INFORMATION TO USERS

This manuscript has been reproduced from the microfilm master. UMI films the text directly from the original or copy submitted. Thus, some thesis and dissertation copies are in typewriter face, while others may be from any type of computer printer.

The quality of this reproduction is dependent upon the quality of the copy submitted. Broken or indistinct print, colored or poor quality illustrations and photographs, print bleedthrough, substandard margins, and improper alignment can adversely affect reproduction.

In the unlikely event that the author did not send UMI a complete manuscript and there are missing pages, these will be noted. Also, if unauthorized copyright material had to be removed, a note will indicate the deletion.

Oversize materials (e.g., maps, drawings, charts) are reproduced by sectioning the original, beginning at the upper left-hand corner and continuing from left to right in equal sections with small overlaps.

Photographs included in the original manuscript have been reproduced xerographically in this copy. Higher quality 6" x 9" black and white photographic prints are available for any photographs or illustrations appearing in this copy for an additional charge. Contact UMI directly to order.

Bell & Howell Information and Learning
300 North Zeeb Road, Ann Arbor, MI 48106-1346 USA
800-521-0600

UMI®

Frictional Convergence and the Madden-Julian Oscillation

Eric Daniel Maloney

A dissertation submitted in partial fulfillment of the
requirements for the degree of

Doctor of Philosophy

University of Washington

2000

Program Authorized to Offer Degree: Atmospheric Sciences

Bell & Howell Information and Learning Company
300 North Zeeb Road
P.O. Box 1346
Ann Arbor, MI 48106-1346

In presenting this dissertation in partial fulfillment of the requirements for the Doctoral degree at the University of Washington, I agree that the Library shall make its copies freely available for inspection. I further agree that extensive copying of the dissertation is allowable only for scholarly purposes, consistent with "fair use" as prescribed in the U. S. Copyright Law. Requests for copying or reproduction of this dissertation may be referred to Bell and Howell Information and Learning, 300 North Zeeb Road, Ann Arbor, MI 48106-1346, to whom the author has granted "the right to reproduce and sell (a) copies of the manuscript in microform and/or (b) printed copies of the manuscript made from microform."

Signature Eric D Maloney

Date 8/16/00

University of Washington
Graduate School

This is to certify that I have examined this copy of a doctoral dissertation by

Eric Daniel Maloney

and have found that it is complete and satisfactory in all respects,
and that any and all revisions required by the final
examining committee have been made.

Chair of Supervisory Committee:

Dennis L. Hartman

Dennis L. Hartmann

Reading Committee:

Dennis L. Hartman

Dennis L. Hartmann

Chris Bretherton

Christopher S. Bretherton

John M. Wallace

John Michael Wallace

Date: 8/16/00

University of Washington

Abstract

Frictional Convergence and the Madden-Julian Oscillation

Eric Daniel Maloney

Chairperson of Supervisory Committee:
Professor Dennis L. Hartmann
Atmospheric Sciences

Frictional surface convergence is shown to be important to the Madden-Julian oscillation (MJO) of the tropical troposphere using both observations and an atmospheric general circulation model (GCM). An observed composite MJO lifecycle is created using the first two empirical orthogonal functions of the NCEP 850 mb equatorial zonal wind as an index. Lower tropospheric water vapor over the Indian and western Pacific Oceans is significantly correlated with 1000 mb convergence during an MJO lifecycle. Frictional convergence may help to precondition the atmosphere for strong MJO convection by moistening the lower troposphere.

Several convection schemes were substituted into the NCAR CCM3 GCM to improve model intraseasonal variability. The McRAS convection scheme, that includes a parameterization of unsaturated convective downdrafts and a relative humidity threshold for convective initiation, produces much improved intraseasonal variability over the default CCM3 convection scheme of Zhang and McFarlane. Intraseasonal variability is decreased for higher relative humidity thresholds with McRAS, contrary to the results of Wang and Schlesinger (1999). Removal of the unsaturated convective downdraft and rain evaporation parameterization greatly diminishes intraseasonal variability in zonal winds and precipitation. An excessively dry tropical troposphere is most likely responsible for the degradation of intraseasonal variability.

Low-level MJO specific humidity anomalies in the model are strongly correlated with surface convergence. This strong coupling with surface convergence causes model MJO convection anomalies to be associated with 850 mb easterly perturbations. Where

the eastward propagating model MJO signal is strong, low-level specific humidity anomalies precede those at middle and upper levels. Surface convergence affects model convection by moistening the lower troposphere, suggesting that surface convergence during an MJO lifecycle may help to precondition the atmosphere for intense MJO convection. Meridional convergence onto the equator contributes most of the anomalous convergence during an MJO lifecycle in both the model and observations. The wind-induced surface heat exchange (WISHE) mechanism of Emanuel (1987) and Neelin and Yu (1994) does not significantly contribute to the MJO-like mode in the CCM3 with McRAS.

TABLE OF CONTENTS

Page

LIST OF FIGURES

LIST OF TABLES

Page

ACKNOWLEDGEMENTS

I would most importantly to thank Dennis Hartmann for his support, guidance, and patience during my 6 years of graduate study. I would further like to thank my committee members Mike Wallace, Jim Holton, David Battisti, Chris Bretherton, and Marcel den Nijs (not necessarily in that order) for providing useful input on my dissertation. My fellow graduate students also provided incredible support, advice, and fun during my six years at UW. None of this work could have been possible without the help of Marc Michelsen, whose computer support saved me months (years?) of frustration. Last, but not least, I would like to thank my wife, Heather, whose patience and support during the past couple of years has made graduate school more enjoyable.

1) Introduction

1.1) Madden-Julian Oscillation Overview

The Madden-Julian Oscillation (MJO) was discovered during the early 1970's in radiosonde and surface data across the tropical oceans (Madden and Julian 1971). Significant spectral peaks on the order of 40-50 days were found in zonal winds and surface pressure for numerous stations near the equator. Since then, an enormous body of work has been published on this phenomenon. The MJO is now understood to be an interaction between tropical convection and the large-scale tropical circulation. It is characterized by an eastward propagating convective envelope over the tropical Indian and Western Pacific Oceans that may contain several convective systems (Chao and Lin 1994). This convective envelope interacts with an eastward-propagating wind pattern dominated by zonal wavenumbers 1 and 2 (Salby and Hendon 1994). The wind response has characteristics of both Kelvin and Rossby waves, often resembling the response to heating described by Gill (1980). Wind anomalies at 850 mb are generally easterly to the east of convection, and westerly to the west of convection. Upper tropospheric winds are 180^{o} out of phase with those at lower levels. Winds at the surface deviate slightly from those at 850 mb due to frictional effects (Hendon and Salby 1994). Rossby wave signatures are present to the northwest and southwest of convection over the Indian and western Pacific Oceans. The speed of propagation of the wave circulation is roughly 5 m s^{-1} in the eastern Hemisphere, where the circulation is strongly coupled to convection, and 12 m s^{-1} in the Western Hemisphere, where equatorial convection is weaker (Salby and Hendon 1994). Figure 1.1 shows a lag regression plot of equatorial (10^{o}N-10^{o}S averaged) 20-80 day filtered 150 mb zonal winds derived from National Centers for Environmental Prediction- National Center for Atmospheric Research (NCEP-NCAR) reanalyses for a reference point at 90^{o}E. The differing phase speeds between the eastern and western Hemispheres are apparent. Slower phase propagation occurs where the intraseasonal convective signal is strong, shown by the lag regression plot of outgoing longwave radiation (OLR) in Figure 1.2.

The collocation of climatological convection and the equator may be important for maintaining the strong equatorial wave signature of the MJO. The MJO signal has a pronounced seasonal cycle. The signal is most prominent in the period December-May when climatological convection is closest to the equator, and is weakest in June-November when convection is to the north of the equator (Salby and Hendon 1994). The location of maximum convection is strongly related to the location of highest SSTs. Although the equatorial signal is weakest in June-September, the MJO does affect the intraseasonal

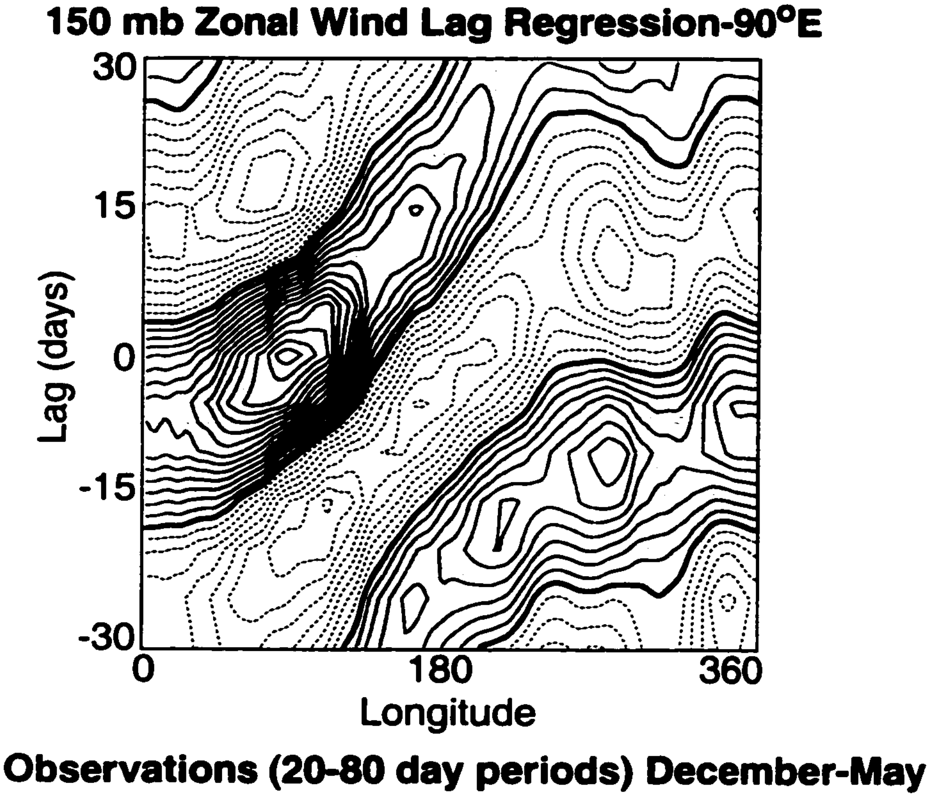

Figure 1.1. Lag regression plot of 20-80 day filtered 150 mb equatorial (10°N-10°S averaged) zonal wind derived from NCEP. Reference time series is located at 90°E and the equator. Contour interval is 0.3 m s^{-1}. Data are available from 1979-1997. Negative contours are dashed.

variability of the Indian summer monsoon (Hartmann and Michelsen 1989, and Chapter 2). The MJO also modulates hurricane activity throughout the Pacific basin, Gulf of Mexico, and western Caribbean Sea during Northern Hemisphere summer (Liebmann et al. 1994, Maloney and Hartmann 2000a,b).

Although many studies have documented the existence and general structure of the MJO, its underlying mechanism is not well understood. Theories abound. One group of theories involves the interaction between equatorial tropospheric Kelvin waves and con-

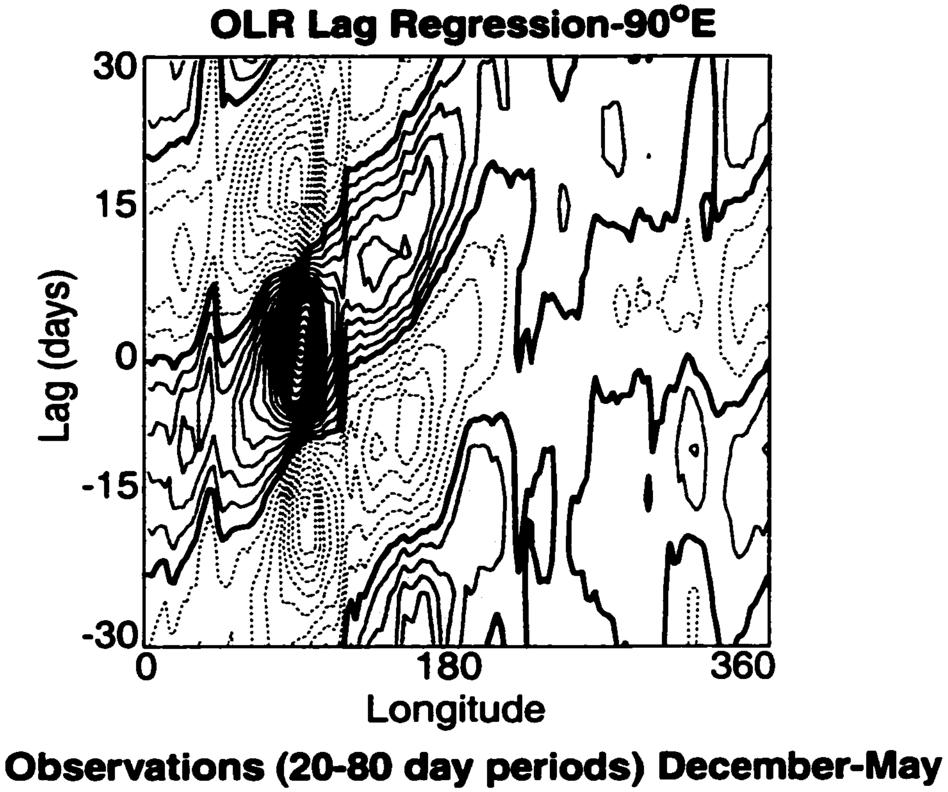

Figure 1.2. Lag regression plot of 20-80 day filtered equatorial (10°N-10°S averaged) outgoing longwave radiation. Reference time series is located at 90°E and the equator. Contour interval is 1.0 W m^{-2}. Data are available from 1979-1997. Negative contours are dashed.

vection. Wave-CISK ideas (Hayashi and Sumi 1986, Lau and Peng 1987, Chang and Lim 1988) are one such manifestation. In wave-CISK theories, the atmosphere is assumed to be conditionally unstable to parcel ascent. The convergent region of an equatorial tropospheric Kelvin wave feeds convection. The strengthening convection forces a stronger wave convergence, which then leads to stronger convection, and so on. This theory has some inherent problems, however. For one, instability seems to occur at the smallest wavelengths, unlike in observations where zonal wavenumbers 1 and 2 are preferred. Wave-CISK theories also have problems explaining the faster propagation speed in the western Hemisphere, and cannot explain the slow 5 m s^{-1} eastward propagation over the Indian and western Pacific Oceans. Others have criticized wave-CISK in that the atmosphere may not be conditionally unstable, but rather convectively neutral to parcel ascent (Emanuel 1987). Any instabilities created in the tropics may be quickly removed by moist convective adjustment.

The introduction of friction into models of Kelvin-wave CISK has led to an improvement in their ability to explain the MJO (Hayashi and Miyahara 1987, Wang and Rui 1990, Salby et al. 1994, Jones and Weare 1996). Boundary layer friction leads to a "coupling" between Kelvin and Rossby wave modes which slows down propagation and causes the largest spatial scales to be preferred. The maximum surface convergence now occurs to the east of inviscid wave convergence due to frictional effects. Meridional convergence contributes a large fraction of this surface convergence to the east of convection. Wave amplification occurs when convective anomalies are supported by surface convergence and convective heating anomalies coincide with positive tropospheric temperature anomalies, leading to the production of eddy available potential energy (EAPE, Hendon and Salby 1994).

Some studies have expanded upon frictional wave-CISK to examine the role that the ocean mixed layer plays in intraseasonal oscillations (Hendon and Glick 1997, Lau and Sui 1997, Flatau et al. 1997, Jones et al 1998, Waliser et al 1998). These studies theorize that SST increases to the east of MJO convection (easterly perturbations) via an increased solar flux into the ocean due to low fractional cloudiness. Light winds in easterly regimes may also increase SST by decreasing the latent heat flux out of the ocean. These effects would presumably enhance the meridional convergence onto the equator to the east of convection by increasing the temperature gradient between equatorial and non-equatorial regions (Lindzen and Nigam 1987). SST is decreased near and to the west of convection due to decreased shortwave radiation reaching the surface, and an increased latent heat flux accompanying westerly wind bursts. Some studies have theorized that the inclusion of realistic ocean mixed layer dynamics into atmospheric general circulation models (GCMs) will improve simulations of the MJO by slowing the speed of propagation in the eastern Hemisphere, and increasing the oscillation amplitude (Flatau et al. 1997, Waliser et al., 1998). Some of the assumptions made in these studies (for example, specifying a relaxation time of 50 days for adjustment of SST back to climatology) may strongly influence the results, however. Reproducibility also needs to be demonstrated more rigorously. For example, Hendon (2000) found that the addition of an interactive upper ocean to an atmospheric GCM influences intraseasonal variability very little. The exact mechanism that slows the eastward propagation speed also needs to be more clearly defined. GCM simulations of the MJO will be discussed in more detail below.

The wind-induced surface heat exchange (WISHE) theory views surface evaporation, rather than moisture convergence, as crucial to the evolution of the MJO (Emanuel 1987, Neelin and Yu 1994, Yu and Neelin 1994). WISHE operates under the premise that the tropical atmosphere is nearly neutral to moist convective ascent. WISHE, in its pure form, assumes a mean easterly state in lower tropospheric equatorial zonal winds. Convection is accompanied by easterly (westerly) wind perturbations to the east (west), as would be expected with an equatorial Kelvin wave. The latent heat flux from the ocean is higher to the east of convection than to the west, increasing the boundary layer equivalent potential temperature there. The high boundary layer equivalent potential temperature air to the east favors convection, which communicates the high moist entropy in the boundary layer to upper levels. One problem with this theory is that lower tropospheric mean winds are not always easterly in the tropical W. Pacific and Indian Oceans, but MJO events still occur in these regions. Some studies have also found that the greatest positive latent heat flux perturbations during an MJO lifecycle occur during westerly wind bursts (Jones and Weare 1996, Lau and Sui 1997). Other work has suggested, however, that mean easterly zonal winds are not necessary for WISHE to produce realistic intraseasonal oscillations (Xie et al., 1993; Crum and Dunkerton, 1994).

Several proposed mechanisms for the MJO do not explicitly require Kelvin wave dynamics. The idea of radiative-convective relaxation is one such theory (Hendon and Liebmann 1990, Blade and Hartmann 1993, Hu and Randall 1994). After the passage of an MJO convective event, low level drying and cooling, and upper level heating cause stabilization of the atmosphere. Preconditioning must take place before convection can again occur. Lower levels must be sufficiently moistened, and upper levels must be cooled radiatively before the atmosphere is ripe for convection. This period of preconditioning sets the timescale for the next convective event. This relaxation theory cannot explain the eastward propagation and organization of convective anomalies without some dynamical considerations. Frictional moisture convergence may assist the preconditioning process and can favor the eastward propagation of convective anomalies. This issue will be examined in Chapters 2 and 4. Surface fluxes and convection of low-precipitation efficiency have also been proposed as a means to precondition the lower atmosphere (Raymond and Torres 1998). Wang and Schlesinger (1999) instituted a relative humidity threshold for initiation of convection in an atmospheric GCM to simulate the requirement of boundary layer preconditioning. They concluded that intraseasonal variability increases as the relative humidity threshold is increased. The use of a relative humidity threshold, and how it influences intraseasonal variability in the National Center for Atmospheric Research Community Climate Model 3 (NCAR CCM3) GCM, will be analyzed in Chapter 3 of this dissertation.

Another non-Kelvin wave theory for the MJO is the theory of teleinduction (Chao and Lin 1994, Chao and Deng 1997, Chao and Deng 1998). Mean flow at lower levels is assumed to be from the east, as with the WISHE mechanism. Equatorial mesoscale convective systems teleinduce new convection to the east via gravity waves. The Kelvin and Rossby wave structure that is observed with the MJO is simply a response to convective heating, as in Gill (1980). No new convection is generated to the west because moisture is consumed by the original cluster in the mean easterly flow. Individual cloud complexes move westward, but the convective envelope moves eastward. Convective gust fronts induced by downdraft evaporation and precipitation drag can also induce teleinduction. Surface convergence caused by gust fronts can spawn additional convection at a distance, with regions to the east being favored in mean easterly flow. These teleinduction theories are in their infancy relative to the other theories, and much more study is needed to determine if they are viable mechanisms.

Other work suggests that the extratropics can play an important role in the intraseasonal variability of the tropics (Lau and Phillips 1986, Hsu et al. 1990, Dickey et al. 1991, Bladé and Hartmann 1993, Meehl et al. 1996). These studies hypothesize that the extratropics can influence the triggering and/or propagation characteristics and timescale of MJO convective events. Such ideas are outside the realm of this dissertation and will not be explored here.

GCMs have had a notoriously difficult time in reproducing the MJO (Slingo et al. 1996). Some deficiencies in the simulations as compared to observations include:

- Too fast a speed of propagation in the eastern Hemisphere
- Amplitudes that are too weak
- Less coherent zonal wind structures, particularly over Indonesia and the W. Pacific
- Too weak a seasonal dependence in the signal
- Lower than observed 200 mb zonal wind variance at periods of 50-60 days

The performance of GCMs in simulating the MJO is very dependent on the convective parameterization. Slingo et al. (1996) has found that convective schemes closed on buoyancy generally perform better than those closed on moisture convergence. Similarly, GCMs that have convection well correlated with SST perform better than those with smaller correlations. Models with the most realistic mean states produce the best oscillations.

1.2) Goals of this Dissertation

The goal of this research is to better understand the mechanisms responsible for tropical intraseasonal variability. In particular, I will analyze the hypothesis that lower tropospheric water vapor and frictional moisture convergence play critical roles in the evolution of the MJO. Observations and the NCAR CCM3 GCM (Kiehl et al. 1998) will be used in this analysis. I will also use the CCM3 to determine the importance of the WISHE mechanism for MJO variability.

The flow of this dissertation is explained in the next few paragraphs. Chapter 2 examines frictional moisture convergence in an observed MJO lifecycle. An MJO index derived from the first two empirical orthogonal functions (EOFs) of the equatorial intraseasonal 850 mb zonal wind is used as a basis for compositing the MJO. Lower tropospheric water vapor is found to be significantly correlated with surface convergence during an MJO lifecycle. The growth of positive water vapor anomalies precedes that of MJO convection. The modulation of break periods in the Indian summer monsoon by the MJO is also briefly examined using the equatorial wind index.

Chapter 3 attempts to find a convective parameterization suitable for studying tropical intraseasonal variability when implemented in the NCAR CCM3. The goal is to produce a GCM simulation with which to study the effects of frictional convergence on the MJO. An intercomparison of intraseasonal variability in the CCM3 is conducted using four different deep convection parameterizations. The MJO is most realistically simulated by the microphysics of cloud with relaxed Arakawa-Schubert (McRAS) convection scheme of Sud and Walker (1999a). Convective rain evaporation with unsaturated downdrafts are found to be crucial to realistically simulating the MJO in McRAS. Convective rain evaporation with unsaturated downdrafts act to moisten the lower troposphere in the mean. The simulation of intraseasonal variability with McRAS is not sensitive to a boundary layer relative humidity threshold.

Chapter 4 examines the role of frictional convergence in an MJO lifecycle, as simulated by the CCM3 with McRAS convection. Frictional convergence is found to be strongly correlated with composite water vapor anomalies and intraseasonal convective anomalies. Lower tropospheric vertical advection associated with surface convergence controls lower tropospheric water vapor during a composite lifecycle. WISHE is shown not to be important for maintaining the model MJO. Conclusions and suggestions for future work follow in Chapter 5.

2) Frictional Moisture Convergence in a Composite MJO Lifecycle

This chapter describes work published in the *Journal of Climate* (Maloney and Hartmann 1998).

2.1) Introduction

Much has been published concerning the Madden-Julian Oscillation (MJO) since it was first discovered by Madden and Julian (1971,72) in rawinsonde and sea level pressure data from the tropical oceans. The MJO is now understood to be a dominant mode of variability in the tropical circulation that has characteristic periods of 30-60 days (Madden and Julian 1994). Ultimately, a complete understanding will probably involve the interaction among convection, wave dynamics, boundary later circulations, and moisture. This paper seeks to further that understanding by constructing a composite lifecycle of the MJO using wind, convergence, water vapor, and precipitation fields.

Recent work suggests the importance of interactions among the large-scale wave, the boundary layer, and convection in determining the mechanisms that give rise to the MJO. Frictional convergence in the boundary layer east of the main convective area has been shown to be important in the evolution and eastward propagation of the MJO in several recent modeling studies (Wang and Rui 1990, Salby, Garcia, and Hendon 1994, Seager and Zebiak 1994, Wang and Li 1994). Observational evidence has also shown that the convective anomaly associated with the MJO is tied to convergence in the boundary layer. Hendon and Salby (1994) showed this by compositing the 1000 mb divergence field in relation to outgoing longwave radiation (OLR). Convection is fostered in areas of boundary layer convergence, while boundary layer divergence suppresses convection. A recent study by Jones and Weare (1996) using ISSCP (International Satellite Cloud Climatology Project) and ECMWF (European Centre for Medium-Range Weather Forecasts) analyses has also shown that the maximum low level moisture convergence occurs to the east of the main convective area. Surface convergence provides an upward flux of moisture in the boundary layer by increasing the low level equivalent potential temperature, through moistening (e.g. Seager and Zebiak, 1994).

Geostrophic zonal wind dynamics, as in classical equatorial Kelvin wave theory, requires that inviscid lower tropospheric easterly wind perturbations be accompanied by a surface pressure trough at the equator, whereas inviscid lower tropospheric westerlies should be accompanied by a pressure maximum (Matsuno 1966). Therefore, friction will foster convergence into the equatorial pressure trough below 850 mb easterlies. Since the growing convective area associated with the MJO over the Indian Ocean is accompanied by 850 mb easterlies to the east over the W. Pacific (Knutson and Weickmann 1987, Hendon and Salby 1994), convection will be supported by boundary layer convergence to the east and suppressed to the west, where 850 mb westerly perturbations and surface divergence are found. Rossby wave generation in the Indian Ocean in the presence of convective heating may also dry the atmosphere to the west of convection through subsidence or horizontal advection from the west or extratropics (Gill 1980). Some previous studies have suggested that the atmosphere goes through a period of preconditioning before being able to sustain convection associated with the MJO (Hendon and Liebmann 1990, Bladé and Hartmann 1993, Hu and Randall 1994). The humidity profile at a fixed point in the lower troposphere moistens slowly and then dries quickly as the convection passes and westerly winds ensue (Bladé and Hartmann 1993). These studies reason that a period of buildup of moist static energy is required for the atmosphere to recover from the previous cycle of convection, which had the effect of stabilizing and drying the atmosphere. In the present study we speculate that a period of buildup of moisture is required over the Indian and W. Pacific Oceans before significant convection can occur, and that this may in fact set the time scale for the jump in convection from the Indian Ocean to the W. Pacific Ocean. Frictional surface convergence may be a key player in this preconditioning of the atmosphere.

Hendon and Salby (1994) (Hereafter referred to as HS) composited 200 mb wind, 850 mb wind, MSU (Microwave Sounding Unit) temperature, OLR, 1000 mb wind, 850 mb divergence, and 1000 mb divergence anomalies. The observed composites are similar to the typical picture derived from modeling studies of a coupled equatorial Rossby-Kelvin wave (e.g. Wang and Li 1994). The HS composites show that maximum convergence at 1000 mb precedes inviscid convergence at 850 mb, which is consistent with the ideas examined in modeling studies. Divergence at 1000 mb lags to the west of convection, and may contribute to its demise when the convective area is engulfed by 850 mb westerly perturbations.

The present study takes a similar strategy as HS in creating a composite MJO lifecycle as a function of 9 phases. In this study, however, the compositing technique, the choice of fields composited, and the method of filtering are significantly different from HS. First, we use 850 mb zonal wind as a compositing basis instead of OLR. Whereas in HS a regression analysis on OLR is used, this paper creates an index for compositing based on the first two EOFs (empirical orthogonal functions) of the 850 mb equatorial zonal wind and then selects events based on this index. Details of the technique will be described in subsequent sections. Second, like HS, this paper composites the fields of 200 mb wind and 850 mb wind, along with 1000 mb convergence. In addition to the fields considered by HS, precipitable water anomalies are composited, along with MSU precipitation in place of OLR. Composites of precipitable water give supporting evidence that regions of boundary layer convergence actually lead to increased column water vapor in areas undergoing surface convergence. The MSU precipitation data give a better indication of the location of heating than OLR, at least over the oceans. Thus, the MSU precipitation field is able to give a more detailed picture of fine structure associated with convective areas. A third significant departure is that HS zonally filtered all fields to zonal wavenumbers 1-3, whereas this study uses no zonal filtering. The composites in HS consequently cannot resolve the separate amplification of convection over the Indian and W. Pacific Oceans (Weickmann and Khalsa 1990, Salby and Hendon 1994), a fact that is duly noted in HS. As will be seen later, the composites created here are able to resolve the Indian Ocean convective center and the W. Pacific convective center and detail the transition between the two regions.

The seasonal dependence of the MJO has been examined in some detail in previous studies (a good review can be found in Madden and Julian 1994), and an examination of the Northern Hemisphere summer composites in the present study (Chapter 2.5) proves to be somewhat enlightening. Particularly interesting is the role of the MJO in the regulation of the Indian summer monsoon. Previous studies have examined this aspect of the MJO and have shown that "break" periods of the Indian monsoon seem to occur on intraseasonal time scales, with strong indications of being phase-locked to MJO events (e.g. Hartmann and Michelsen 1989, Madden and Julian 1994). Creating a composite view of the NH summer case proves to be very interesting in this respect in that "break" and "active" periods of the monsoon can be directly traced to the phase of the MJO being examined in the composites. High spatial resolution shows that Rossby-wave structure is responsible for northward propagating precipitation areas.

Section 2 describes the data products used and section 3 describes the compositing technique. Section 4 will present the composites created for all seasons of the year, while section 5 will look at the Northern Hemisphere summer. Conclusions will be presented in section 6.

2.2) Data

NCEP/NMC reanalysis data (Kalnay et al. 1996) were used for the 200 mb, 850 mb, and 1000 mb wind fields. Convergences were derived using these wind fields. Pentad (5-day mean) averages were used from 1979-1995 in a gridded 2.5° x 2.5° format. Operational ECMWF analyses were originally used in the study, but then replaced by the NCEP reanalysis product when it became available. The NCEP data for the entire 1979-1995 period were derived from the same model and data assimilation scheme. Our results do not significantly differ for the two datasets. In this study the wind convergence at 1000 mb plays an important role. Over the oceans the surface winds are largely generated by the model dynamics and boundary layer scheme, and not by direct observations, so our conclusions are subject to the assumption that the model produces realistic surface wind convergence. Surface meridional convergence anomalies at 165°E and the equator from NCEP and the TAO (Tropical Atmosphere Ocean) buoy array were compared for the years 1988-1995 using the compositing technique described in Section 3. Similar anomalies were seen in both datasets (see Appendix A), although the sample size was too small to produce statistically significant results.

MSU precipitation data were used in pentad form for the years 1979-1995. The precipitation dataset is derived by using Channel-1 of the Microwave Sounding Unit which is sensitive to emission by cloud water and rain water in the lowest few kilometers of the atmosphere (Spencer 1993). The MSU precipitation product is only able to detect precipitation over the ocean, which is adequate for this study, since ocean surface dominates the region of interest. The reliability of MSU precipitation over the Maritime continent is a question, but the OLR signal does not indicate any strong convective signals over island areas that do not exist in the MSU precipitation data. The AVHRR (Advanced Very High Resolution Radiometer) NOAA OLR product (Gruber and Krueger 1984) was used to corroborate signals in MSU precipitation in certain key regions, and proved useful in examining signals around the Indian subcontinent.

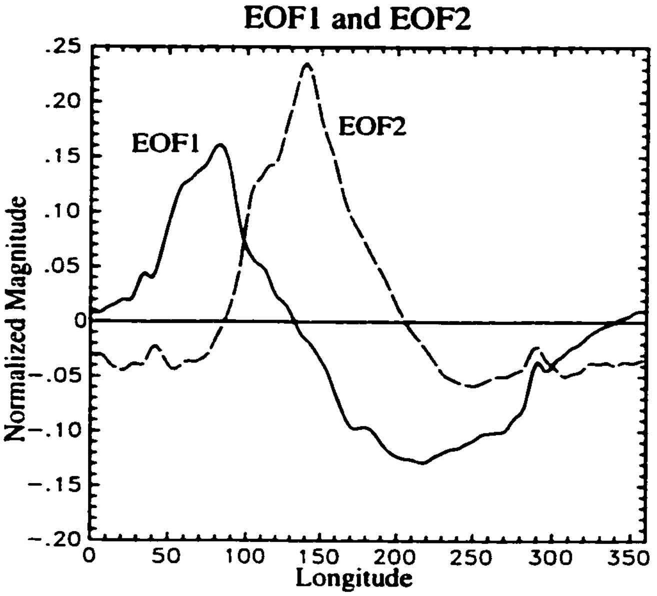

Figure 2.1. EOF1 (solid) and EOF2 (dashed) of 850 mb zonal wind as a function of longitude. Magnitudes were normalized in the computation of the EOFs.

NVAP (NASA Water Vapor Project) precipitable water data (Randel et al. 1996) were available from 1988-1992 in pentad form. The NVAP product is a merged product of three different datasets: Radiosonde, SSM/I (Special Sensor Microwave/Imager), and TOVS (TIROS Operational Vertical Sounder). The merged product gives water vapor values for three different levels: surface to 700 mb, 700 mb to 500 mb, and 500 mb to 300 mb.

2.3) Compositing Technique

The index used for compositing was constructed using the 20-80 day bandpass filtered 850 mb zonal wind field. The filter was designed to have a frequency response with half-power points at 20 and 80 days, effectively retaining near full amplitude frequencies in the 30-60 day range. The 850 mb zonal wind was averaged from 5°N to 5°S every 2.5° around the equator. EOF analysis was then done on the resulting equatorially averaged zonal wind field for the entire 1241 pentad record (1979-1995). EOF 1 and EOF 2 are displayed in Figure 2.1. EOF1 explains 32% of the total bandpass filtered variance, while EOF 2 explains 22%. EOFs 3 and 4 explained 10% and 7%. Using the criterion developed by North et al (1982), the first two EOFs are significantly different from the rest. Principal component analysis by projection of the first two EOFs onto the filtered 850 mb zonal wind field shows that the principal component for EOF 1 peaks in magnitude an average of 2-3 pentads before the principal component for EOF 2.

EOF 1 and EOF 2 appear to form a propagating signal in the zonal wind. EOF 1 in its positive polarity appears to show westerlies at lower levels over the Indian Ocean changing over to easterlies over the Pacific Ocean at roughly 130°E. Peaking 2-3 pentads later, EOF 2 corresponds to the strong low-level westerly winds that accompany many MJO events over the western and central Pacific Oceans. (e.g. Lau et al. 1989) Further progression with time reveals that the EOFs nicely depict the cycle of 850 mb wind perturbations which accompany MJO events that have been detailed in prior observational work. (e.g. Madden and Julian 1972, Knutson and Weickman 1987, Hendon and Salby 1994)

An index was constructed in the following manner, where t is the time in pentads:

$$Index(t) = PC1(t) + (PC2(t+2) + PC2(t+3))/2 \qquad (2.1)$$

The index is a linear combination of the principal components (PCs) of EOF 1 and EOF 2. Since the principal component of EOF 2 peaks an average of 2-3 pentads after the principal component of EOF 1, contributions from the principal component of EOF 2 both 2 and 3 pentads later are added to the principal component of EOF 1 in order to form the index. The results are insensitive to reasonable variations in the time at which PC 2 is taken into account. Since the PCs are proportional to the amplitude explained, no weighting between PC 1 and PC 2 other than this is required. The selection of events is not sensitive to this weighting. The time at which the index is at a maximum is when a region of maximum convergence of the 850 mb zonal wind anomalies is centered at about 130°E.

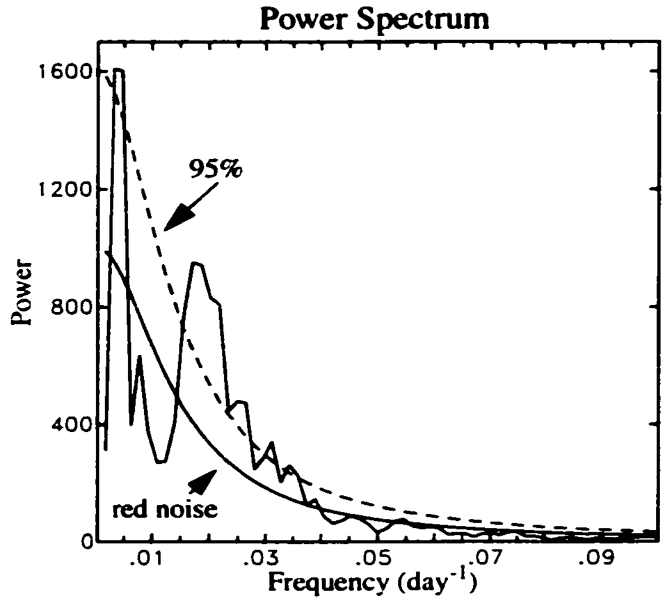

Figure 2.2. Power spectrum of the MJO index obtained by projecting the first two EOFs onto the unfiltered equatorial time series of 850 mb zonal wind for 1979-1995. The red noise spectrum is displayed along with the *a priori* 95% confidence limit.

To test whether the index indeed captures the essence of the zonal wind signal associated with the MJO, the first two EOFs were projected onto the *unfiltered* 850 mb zonal wind time series averaged over 5°S to 5°N. The index above was then reconstructed using these unfiltered principal components and the power spectrum was computed. The results of the spectral analysis are shown in Figure 2.2. Two features are readily apparent. A large peak is associated with the annual cycle and, most importantly, a second peak prominently stands above the background spectrum at intraseasonal periods of roughly 30-80 days. The intraseasonal peak is significantly different from the red noise spectrum at the 95% level. This zonal wind index thus captures the nature of the MJO, even when projected onto unfiltered data.

Once the index was constructed, phases were assigned. The time variation of the index is that of an oscillating pattern much like a sinusoidally varying function. Key events were determined by choosing events that had peak amplitudes greater than one standard deviation away from zero. Periods in which the index did not have succeeding positive and negative anomalies were ignored, but as it turns out, these periods would have been filtered out by the selection process regardless, because the magnitudes were small during these times. Criteria such as choosing events with maximum peak to trough amplitude and maximum trough amplitude were also tried, and the results were found to be insensitive to the exact criterion used. As a result of this selection criterion, 81 events were isolated during the period 1979-1995 for all seasons. Once the events were isolated, each event was broken into 9 different phases for compositing. Phase 5 was designated the time in each event at which the index had maximum peak amplitude. Phase 1 and Phase 9 were given to the times in each event with largest trough amplitude before and after Phase 5 respectively. Phases 3 and 7 were given to the zero increasing and zero decreasing points in each event, and the other phases were placed equidistant in time between Phases 1,3,5,7, and 9. The 81 events were then averaged together to produce a composite event.

Water vapor values were available for only the years 1988-1992, so the number of events included in the water vapor composites is only 28. Compositing the fields other than water vapor for the years 1988-1992 showed the same features as for the longer period of 1979-1995, so we feel it is justified to display the water vapor composites alongside the composites for the other variables that were determined from the entire 1979-95 record.

2.4) Composites

Figures 2.3-2.14 detail the evolution of a composite cycle of the MJO. All seasons are included. Wind fields were bandpass filtered to 20-80 days and convergences were derived from these filtered wind fields. The annual cycle was removed from the precipitation and water vapor fields. Winds at 200 mb are displayed along with MSU precipitation for all nine phases. Vectors that are significantly greater than zero at the 90% level are plotted in black. The significance of wind vectors was determined by comparing the magnitude of the vector wind anomalies to a null hypothesis of zero. Winds at 850 mb are displayed along with the 1000 mb convergence field. Water vapor anomalies are displayed with the 90% significance levels shaded. Since the patterns in the water vapor field show no significant dependence on the particular level examined, we show the anomalies of column integrals from the surface to 300 mb. In the Indian and W. Pacific Oceans at the lowest levels, the moisture anomalies in our composites correspond to equivalent potential temperature variations of 2-3°C.

2.4.1) Phase 1

Figure 2.3 shows the situation at Phase 1 of the composite cycle. At this time the precipitation anomaly over the Indian Ocean is weakly negative. Westerly 200 mb wind anomalies extend across this region with easterlies at 850 mb. Patches of surface convergence can be seen near the equator over the Indian Ocean in association with the 850 mb easterly winds, a theme which will be repeated in the composite pictures for other phases. A positive water vapor anomaly appears over the western Indian Ocean at about 50°E near the westernmost convergence center at 1000 mb. A small anomaly appears in the precipitation record coincident with the water vapor record from 1988-1992 (not shown). The precipitation anomaly is not significant, whereas the water vapor anomaly is. The devel-

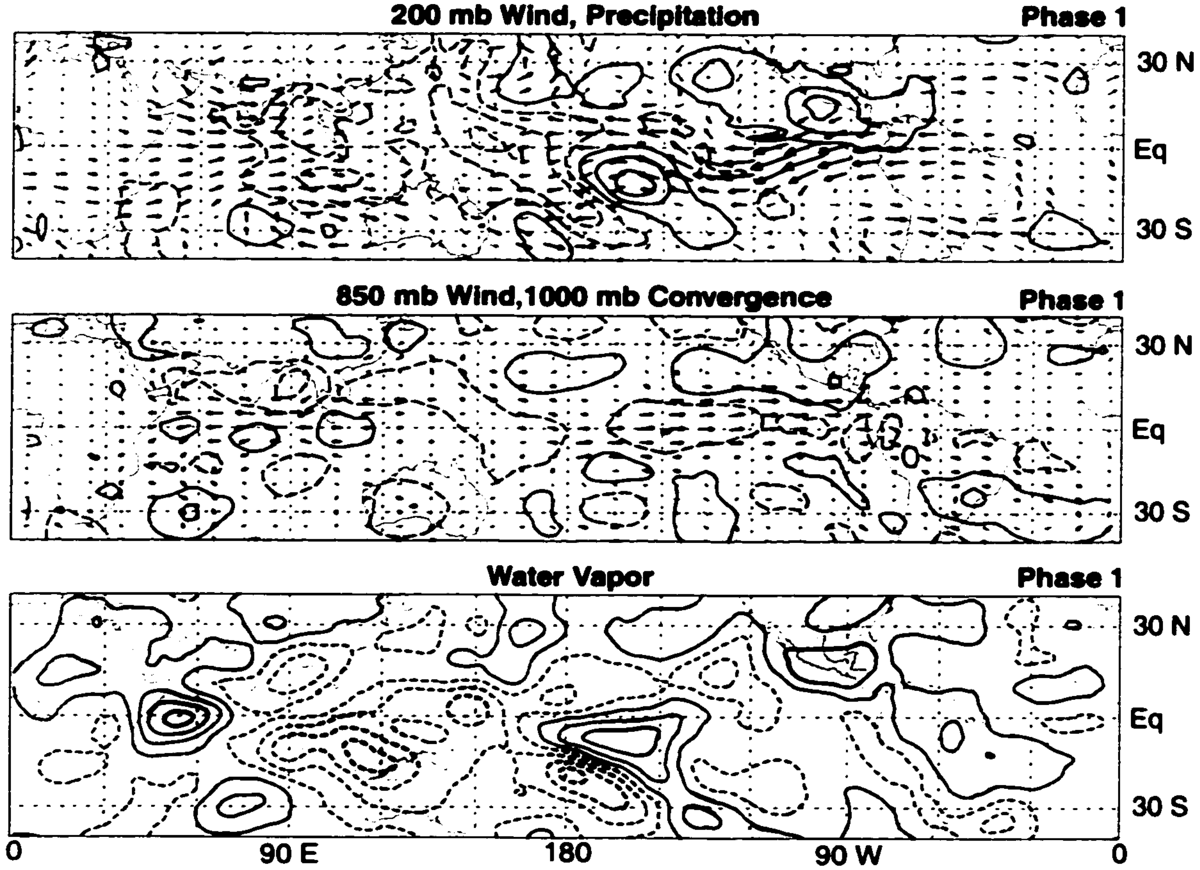

Figure 2.3. The top two panels are Phase 1 composites of bandpassed 200 mb and 850 mb wind anomalies, MSU precipitation anomalies (without annual cycle), and the bandpassed 1000 mb convergence anomaly field for the period 1979-1995 (all seasons). Significant vectors are shown in black while others are shown in gray. The third panel is a composite of NVAP water vapor anomalies (without annual cycle) integrated to 300 mb, displayed for the years 1988-1992. Maximum wind vectors are 6.1 m s^{-1} and 2.8 m s^{-1} for 200 mb and 850 mb respectively. Precipitation contours are at intervals of 0.6 mm day^{-1} starting at 0.3 mm day^{-1}. Convergences are at intervals of $2x10^{-7}$ s^{-1} starting at $1x10^{-7}$ s^{-1}. Water vapor anomalies are at intervals of 0.8 mm starting at 0.4 mm. Regions significant at the 90% level are shaded. Convergence contours are solid and divergences are dashed. Negative contours are dashed for precipitation and water vapor.

opment of a strong positive water vapor anomaly without a strong signal in precipitation over the W. Indian Ocean is intriguing. It is notable that this same feature will appear in

Phase 9. The timing of this feature in Phases 8 and 9 seems to correspond to the onset of easterly 850 mb wind anomalies in this region.

Farther to the east, negative precipitation anomalies and negative water vapor anomalies are occurring from the Central Indian Ocean near 70°E eastward to the dateline. The remnants of the previous cycle of convection can be seen just to the east of the dateline at about 10°S. Significant water vapor anomalies match up nicely with this feature. Westerly anomalies at 850 mb and strong 200 mb easterly wind anomalies occur from the dateline eastward to past 60°W. Another intriguing feature that is also seen in Phase 9 is the positive precipitation and water vapor anomaly to the south of Mexico and Central America extending northwestward from 90°W. This feature is most prominent in the Northern Hemisphere summer (not shown). This precipitation is coincident with cyclonic shear of the zonal wind associated with the westerly wind anomaly near the equator at 850 mb. The MJO strongly modulates tropical cyclone activity in this region of the Eastern Pacific Ocean during northern Hemisphere summer. Maloney and Hartmann (2000a) found that eastern Pacific hurricanes are four times more likely during MJO westerly anomalies than easterly anomalies.

2.4.2) Phase 2

In Phase 2, weak positive anomalies in precipitation are present over the equatorial Indian Ocean at the African coast and at about 80°E (Fig. 2.4). The eastern edge of this developing precipitation area is where the main convective area for the Indian Ocean will develop during subsequent phases. The water vapor anomaly has expanded slightly toward the east. Both the precipitation and water vapor anomalies are growing in a region of increasing 1000 mb convergence which is expanding eastward with the 850 mb easterly wind perturbations. Negative water vapor anomalies over the western Pacific and the Maritime Continent (90°E- 150°E) have begun to weaken along the equator in the area coincident with the surface convergence. We hypothesize that surface convergence plays the necessary role of eroding negative water vapor anomalies over the W. Pacific thereby cre-

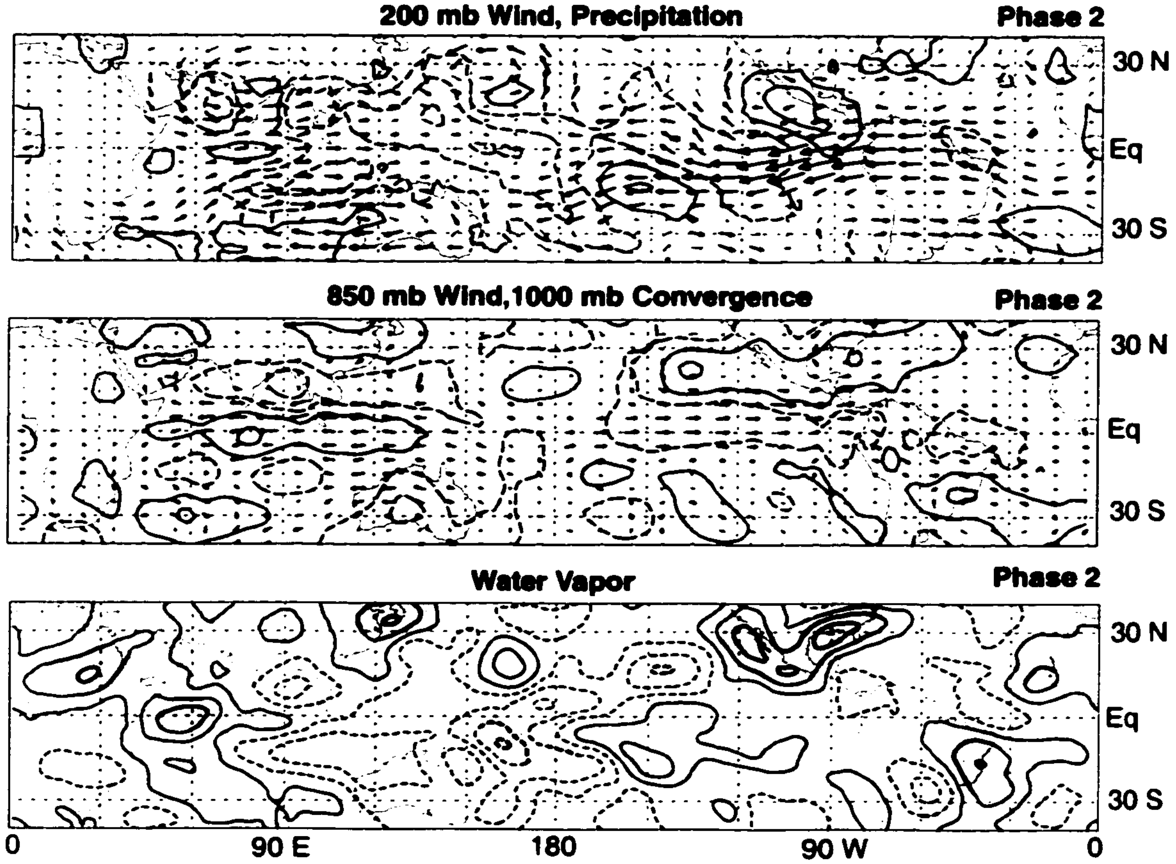

Figure 2.4. Phase 2 composites. Otherwise, same as Figure 2.3.

ating an environment favorable for convection. Upper tropospheric wind perturbations are westerly over the equator from 60°E to 150°E and are associated with cyclones in the 200 mb wind field at about 25°N and 25°S, a picture consistent with HS.

To the east, a weak area of convection can still be found near 150°W and 15°S. Precipitation and water vapor anomalies are still enhanced along the Mexican and Central American coasts associated with summertime convection. The 1000 mb convergence field continues to show positive anomalies over this area also. Rather strong easterly 200 mb wind anomalies are occurring along and just to the south of the equator from 150°W to 30°W.

2.4.3) Phase 3

In Phase 3 rainfall begins to blossom in the E. Indian Ocean at about 80°E (Fig. 2.5). This convection is accompanied by a strong water vapor anomaly. The convection is accompanied by surface convergence, which extends eastward of the convection with the 850 mb easterlies that extend to about 160°E. The water vapor field shows that the negative anomalies over the equatorial W. Pacific have been eliminated and some positive anomalies are developing near 150°E, which is consistent with persistent surface convergence in these areas. Positive anomalies in the water vapor field generally precede positive anomalies in the precipitation field in the western and central Pacific Oceans. This sug-

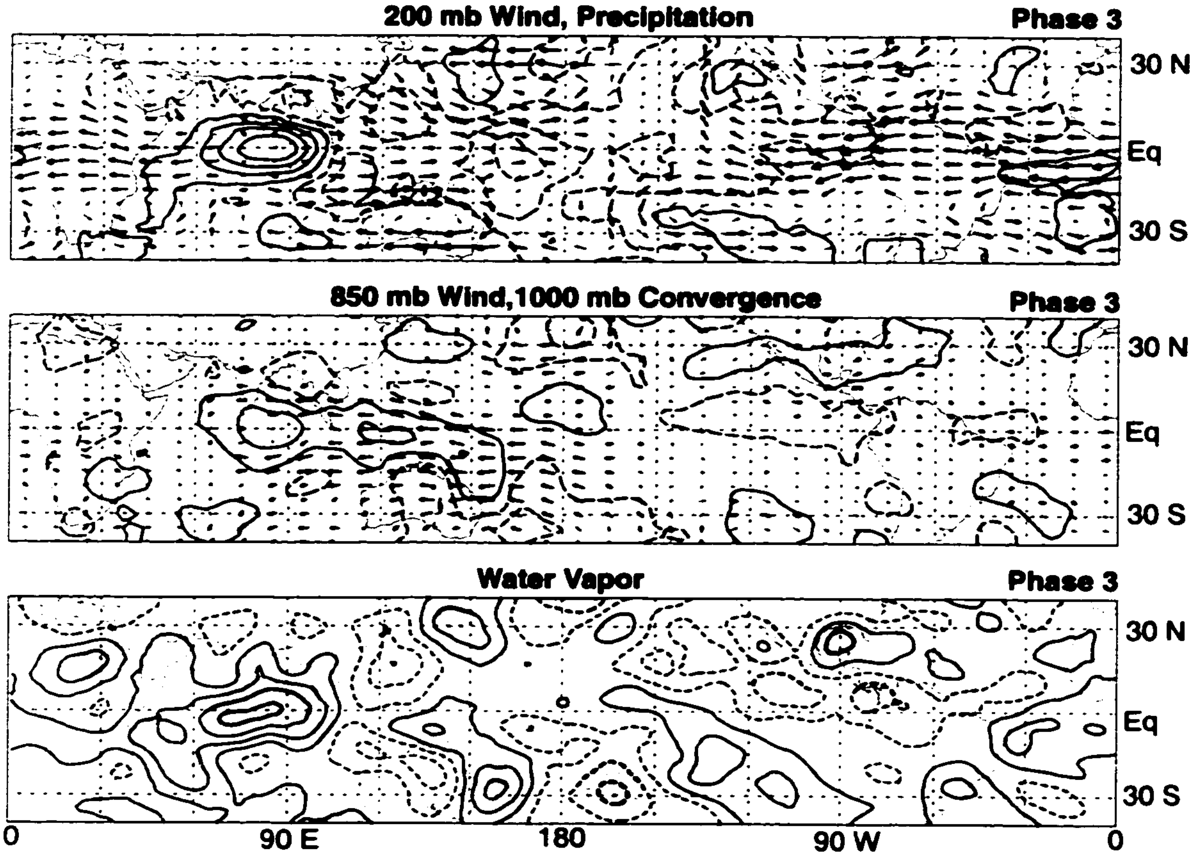

Figure 2.5. Phase 3 composites. Otherwise, same as Figure 2.3.

gests that the atmosphere in this region needs to be preconditioned before convection is able to occur there. This idea is similar to the idea proposed by Hendon and Liebmann (1990), Bladé and Hartmann (1993), and Hu and Randall (1994) that the atmosphere requires a period of buildup of moist static energy before convective events can be maintained. In the present paper, we see that surface convergence acts to increase the precipitable water in the W. Pacific and thus increase the moist static energy of that region. The drying of the atmosphere after passage of the previous convective event is counteracted in part by the moistening of the atmosphere by surface convergence below the 850 mb easterly wind perturbations. In the Indian Ocean also, a buildup of moisture anomalies serves as a precursor to the actual convective event. As was seen in Phase 1, a strong buildup of anomalies in the water vapor field occurs before the strong onset of convection in the Indian Ocean near 80°E, although the precursor event in the Indian Ocean is not collocated with the main convective development.

Figure 2.6 shows lag correlations between convergence at 1000 mb and 850 mb and column integrated water vapor anomalies for the Indian and W. Pacific Oceans. Convergence at 1000 mb leads positive vapor anomalies by 0-1 phases over the Indian Ocean and 1-2 phases over the W. Pacific Ocean. Positive correlations on the order of 0.4-0.45 that are significantly different from zero at the 95% level are found in both regions. Convergence at 850 mb lags positive vapor anomalies by one phase over the W. Pacific Ocean with no phase lag over the Indian Ocean. Correlations between 850 mb convergence and vapor anomalies are lower (0.3-0.35) than for 1000 mb convergence. These correlations provide evidence that surface convergence and water vapor anomalies are indeed linked and that convergence at 850 mb is not crucial for the development of water vapor anomalies. Convergence anomalies at 850 mb are generally about 50% weaker than those at the surface (not shown).

2.4.4) Phase 4

Phase 4 shows the convection over the Indian Ocean at its peak (Fig. 2.7). The center of convection has moved very little since Phase 3, indicating that this convective center is

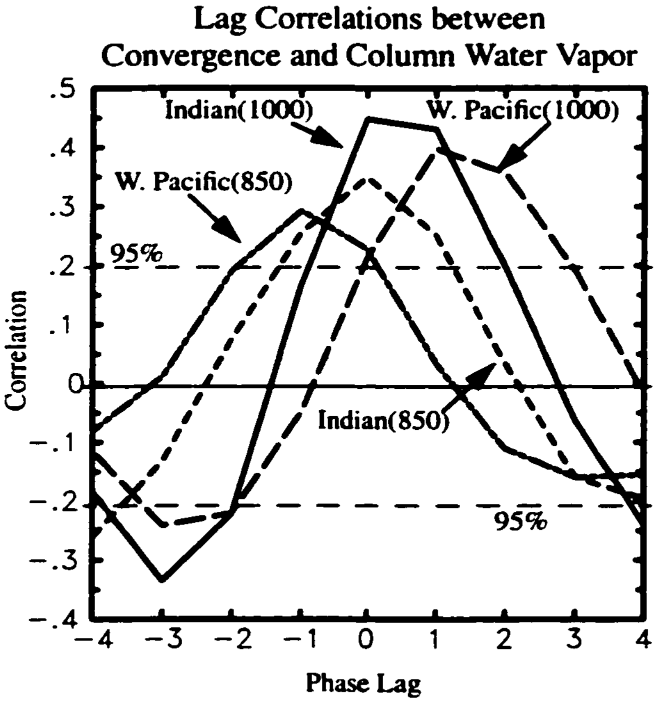

Figure 2.6. Plot of lag correlations between 850 mb and 1000 mb convergence and column water vapor anomalies in the Indian and W. Pacific Oceans as a function of the lag in phases for 1979-1995 (all seasons). A positive phase lag means convergence leads water vapor. Indian Ocean correlations are averaged over an area from 5°N to 5°S and 65°E to 85°E. (solid-1000 mb, short dash-850 mb) W. Pacific correlations are averaged over an area from 5°N to 5°S and 130°E to 150°E. (long dash-1000 mb, dot-dash-850 mb) The dashed horizontal lines represents the limits at which correlations are significantly different from zero at the 95% level at 1000 mb for the W. Pacific Ocean.

virtually growing in place over the eastern Indian Ocean between 80-85°E along the equator. HS note that the same stationary feature in convection would have been obtained in their composites had they not filtered all fields to zonal wavenumbers 1-3. Positive water vapor anomalies have now taken hold eastward from this area to about 150°E along the equator, and a tongue of surface convergence now extends to about 135°W in the company of 850 mb easterly perturbations. These easterlies are flanked to the north and south by anticyclones evident in the 850 mb wind field and cyclones at 200 mb. The precipitation anomaly to the south of Central America has reversed. Negative precipitation anoma-

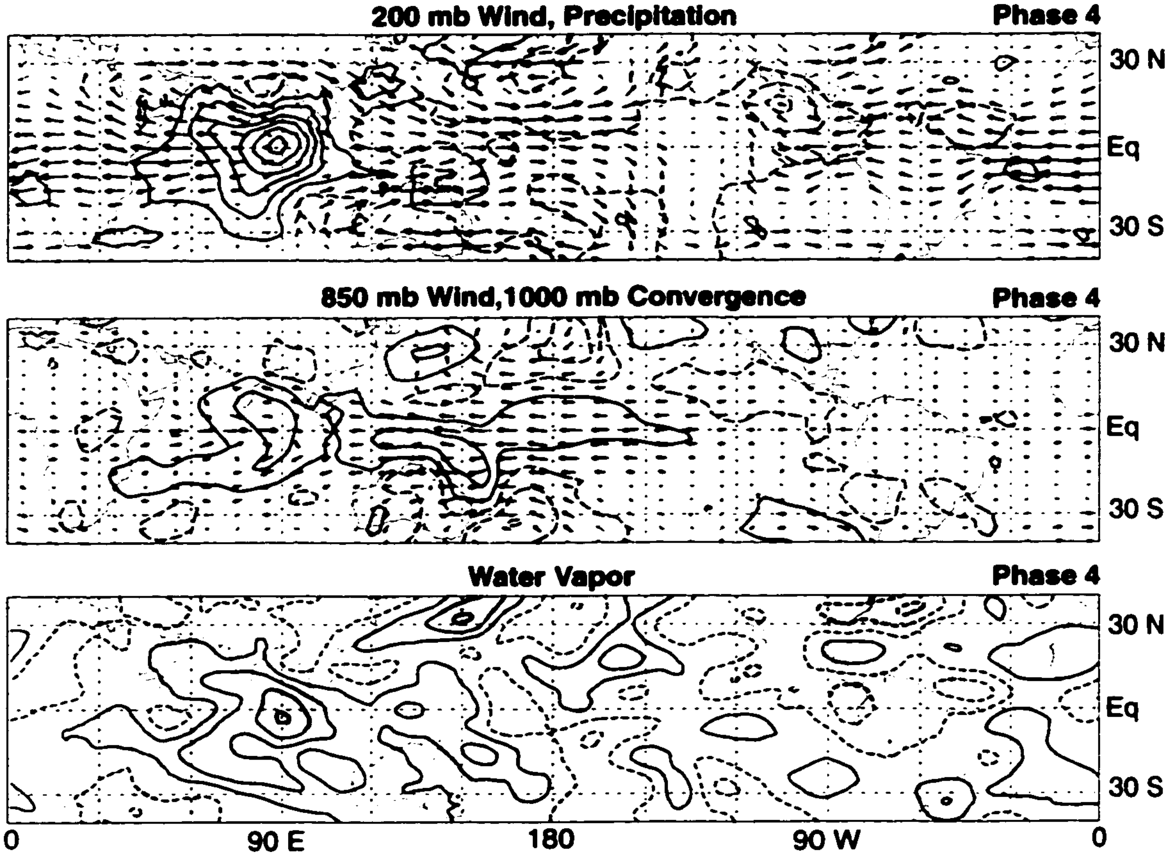

Figure 2.7. Phase 4 composites. Otherwise, same as Figure 2.3.

lies and anticyclonic shear of the 850 mb zonal wind will continue to develop in this area during subsequent phases. The beginning of cyclones in the 850 mb wind field can be seen to the immediate northwest and southwest of the main convective region, along with a broader anticyclone pair in the 200 mb wind field. These features are consistent with Rossby wave propagation away from the main convective area. Circulation patterns in the Indian Ocean appear to be most interesting during Northern Hemisphere summer, particularly north of the equator. These will be examined in more detail in section 5.

Westerly perturbations at 850 mb are apparent from the Indian Ocean convection westward. A dry water vapor anomaly is beginning to grow near 50°E. A couple of mechanisms may explain the appearance of this anomaly. One possibility is that surface divergence (barely detectable by the first contour level over the W. Indian Ocean) due to an equatorial pressure maximum dries the lower atmosphere. Second, subsidence or horizontal advection from the west or extratropics associated with Rossby wave circulations may dry the air (Gill 1980). Subsequent composites will show that these westerlies will form a wedge of dry anomalies along the equator that will act to suppress convection in areas affected by it. Winds at 200 mb are out of phase with those at 850 mb and display easterly anomalies.

Returning to the idea of surface convergence, the 850 mb convergence and wind fields are plotted for Phase 4 in Figure 2.8. Although at 1000 mb a tongue of convergence extends across the equatorial Pacific to about 130°W, no such tongue is found at 850 mb. This implies that it is the surface convergence which must be causing the moisture increase to the east of the main convective area and not the effect of inviscid convergence. Inviscid convergence is prominent in the region at which 850 mb easterly and westerly zonal wind anomalies converge along the equator, but not toward the east. Convergence fields are generally weaker for the 850 mb field than for the 1000 mb field.

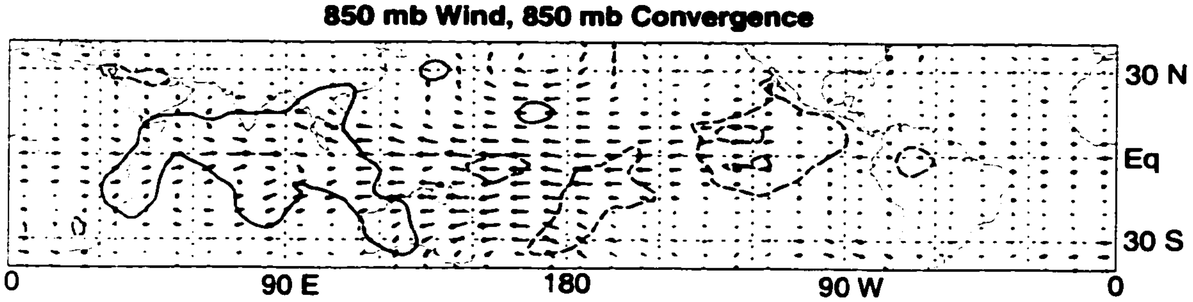

Figure 2.8. Wind anomalies at 850 mb and 850 mb convergence anomaly field for Phase 4. Contour interval is 2 x 10-7 s^{-1} starting at 1 x 10-7 s^{-1}. Wind vectors are of same magnitude as Fig 2.7.

2.4.5) Phase 5

Interesting things occur in the Indian and W. Pacific Oceans during Phase 5 (Fig 2.9). Convection at the equator in the Indian Ocean is no longer being supported by surface convergence and is consequently beginning to move off the equator accompanied by cyclonic (anticyclonic) circulations at 850 mb (200 mb) to the north and south of the equator at about 80°E. As discussed earlier, these low level cyclones and upper level anti-cyclones are characteristic of the Rossby wave response seen with the MJO. A split in the anomaly pattern is rather well shown in the 1000 mb convergence field and water vapor field. Bands of surface convergence at about 15°N and 15°S flank the equatorial divergence over the Indian Ocean. Westerly equatorial 850 mb wind perturbations and anomalous surface divergence have also started to split convection into two separate centers on either side of the equator. This same structure has been reproduced in several recent modeling studies (Wang and Rui 1990, Salby, Garcia, and Hendon 1994, Seager and Zebiak 1994, Wang and Li 1994).

To the east of the convective region, strong water vapor anomalies are now present in the W. Pacific, along with growing precipitation anomalies. It appears that the atmosphere is becoming sufficiently moistened for convection to be favored in the W. Pacific. A strong tongue of positive water vapor anomalies also extends past the dateline at about 5°N to 10°N. Weak positive precipitation anomalies are becoming apparent in this tongue of moisture anomalies. This precipitation structure resembles an ITCZ (Intertropical Convergence Zone) and is forming in the transition zone between positive and negative surface convergence anomalies. Thus, the link between this development and surface convergence is inconclusive. However, the link between surface convergence and vapor anomalies in the western Pacific is robust. The surface convergence signal now extends along the equator to South America in association with the 850 mb easterly wind perturbations. Weak water vapor anomalies are also present in the vicinity of South America. Negative water vapor anomalies and suppressed precipitation are present just to the south and west of Central America.

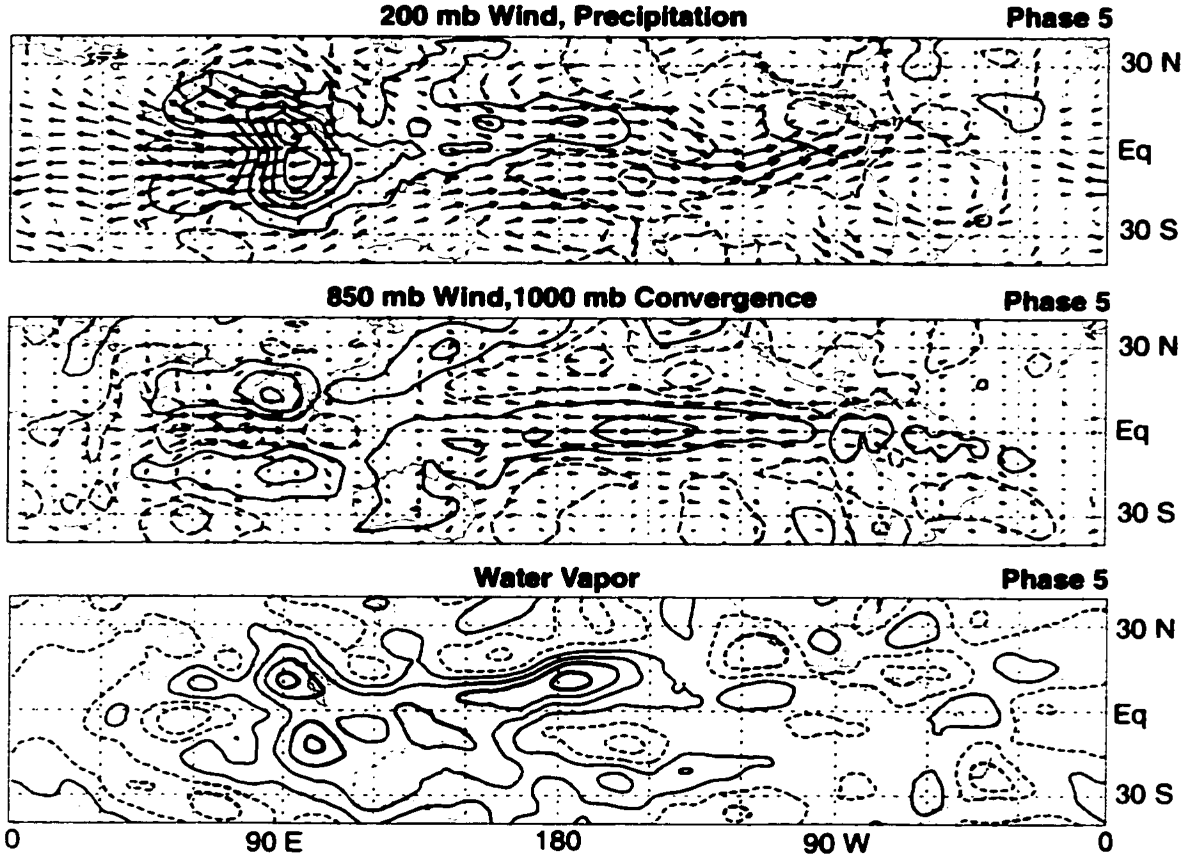

Figure 2.9. Phase 5 composites. Otherwise, same as Figure 2.3.

2.4.6) Phase 6

Phase 6 shows a rather impressive structure in the precipitation field (Fig. 2.10). The main equatorial convective anomaly has made the transition from the Indian Ocean to the Western Pacific around 130°E. Bands of precipitation at about 15°N and 15°S extending across the northern and southern Indian Ocean are associated with Rossby waves evident in both the 1000 mb convergence field and the water vapor anomaly field. Strong anticyclonic circulations at 200 mb in association with these features are readily apparent. At the equator in the Indian Ocean strong 850 mb westerly anomalies and surface divergence are present with a strong tongue of anomalously low precipitation and water vapor values extending across the Indian Ocean. Rapid drying of the atmosphere occurs in association with these westerly anomalies. Possible mechanisms for this drying were discussed in section 2.4.4.

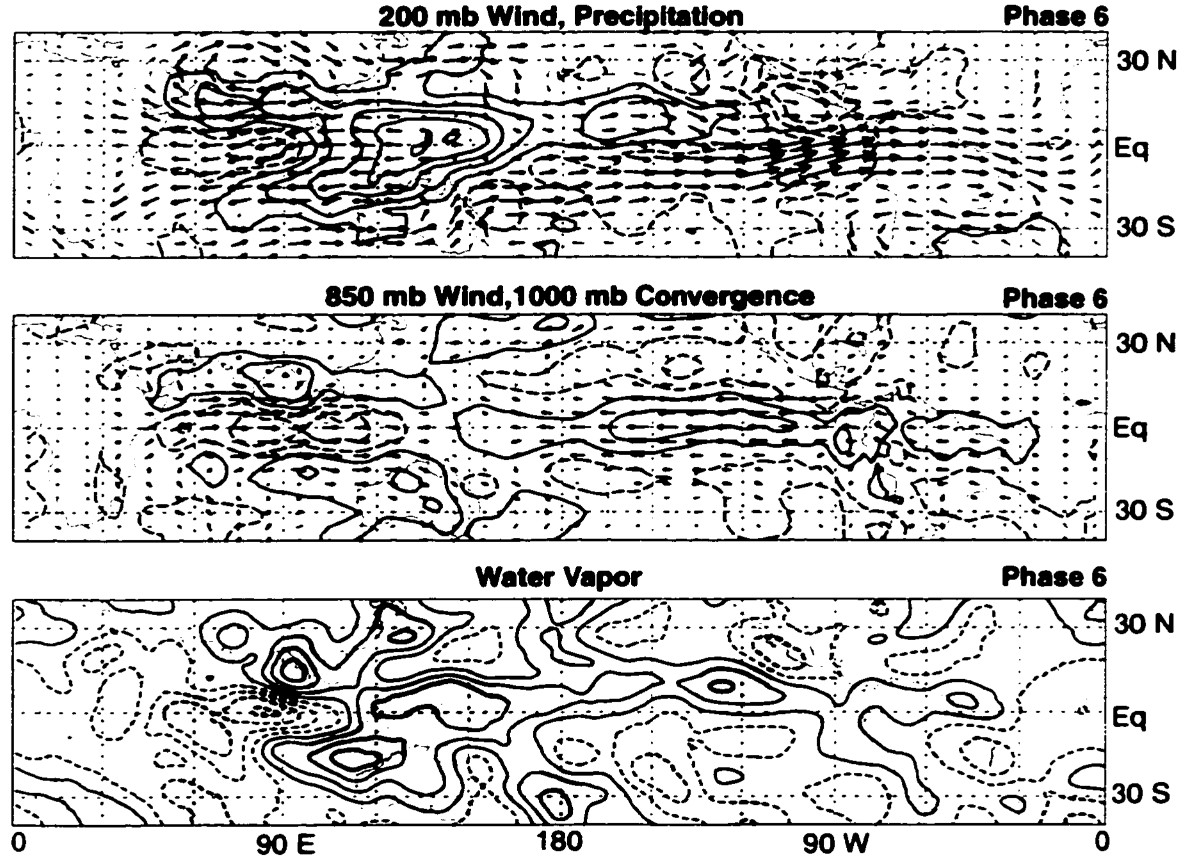

Figure 2.10. Phase 6 composites. Otherwise, same as Figure 2.3.

The main convective area is at a node in the surface convergence at 130°E, with strong convergence to the east toward South America. Strong positive water vapor anomalies are occurring along and to the north of this convergence. An ITCZ signature in the precipitation extends out to 120°W at about 5-10°N. A similar ITCZ structure was detected by Bantzer and Wallace (1996). Strong 850 mb easterly perturbations and very strong 200 mb westerly perturbations straddle the equator just to the south of the ITCZ.

The phase relationship between the precipitation signal and the water vapor signal over the western Pacific is interesting. To show this relationship, a 5° by 5° box centered at the equator and 130°E was chosen and water vapor anomalies and precipitation anomalies were plotted as a function of phase (Fig 2.11). Results from this region were typical of the western equatorial Pacific in general. Water vapor anomalies are increasing over this region after Phase 1. The precipitation anomalies only start to increase significantly after Phase 4. Positive water vapor anomalies are reached at Phase 3 preceding the onset of positive precipitation anomalies at Phase 5. The vapor anomaly peaks at Phase 5 or 6, whereas the precipitation anomaly peaks at Phase 6. After they peak, both fields decline rapidly. This suggests again that the atmosphere needs to be slowly preconditioned before convection can begin in earnest, and that the passage of the maximum in convection and large-scale wave structure quickly dries the atmosphere. Surface convergence associated

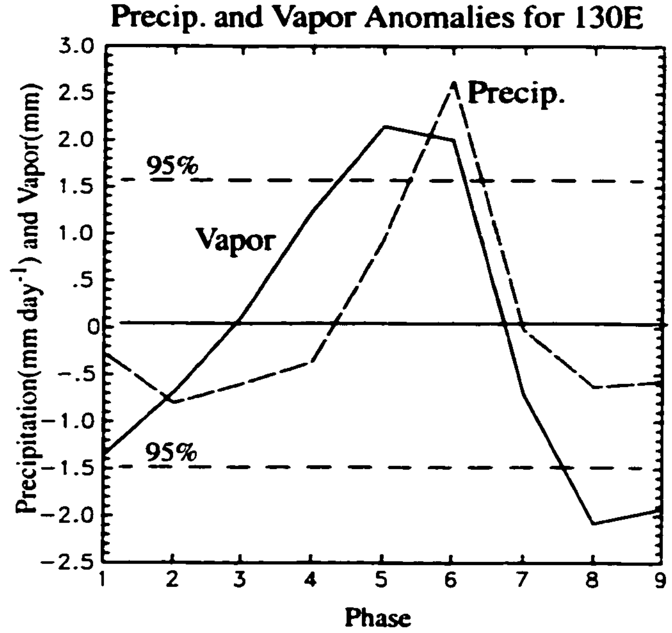

Figure 2.11. Precipitation anomalies and water vapor anomalies for the years 1988-1992 (all seasons) as a function of phase for a 5° by 5° box centered at the equator and 130°E. Precipitation (dashed) Vapor (solid). The dotted horizontal lines are the limits at which the water vapor signal is significantly different from zero at the 95% level.

with the 850 mb easterly perturbations of a Kelvin wave helps to slowly moisten the atmosphere, and rapid drying accompanies the strong 850 mb westerly anomalies of the Rossby and Kelvin wave features after the passage of convection.

2.4.7) Phase 7

At Phase 7 the convective center has shifted to 155°E with a bull's-eye of suppressed precipitation and humidity over the Indian Ocean accompanied by 1000 mb divergence (Fig. 2.12). Westerly 850 mb wind anomalies are continuing to drive into the convective area with precipitation areas to the north and south of the equator at about 120°E flanking the strong westerlies at lower levels. Strong anticyclones at 200 mb accompany these fea-

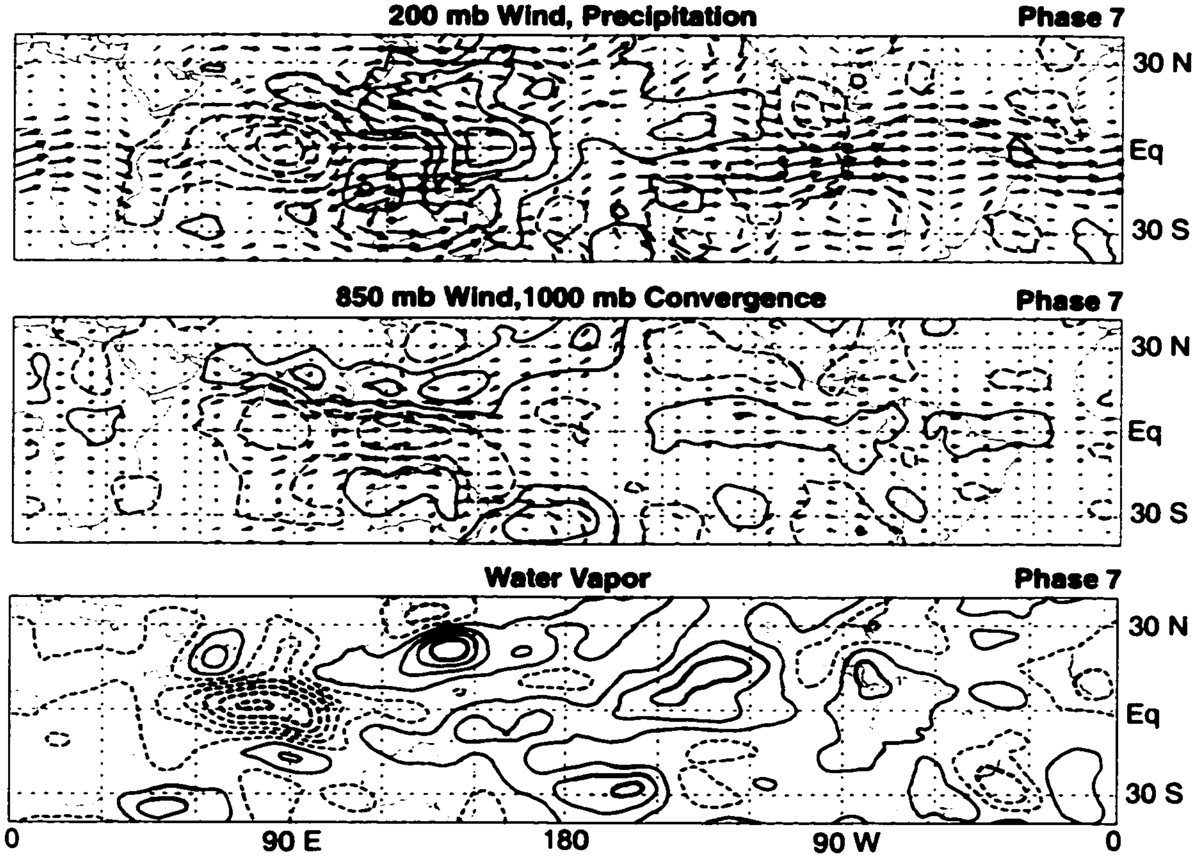

Figure 2.12. Phase 7 composites. Otherwise, same as Figure 2.3.

tures in association with Rossby waves at 130°E. A strong dry anomaly is located over the Indian Ocean to the west of the main convective area with some moist anomalies stretching eastward from the main convective area to about 110°W with additional pockets over S. America. Surface convergence has weakened over the E. Pacific Ocean along the equator and strong moist anomalies in the water vapor field are beginning to decay and become disjointed. An ITCZ still extends out to about 120°W. The main convective area is in a region of surface divergence now as the equatorial Kelvin wave begins to propagate away from the central Pacific, and 850 mb westerly wind anomalies overtake the convective area.

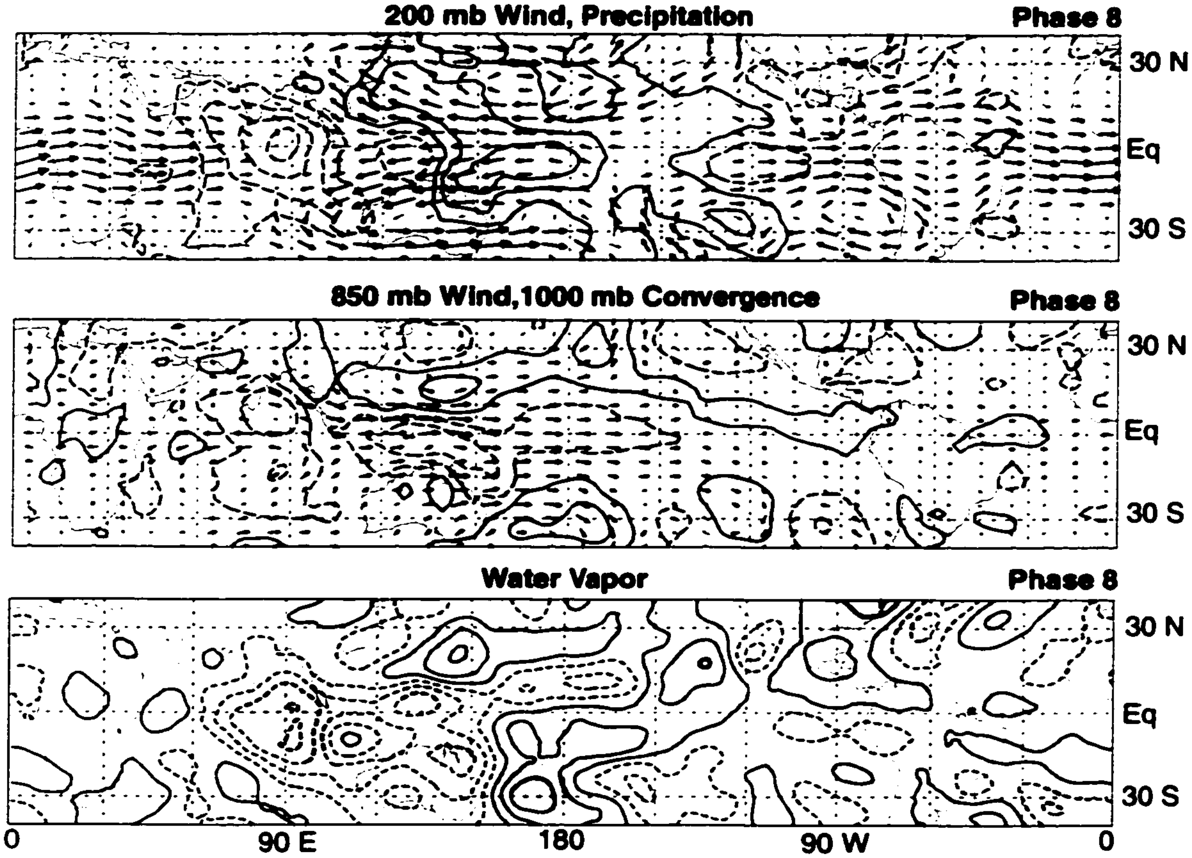

Figure 2.13. Phase 8 composites. Otherwise, same as Figure 2.3.

2.4.8) Phase 8

The convective area over the central Pacific at 170°E has weakened and the water vapor anomaly has started to become diffuse over the central and eastern Pacific (Fig. 2.13). Evidence for a positive ITCZ anomaly still remains just to the north of the equator. The dry anomaly over the Indian Ocean has expanded into the W. Pacific Ocean to about 150°E, and it is this anomaly which must be eroded in order for convection to be reestablished in the W. Pacific when the cycle in convection begins again.

In the W. Indian Ocean at about 60°E a small patch of surface convergence and a newly formed positive water vapor anomaly have appeared in a region previously inhabited by dry anomalies. Thus, the preconditioning of the atmosphere in the Indian Ocean has begun and moist anomalies are forming which are a precursor to a new convective anomaly near 80°E. Strong westerly flow anomalies at 200 mb are expanding into the W. Indian Ocean from the west.

2.4.9) Phase 9

If the MJO were periodic, Phase 9 would be identical to Phase 1. The MJO is not perfectly periodic, but Phase 9 (Fig. 2.14) shows many similarities to Phase 1, especially in the water vapor and precipitation fields. The remnants of convection are located to the east of the dateline near 10°S, which is reflected in the water vapor and precipitation fields. A strong area of positive water vapor anomalies has grown near 60°E and the equator, that is the precursor to convection in the Indian Ocean mentioned earlier. This feature is being supported by surface convergence and lies within the region of 850 mb easterly wind anomalies. Evidence exists for a weak precipitation anomaly accompanying this water vapor anomaly when the precipitation field is examined for 1988-1992 (not shown). A similar anomaly was seen in Phase 1.

Enhanced precipitation is occurring along the Mexican and Central American coast as in Phase 1, associated with convection there during the Northern Hemisphere summer. Positive moisture anomalies are also found. A tongue of surface divergence and 850 mb

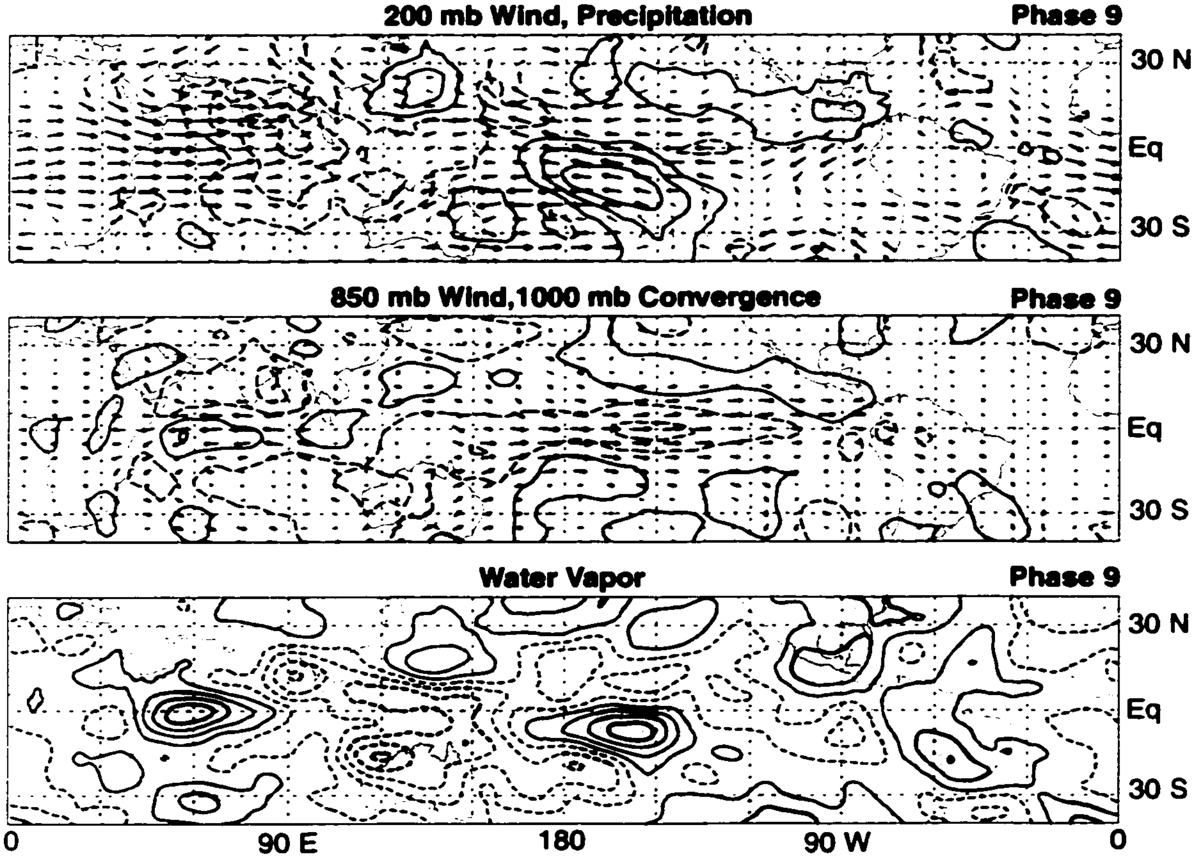

Figure 2.14. Phase 9 composites. Otherwise, same as Figure 2.3.

westerlies lies along the equator from 120°E to 90°W. Cyclonic flow at 200 mb is beginning to establish itself on either side of the equator at upper levels in the Indian Ocean region.

2.5) The Northern Hemisphere Summer

Previous studies have noted the seasonal aspects of the MJO, in particular the Indian monsoon during the Northern Hemisphere summer (see Madden and Julian 1994 for a review). Break periods of the monsoon have been attributed in part to different phases of the Intraseasonal Oscillation (e.g. Hartmann and Michelsen 1989). Using the index developed in Section 3, an enlightening picture of the MJO during Northern Hemisphere summer can be obtained. Composites of 850 mb wind anomalies and MSU precipitation anomalies for the months May-October in the Indian Ocean region are displayed in Figure 2.15. This period encompasses the Indian summer monsoon period and 43 events of the 81 total events derived in the all-season composites fall within this period. Phase 1 is very similar to Phase 9 and so only phases 2-9 are displayed in the composite picture. One need only look at Phase 9 to see how the cycle of convection is initiated. Since the MSU precipitation dataset is only available over ocean areas, precipitation values over the Indian subcontinent are either nonexistent, or reflective of nearby ocean surfaces through smoothing. However, a very good indication of the widespread precipitation anomalies over the Indian subcontinent can be inferred by examination of the precipitation fields over the Bay of Bengal and the Arabian Sea to the east and west of the Indian subcontinent. OLR data were used to support inferences about precipitation over the Indian subcontinent, but is not suitable to determine fine spatial structure.

Composites based on the equatorial 850 mb zonal wind index are very similar to those obtained by Hartmann and Michelsen (1989) (Hereafter referred to as HM) using indices based on precipitation and 850 mb zonal wind for selected observing stations around India. HM describe "active" periods of the monsoon as being accompanied by enhanced precipitation centered over central India with an associated cyclonic circulation at 850 mb. "Break" periods are accompanied by a precipitation minimum over central India with an associated anticyclonic circulation at 850 mb. Spectral analysis indicated that such variations occur on intraseasonal timescales of 40-50 days. These features in the precipitation and winds appear first over the far southern portions of the Indian subcontinent and then propagate toward the north. Precipitation anomalies terminate their northward movement and then die in place once the Himalayas are reached.

The composites in this paper provide a large-scale context for the results of HM. Convection grows along the equator from 80-90°E during Phases 2 and 3. Westerly wind perturbations at 850 mb begin to divide the convective system at Phase 4, and the resulting shear spawns a cyclonic circulation to the north of the equator at roughly 10°N with a

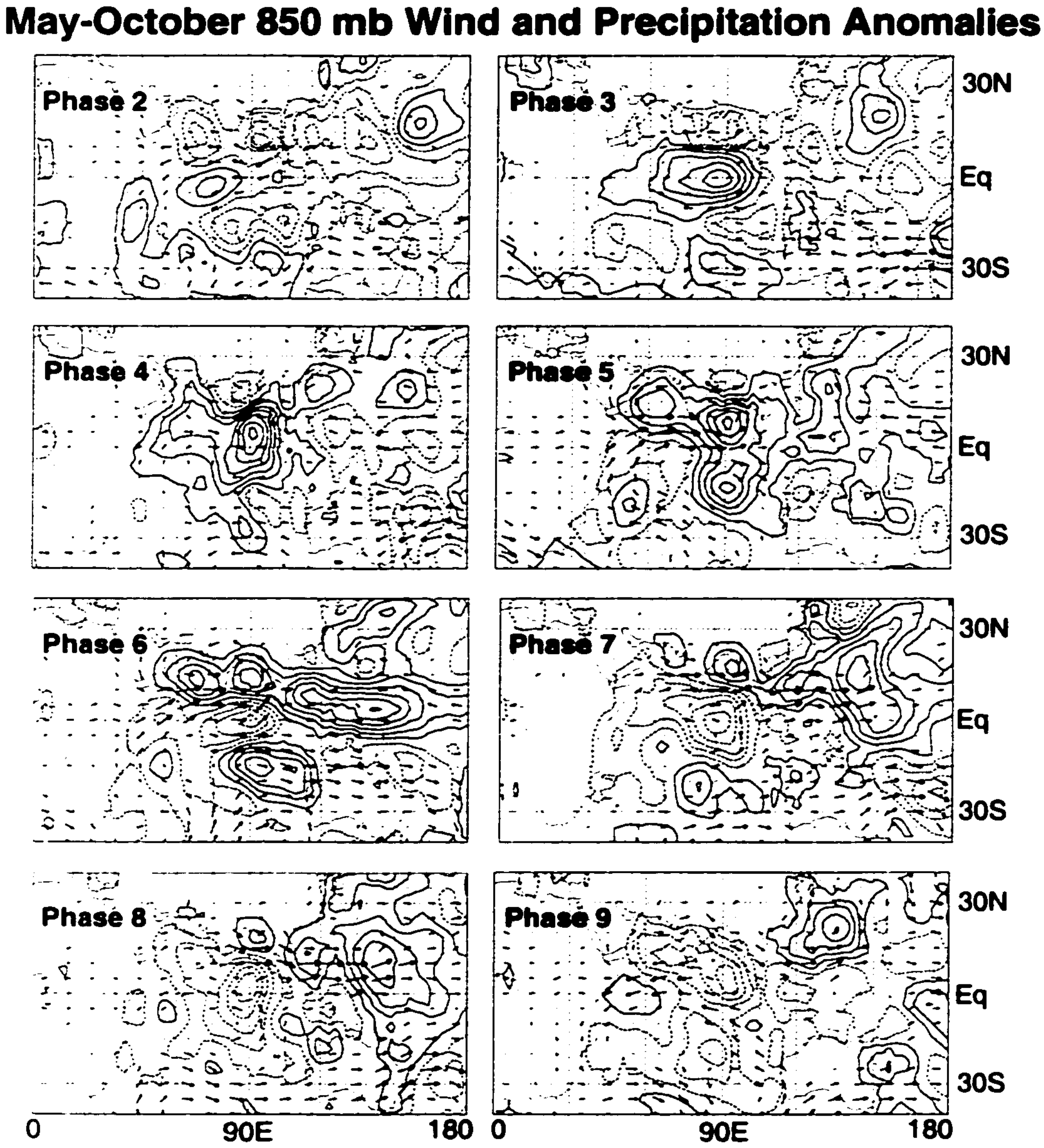

Figure 2.15. May-October 850 mb bandpassed wind anomalies and MSU precipitation anomalies as a function of phase for 1979-1995. Wind vectors significant at the 90% level are plotted in black and non-significant vectors are gray. Contours are every 0.6 mm day^{-1} starting at 0.3 mm day^{-1}. Maximum vectors are 3.3 m s^{-1}. Dashed contours are negative.

lesser circulation in the Southern Hemisphere. Precipitation anomalies have reached the southern part of India at this time. At Phase 5 the precipitation area near the equator has been completely sheared into two centers to the north and south, consistent with the drying mechanisms discussed in section 4d. Precipitation anomalies have reached central India (confirmed by the OLR signal (not shown)) and are accompanied by a strengthened 850 mb cyclone. This northward and westward propagation of Rossby waves away from the equator explains the northward propagation of the precipitation and wind anomalies seen in HM and other studies. In Phase 6, the precipitation maximum and associated cyclonic circulation over central India are consistent with the "active" monsoon period described by HM. A dry anomaly is centered over the equatorial Indian Ocean that will propagate northward to eventually provide a "break" monsoon period for India. Phase 3 is typical of such a period in that a precipitation minimum appears over central India with associated anticyclonic circulation at 850 mb. Phases 7-9 detail the northward propagation of this dry anomaly from the equator. The positive anomaly eventually dies over the north of India (confirmed by the OLR signal).

These composites paint the picture of alternating positive and negative precipitation anomaly areas and associated cyclonic and anticyclonic 850 mb wind circulations beginning in the east equatorial Indian Ocean and then propagating northward and westward across the Indian subcontinent. Weaker precipitation and wind anomaly features occur in the Southern Hemisphere during this season. This pulsation in alternating northward moving wet and dry anomalies is a rather robust feature independent of the portion of the NH summer record examined and provides compelling evidence in locking at least some of the intraseasonal variability associated with the Indian monsoon to the phases of the MJO. This same type of feature, sometimes described as a "northward moving cloud bank" when associated with an active monsoon period, has been observed in numerous studies (see Madden and Julian 1994). The timing of the monsoon onset may also be affected by the phase of the MJO, so that the MJO may be important for Indian agriculture (Webster 1987).

2.6) Conclusions

A composite lifecycle of the Madden-Julian Oscillation based on an 850 mb equatorial averaged zonal wind index has shown that convergence in the boundary layer due to friction plays a key role in the evolution of the Madden-Julian Oscillation. The large scale structure of the MJO is that of a coupled Kelvin-Rossby wave, with wavenumber 1 structure along the equator at upper levels. Equatorial Kelvin wave theory indicates that regions of 850 mb easterlies are accompanied by negative pressure perturbations at the surface and that positive pressure perturbations occur below 850 mb westerlies. Thus, frictional moisture convergence takes place near the surface beneath 850 mb easterly perturbations, and divergence of moisture occurs beneath 850 mb westerly perturbations. The convective complex associated with the MJO generally has moisture convergence in the boundary layer lying along the equator to the east, and divergence to the west. Subsidence or horizontal advection from the west or extratropics associated with Rossby wave circulations may also contribute to drying to the west of convection Convergence at 850 mb is more bound to the regions of maximum convection (Fig. 2.7 vs. Fig. 2.8). This phase lag between regions of inviscid convergence and frictional convergence has been noted in other studies (e.g. Hendon and Salby 1994).

Frictional convergence acts to moisten the atmosphere in regions which had been dried out by the previous cycle of convection. A significant correlation exists between surface convergence and positive water vapor anomalies over the W. Pacific and Indian Oceans with surface convergence leading water vapor in time (Fig. 2.6). Convergence at 850 mb has a weaker correlation and lags water vapor over the W. Pacific Ocean. The time required for the formation of new convection in a region may be determined by the amount of time it takes surface convergence to reestablish a certain level of moisture. As a prime example, dry anomalies in the western Pacific to the east of the growing area of convection in the Indian Ocean are subjected to a period of moisture convergence (Figs. 2.4, 2.5, 2.7). The timescale required for convection to shift into the Pacific may be set by the time it takes frictional convergence to sufficiently moisten the atmosphere. Positive water vapor anomalies precede the development of positive precipitation anomalies in areas east of the main convection (Fig 2.11). Additionally, water vapor anomalies peak in many areas of the W. Pacific before the peak precipitation is observed. A similar process occurs for the onset of convection in the Indian Ocean. Curiously, in the Indian Ocean the main convective area forms to the east of where the initial perturbation in the moisture field is located (Fig. 2.3 vs. Fig. 2.5).

Rossby wave circulations propagate poleward and westward away from the main convective areas of the Indian and W. Pacific Oceans, and accelerate the westerly flow at 850 mb along the equator. This 850 mb westerly flow associated with both the Kelvin and Rossby wave components dries out the equatorial region of the Indian Ocean rapidly, ending convection there. The convection then shifts off the equator with the Rossby components while a second convective center is forming in the western Pacific Ocean. Anticyclonic flow at 200 mb and cyclonic flow at 850 mb are characteristic of these Rossby waves (Figs. 2.9, 2.10). Rossby wave features of the opposite polarity are observed in association with dry periods of the oscillation.

During the Northern Hemisphere summer, the Indian monsoon seems intimately tied to phases of the MJO. The northward propagation of precipitation across India during the summer monsoon is associated with northward and westward movement of Rossby wave features trailing the main center of equatorial convection associated with the MJO. "Break" and "active" phases of the Indian monsoon seem to be tied to the phases of the MJO. Cyclonic winds at 850 mb accompany "active" periods, while anticyclonic winds accompany "break" periods. The composites obtained are consistent with the fields described in Hartmann and Michelsen (1989).

3) The Sensitivity of CCM3 Intraseasonal Variability to Convection Scheme

This chapter describes work submitted to the *Journal of Climate* (Maloney and Hartmann 2000c). Figure 3.1 is the only significant addition to the analysis in that paper.

3.1) Introduction

The Madden-Julian oscillation (MJO), or tropical intraseasonal oscillation, is a dominant mode of variability in the tropical troposphere with characteristic eastward periods of 30-60 days (Madden and Julian 1994, Hendon and Salby 1994). The oscillation has a mixed Kelvin-Rossby wave structure over the Indian and western Pacific oceans, where the circulation is strongly coupled to convection and propagates slowly eastward. Kelvin wave structure with more rapid eastward propagation is characteristic in regions away from convection. Winds at 200 mb are out-of-phase with those at 850 mb. Amplitude over the western Pacific and Indian Oceans peaks during December-May.

Atmospheric general circulation models (GCMs) have had difficulty in simulating the observed characteristics of the MJO. Many GCMs are able to simulate eastward propagating equatorial zonal wind signals. The vast majority, however, produce intraseasonal signals with unrealistically high phase speeds in convective areas, periods that are too low (< 30 days), and unrealistically low amplitudes (Park et al. 1990, Slingo et al. 1996). Most models also do not capture the seasonality of the signal. Models that employ convective schemes closed on buoyancy tend to produce better intraseasonal oscillations than those closed on moisture convergence (Slingo et al., 1996). Other methods have been suggested for improving intraseasonal variability in GCMs. Flatau et al. (1997) and Waliser et al. (1999) suggest that coupling an atmospheric GCM to a simple slab ocean model may increase intraseasonal variability, and slow the eastward propagation of equatorial wave disturbances. Wang and Schlesinger (1999) find that a relative humidity threshold for initiation of convection may increase intraseasonal variability with certain convection schemes. Raymond and Torres (1998) suggest that convective parameterizations must properly simulate convection of low precipitation efficiency during dry regimes to properly moisten the mid-troposphere for MJO deep convection events.

This study will analyze intraseasonal variability in the National Center for Atmospheric Research (NCAR) Community Climate Model, version 3.6 (CCM3) (Kiehl et al. 1998). As we will show later, the standard CCM3 deep convection parameterization of Zhang and McFarlane (1995) produces tropical intraseasonal variability in zonal winds and precipitation with amplitude much weaker than observed. The intraseasonal variability of the model can be improved with alternate deep convection schemes. We will compare the performance of four quasi-equilibrium type schemes in the CCM3 (Table 1). Quasi-equilibrium schemes assume that convection is controlled by the rate at which instability is supplied by the large-scale environment. The timescale for convection is much less than the timescale at which the instability is created (Manabe and Strickler 1964, Arakawa and Schubert 1974, Emanuel 1986). The four schemes we use in this study relax the atmosphere toward a stable state rather than remove the instability instantly. The convective parameterizations are described in section 2. The microphysics of cloud with relaxed Arakawa-Schubert (McRAS) scheme of Sud and Walker (1999a) gives the best MJO simulation in both zonal winds and precipitation.

Table 3.1. Quasi-equilibrium convection schemes.

Configuration	Deep Convection Scheme	Description
1	Zhang and McFarlane (1995)	Mass flux scheme with saturated downdrafts
2	Hack (1994)	Three level adjustment (triplet) cloud model
3	Emanuel and Zivkovic-Rothman (1999)	Buoyancy sorting with unsaturated downdrafts
4	Moorthi and Suarez (1993) with Sud and Walker (1999a) (McRAS)	Relaxed Arakawa-Schubert scheme with prognostic cloud water, RH threshold, and evaporation of convective precip. in unsaturated downdrafts and the environment.

Convective downdrafts have been observed to significantly affect the lower tropospheric temperature and moisture budgets of tropical convective systems (Betts 1976, Zipser 1977, Houze 1977). Although downdrafts cool and dry the lower troposphere immediately near convection, they promote a cooler and moister mean tropical lower troposphere due to weaker compensating subsidence away from convection (Johnson 1976, Cheng 1989). The parameterization of convective precipitation evaporation and convective downdrafts has been shown to improve the simulation of convection by cumulus parameterizations (e.g. Garstang and Betts 1974, Kao and Ogura 1987). Molinari and Corsetti (1985) found that parameterizing convective downdrafts is essential for realistically simulating the lifecycle of a mesoscale convective system. Sud and Walker (1993) and Seager and Zebiak (1995) found that including convective downdrafts in their models improves the mean simulation of tropical convection. Models with realistic mean states of convection are more likely to produce realistic intraseasonal oscillations (Slingo et al 1996).

Convective evaporation may also help to precondition the tropical atmosphere for deep MJO convection. After stabilization of the atmosphere by the passage of an MJO convective event, the troposphere needs to be sufficiently destabilized before the recurrence of deep convection (Bladé and Hartmann 1993, Hu and Randall 1994, Maloney and Hartmann 1998). Radiative cooling aloft and moistening of the lower and middle troposphere by shallow and mid-level convection may contribute to this destabilization (Raymond and Torres 1998). The evaporation of convective rainfall in unsaturated air may also contribute toward moistening the lower troposphere for more intense convection. Boundary layer relative humidity thresholds for the initiation of convection parameterize the requirement of lower tropospheric preconditioning in a simple manner (Wang and Schlesinger 1999). Convective downdrafts can also help stabilize the boundary layer after a strong MJO convective event by transporting air of low moist entropy to lower levels. Rain evaporation in tropical mesoscale convective systems has been observed to stabilize the lower troposphere (e.g. Leary and Houze 1979).

The McRAS convection scheme includes a relative humidity threshold for initiation of convection, and a parameterization of convective rain evaporation and unsaturated downdrafts. We will show that the simulation of intraseasonal variability in CCM3 with McRAS is very sensitive to the rain evaporation and downdraft parameterization. The simulation of MJO variability is not improved through use of a boundary layer relative humidity threshold, and is in fact degraded if the threshold is set too high. The McRAS convection scheme also contains prognostic cloud water. Cloud mass fractions are allowed to entrain, advect horizontally and vertically, diffuse, evaporate, and condense with a detailed parameterization of cloud microphysics. The treatment of cloud water as a prognostic variable rather than a diagnostic variable can improve the simulation of deep convection and atmospheric temperature and moisture profiles (e.g. Randall 1989, Tiedtke 1993, Del Genio et al. 1996, Das et al. 1998). Our experiments indicate that the simulation of intraseasonal variability in CCM3 with McRAS is not sensitive to prognostic cloudwater, and so results examining prognostic cloud water will not be presented here.

Section 2 will describe the CCM3, the four convection parameterizations, and the model experiments. Section 3 will compare the intraseasonal variability of the CCM3 using the four different convective schemes. Section 4 examines a composite MJO lifecycle in CCM3 with McRAS convection. Section 5 examines the sensitivity of CCM3 with McRAS convection to relative humidity threshold and the evaporation of convective precipitation with unsaturated downdrafts. Conclusions are presented in section 6.

3.2) The CCM3 and Quasi-Equilibrium Convection Schemes

3.2.1) The NCAR CCM3

The standard version of the NCAR CCM3 used here is a global spectral atmospheric GCM with T42 horizontal resolution (a roughly 2.8° x 2.8° Gaussian grid) and 18 levels in the vertical. The top of the model is at 2.9 mb. The model time step is 20 minutes. Deep convection is simulated by the mass-flux scheme of Zhang and McFarlane (1995), and the triplet convective scheme of Hack (1994) simulates shallow convection. The mean simulation of tropical convection is much improved over that of CCM2 which uses the Hack (1994) scheme for deep convection (Hack et al. 1998), but overall convective variability is reduced. See Kiehl et al. (1998) for a complete description of the CCM3.

3.2.2) Quasi-equilibrium convection parameterizations

We compare the performance of the CCM3 at intraseasonal timescales using four different deep convection schemes: Zhang and McFarlane (1995), Hack (1994), Emanuel and Zivkovic-Rothman (1999), and Sud and Walker (1999a, McRAS). Relaxation timescales for convection of one hour were used for all schemes except for the Emanuel scheme. For the Emanuel scheme, the relaxation parameters were set to the values prescribed in Emanuel and Zivkovic-Rothman (1999).

The Zhang and McFarlane (1995) parameterization is a mass flux scheme inspired by the convective parameterization of Arakawa and Schubert (1974). An updraft ensemble of entraining convective plumes, all having the same mass flux at cloud base, relaxes the atmosphere toward a threshold value of convective available potential energy (CAPE). Results are not sensitive to the threshold used. In-cloud *saturated* downdrafts commence at the level of minimum moist static energy. The effects of these downdrafts are generally weak. Detrainment of ascending plumes also begins at the level of minimum moist static energy. Therefore, only ascending plumes that can penetrate through the conditionally unstable lower troposphere are present in the ensemble. The Hack scheme (described next) accompanies the Zhang scheme for simulation of shallow convection.

The Hack (1994) triplet cloud model was implemented in CCM2 as the primary deep convection scheme. The scheme uses a simple cloud model based on a triplet, in which convective instability is assessed for three adjacent layers in the vertical. If a parcel of air in the lower layer is more buoyant than one in the middle layer, adjustment occurs. The mass flux is related to the parcel buoyancy and an autoconversion parameter, and is modified by a relaxation timescale. Detrainment occurs at the highest level. After adjustment occurs for three levels, the triplet moves up one level and the process is repeated.

The Emanuel scheme (Emanuel and Zivkovic-Rothman 1999) is a buoyancy sorting scheme. Parcels ascend undiluted from cloud base to upper levels, where mixing with the environment and precipitation formation occurs. The mixed parcels then ascend or descend according to their buoyancy. Detrainment occurs at the level where the liquid water potential temperature equals that of the environment. Relaxation parameters and CAPE determine the rate of adjustment per time step toward equilibrium. Both saturated and unsaturated downdrafts are simulated.

The relaxed Arakawa-Schubert (RAS) scheme of Moorthi and Suarez (1992) relaxes the atmosphere toward equilibrium by adjustment through an ensemble of entraining plumes. Adjustment is initiated when the critical value of the cloud work function (a measure of the buoyancy of lower tropospheric parcels, see Appendix B) for a particular cloud type is exceeded. Cloud types are distinguished by differing entrainment parameters. The version of RAS we use includes modifications made by Sud and Walker (1999a, McRAS). McRAS has a relative humidity threshold (RH_c) for initiation of convection, where cloud base is determined to be the lowest level in the atmosphere between 700 mb and 960 mb that satisfies RH_c. We use an RH_c of 0.81 in the control simulations of McRAS. Evaporation of convective precipitation in unsaturated environmental air is included in McRAS following Sud and Walker (1993). Convective rainfall in each cloud is partitioned between the convective core and lighter precipitation areas. Convective downdrafts driven by evaporation are generated in the regions with the most intense rainfall, where about one-third of the total rain generation occurs. An evaporation efficiency parameter determines the fraction of the total possible evaporation that occurs in a layer (Kessler 1969). Downdrafts commence near the level of minimum moist static energy and crash at the surface, displacing boundary layer air upward. The cloud regions with lighter convective rainfall (such as below the anvil) also experience evaporation, but do not experience downdrafts. A third major modification in McRAS is the inclusion of a prognostic cloud water scheme. Cloud liquid water values and cloud fractions are retained as prognostic variables at each time step. Explicit cloud microphysics act on the cloud variables. Clouds advect, convect, and diffuse in the horizontal and vertical. Due to computational constraints, we use the standard CCM3 radiation scheme in our simulations, which does not directly interact with cloud microphysics. Cloud properties required by the radiation scheme are diagnosed at each radiation time step. A different model climate may result from using a radiation parameterization that explicitly interacts with the prognostic cloud-water scheme.

3.2.3) Perpetual March simulations of CCM3

Four-year perpetual March simulations with full topography were conducted for each of the four convection schemes. Results are insensitive to increasing the length of the simulation. Results become increasingly subject to sampling variability as the length of the simulation is shortened, and may not generalize well. March is the month of maximum amplitude of the MJO over the western Pacific and Indian Oceans (Salby and Hendon 1994). Perpetual March simulations enable us to adequately sample the most active month of intraseasonal variability within the time constraints imposed by computational requirements. Insolation is fixed at its March 15 distribution. The monthly mean sea surface temperature (SST) climatology for March, described by Shea et al. (1992), is used for the ocean surface (Figure 3.1). Mean March stratospheric ozone values are specified for use in radiative transfer calculations. Although a perpetual March simulation does not have seasons, we will use the word "intraseasonal" to describe variability with periods between 20 and 80 days.

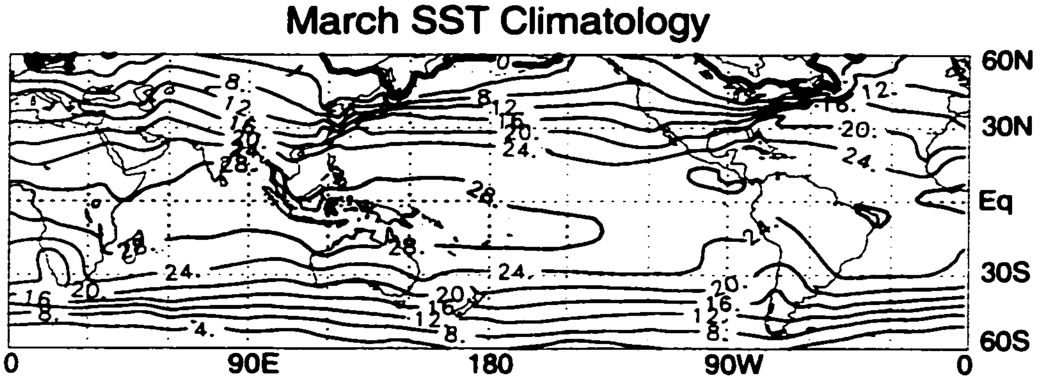

Figure 3.1. March SST climatology used in the model simulations. The values over land are interpolated from nearest ocean points, and have no meaning.

3.3) Intraseasonal Variability Intercomparison

3.3.1) Data

Observed 850 mb zonal wind and precipitation fields are compared to CCM3 generated fields to determine the model performance at intraseasonal timescales. National Centers for Environmental Prediction (NCEP)- National Center for Atmospheric Research (NCAR) gridded ($2.5^{o}x2.5^{o}$) pentad reanalysis data (Kalnay et al 1996) are used for 850 mb zonal wind. Data were available during 1979-1997. Xie and Arkin (1996) merged gridded ($2.5^{o}x2.5^{o}$) precipitation data in pentad format were available during 1979-1996. This dataset includes both land and oceanic precipitation.

3.3.2) Model performance

Slingo et al. (1996) found that GCMs with the most realistic intraseasonal variability generally have realistic mean states. Figure 3.2 compares the Xie/Arkin March precipitation climatology to climatologies from the CCM3 perpetual March simulations using varying convection schemes. Strictly speaking, a direct comparison cannot be made between a perpetual March simulation climatology and a March climatology derived from observations. In nature, SSTs vary within the month of March, and so we should not expect the simulation of tropical convection to exactly match the long-term March climatology. A comparison between the perpetual March simulations and observed March climatologies should indicate the general quality of the simulation, however.

Note that we only show the *convective* precipitation climatology from the Emanuel scheme here. The CCM3 with the Emanuel scheme has a problem with excessive large-scale precipitation in tropical areas. Large-scale precipitation magnitudes can be four times the value of the convective precipitation. Consequently, total precipitation is unrealistically high over many regions of the tropics. Inadequate boundary layer resolution in the CCM3 may be responsible for the poor simulation of mean tropical precipitation with the Emanuel scheme (Kerry Emanuel, personal communication). This deficiency should be noted as a caveat when examining intraseasonal variability results from the CCM3

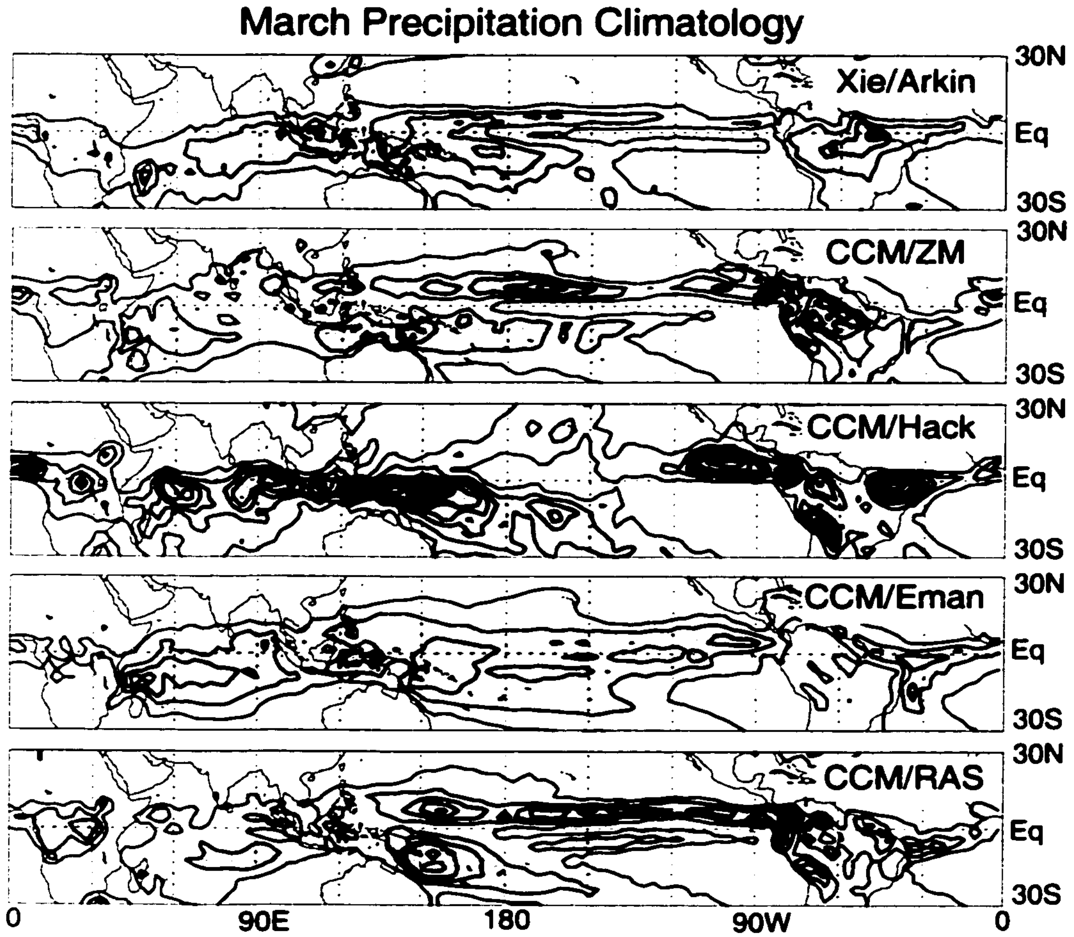

Figure 3.2. March precipitation climatology. a) Observed mean March precipitation from Xie/Arkin and the mean precipitation from the four 4-year perpetual March CCM3 simulations using b) the Zhang/McFarlane, c) Hack, d) Emanuel, and e) McRAS convective schemes. Only convective precipitation is displayed for the Emanuel convective scheme. The contour interval is 3 mm day^{-1}. Values greater than 6 mm day^{-1} are shaded.

Emanuel simulation. The Emanuel scheme may perform significantly better in higher resolution versions of the model.

Both the McRAS scheme and the Zhang/McFarlane (ZM) scheme produce reasonable March precipitation distributions. A somewhat stronger than observed ITCZ signature occurs with both schemes over the tropical Pacific, and mean precipitation tends to be somewhat weaker than observed over the Indian Ocean. Tropical land precipitation over

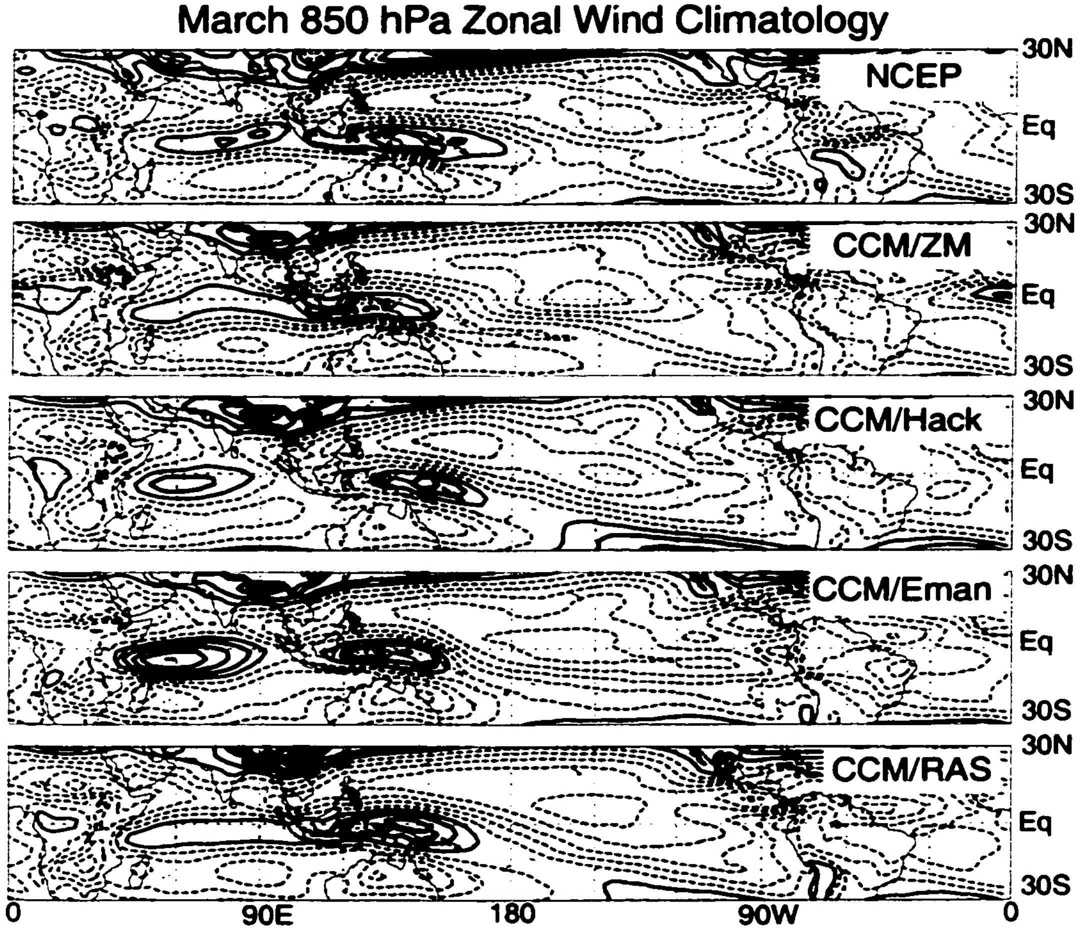

Figure 3.3. March 850 mb zonal wind climatology from model and observations. Observations are derived from NCEP. The contour interval is 2 m s^{-1} starting at 1 m s^{-1}. Values greater than 1 m s^{-1} are shaded. The zero contour is not shown.

South America and Africa is also somewhat more intense. Although McRAS and ZM produce similar mean precipitation, subsequent results will show that their simulations of intraseasonal variability are vastly different. The Hack scheme tends to produce excessive precipitation over the western Pacific, especially near the Maritime continent. Mean precipitation to the north of the equator in the intertropical convergence zone (ITCZ) tends to be too low. Tropical land precipitation tends to be too intense in isolated pockets. The convective precipitation distribution with the Emanuel scheme tends to be too diffuse across the tropics, although magnitudes over the western Pacific warm pool are realistic.

Figure 3.3 shows March 850 mb zonal wind climatologies from NCEP reanalysis and from the CCM3 simulations. The McRAS and ZM schemes do a reasonable job of reproducing the observed mean equatorial 850 mb westerly winds from the Indian Ocean into the western Pacific, with easterlies over the eastern tropical Pacific. The Hack and Emanuel schemes produce westerlies over the Indian and western Pacific Oceans that are less widespread than in observations. Mean westerlies with the Emanuel scheme are also too intense.

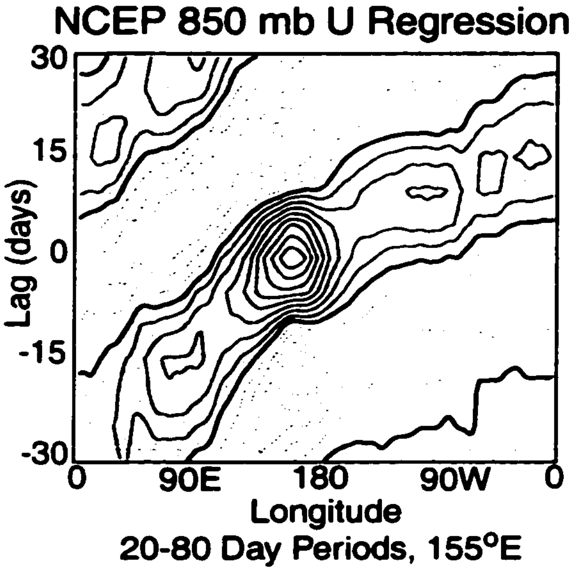

Figure 3.4. Lag regression plot of the NCEP 850 mb zonal wind averaged from 10°N to 10°S as a function of longitude. The reference time series is at 155° E. Winds were band-pass filtered to 20-80 days. December-May data during 1979-1997 are used. Contours are plotted every 0.2 m s^{-1}. Positive values are shaded.

Figure 3.4 shows a lag-regression plot of intraseasonal equatorial 850 mb NCEP reanalysis zonal wind. Data during December-May were used in the regression. The December-May period corresponds to the months of maximum MJO amplitude over the western Pacific and Indian Oceans (Salby and Hendon 1994). Zonal winds at 850 mb were filtered to 20-80 days, averaged from 10°N to 10°S at every equatorial longitude,

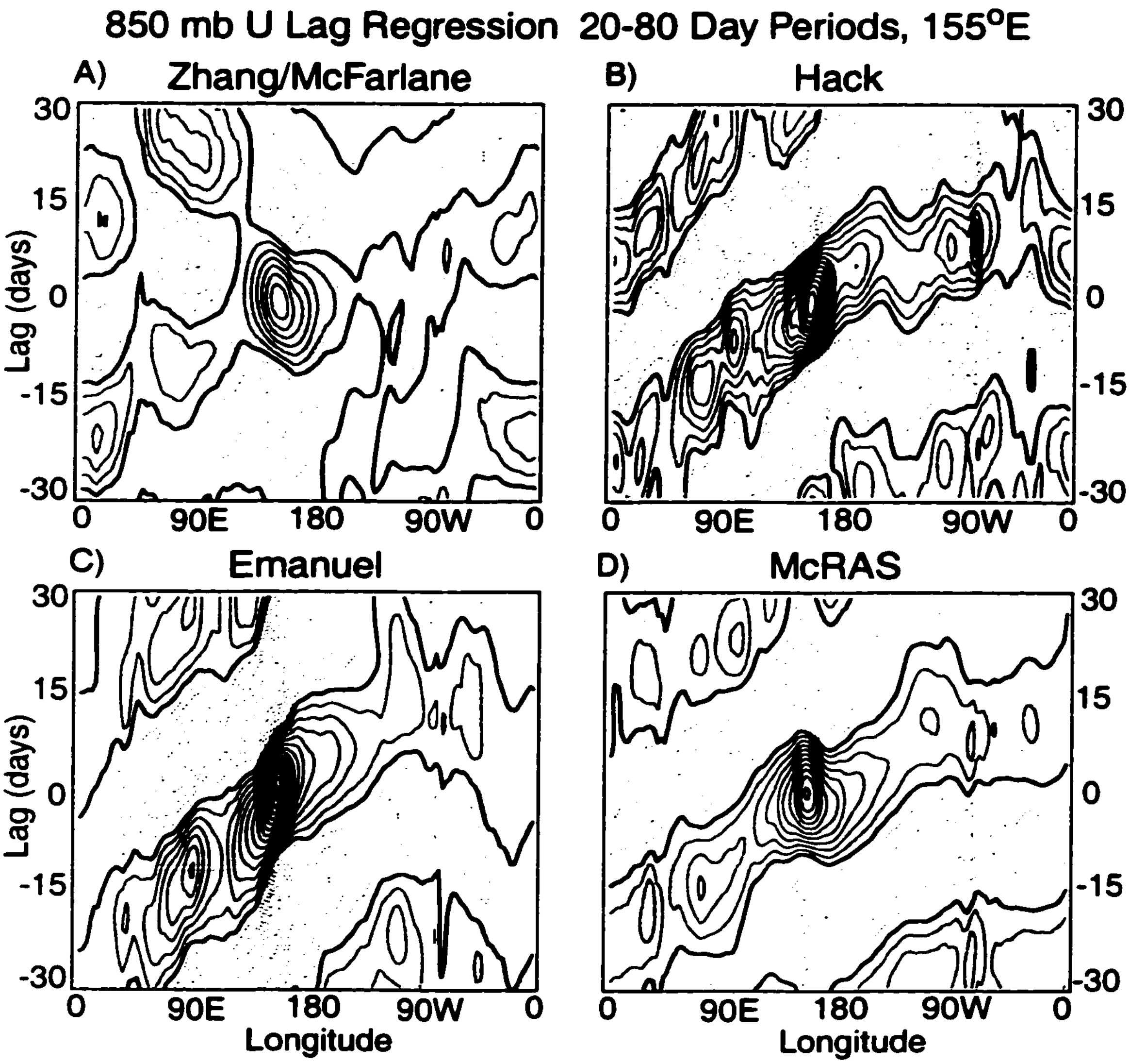

Figure 3.5. CCM3 lag regressions. Same as Fig. 3.4, except for perpetual March CCM3 simulations with the a) Zhang/McFarlane, b) Hack, c) Emanuel, and d) McRAS scheme.

and then regressed onto the zonal wind timeseries at 155°E. A lag-regression analysis can give information on the propagation characteristics and amplitude of zonal wind signals along the equator at intraseasonal periods. Slow eastward propagation of zonal wind anomalies at about 6-7 m s^{-1} occurs from the Indian Ocean (~70°E) to just past the date-line. More rapid eastward propagation occurs outside of these areas. The regions of slow eastward phase speed correspond to where the zonal wind signal is strongly coupled to convection. The wind signal near 120°W lags the signal over the Indian Ocean by about 30 days.

Figure 3.5 shows lag-regression plots for zonal wind from the perpetual March CCM3 integrations with the ZM, Hack, Emanuel, and McRAS schemes, which can be compared to the observations in Figure 3.4. The ZM convective scheme shows only a weak eastward propagating signal. Time-longitude diagrams (not shown) do show some fast eastward propagation of zonal wind signals outside of convective areas. No consistent eastward propagation is present over the western Pacific and Indian Oceans, however. The Hack and Emanuel schemes produce eastward propagating signals with amplitudes generally stronger than observed, but with realistic phase speeds. The McRAS scheme produces realistic eastward propagating signals with slightly faster than observed phase speeds and slightly lower than observed amplitudes over warm pool convective areas. Both the Hack and McRAS schemes show evidence of a change in propagation speed between the western and eastern Pacific Oceans. The Emanuel scheme shows little coherent eastward propagation outside of warm pool convective areas. Results for upper tropospheric levels are similar.

Averaged wavenumber-frequency spectra for observed equatorial (10°N-10°S) 850 mb zonal winds and precipitation are plotted in Figure 3.6. All seasons were used in computation of the spectra in order to obtain a reasonably small bandwidth. Using all seasons may tend to smooth the spectra obtained since intraseasonal variability in the tropics may have spatial and temporal characteristics dependent on season (Madden 1986, Hartmann et al. 1992). The annual cycle was removed before computation. An averaged spectrum is derived from individual spectra that are 64 pentads in length, overlapping each other by 50 pentads. The averaged spectra are not sensitive to the number of overlapping pentads. A Hanning window was applied in the temporal domain, although results do not differ from using a window function constant in time. The zonal wind spectrum is dominated by power at wavenumber one and eastward periods of 30-80 days. The precipitation spectrum is also dominated by eastward periods of 30-80 days, with power concentrated at

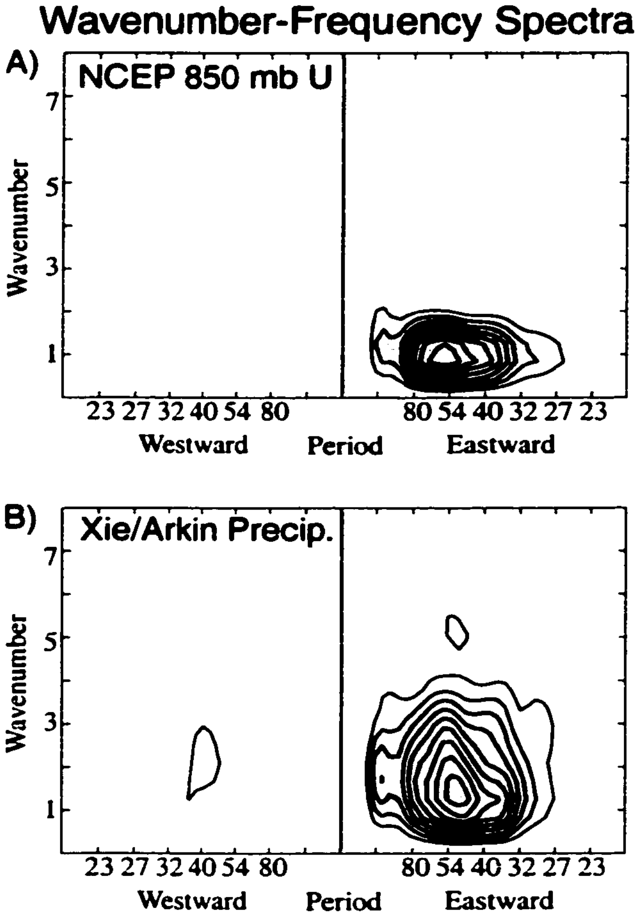

Figure 3.6. Observed wavenumber-frequency spectrum of 10°N to 10°S averaged a) NCEP 850 mb zonal wind and b) Xie/Arkin precipitation. Data during 1979-1997 (1979-1996) are used for the zonal wind (precipitation) spectrum. The zonal wind spectrum contour interval is 2.5 m^2s^{-2} starting at 6.0 m^2s^{-2}. Values greater than 8.5 m^2s^{-2} are shaded. The precipitation contour interval is 1.5 mm^2 day^{-2} starting at 4.5 mm^2 day^{-2}. Values greater than 6.0 mm^2 day^{-2} are shaded.

wavenumbers 1-3. The maximum values in both spectra occur near periods of 50-60 days and wavenumber 1. These results are consistent with those of Salby and Hendon (1994).

Figure 3.7 shows 850 mb zonal wind spectra for the perpetual March CCM3 simulations. Although perpetual March simulations were conducted, frequencies characteristic of the annual cycle and lower were removed from the data for consistency with the

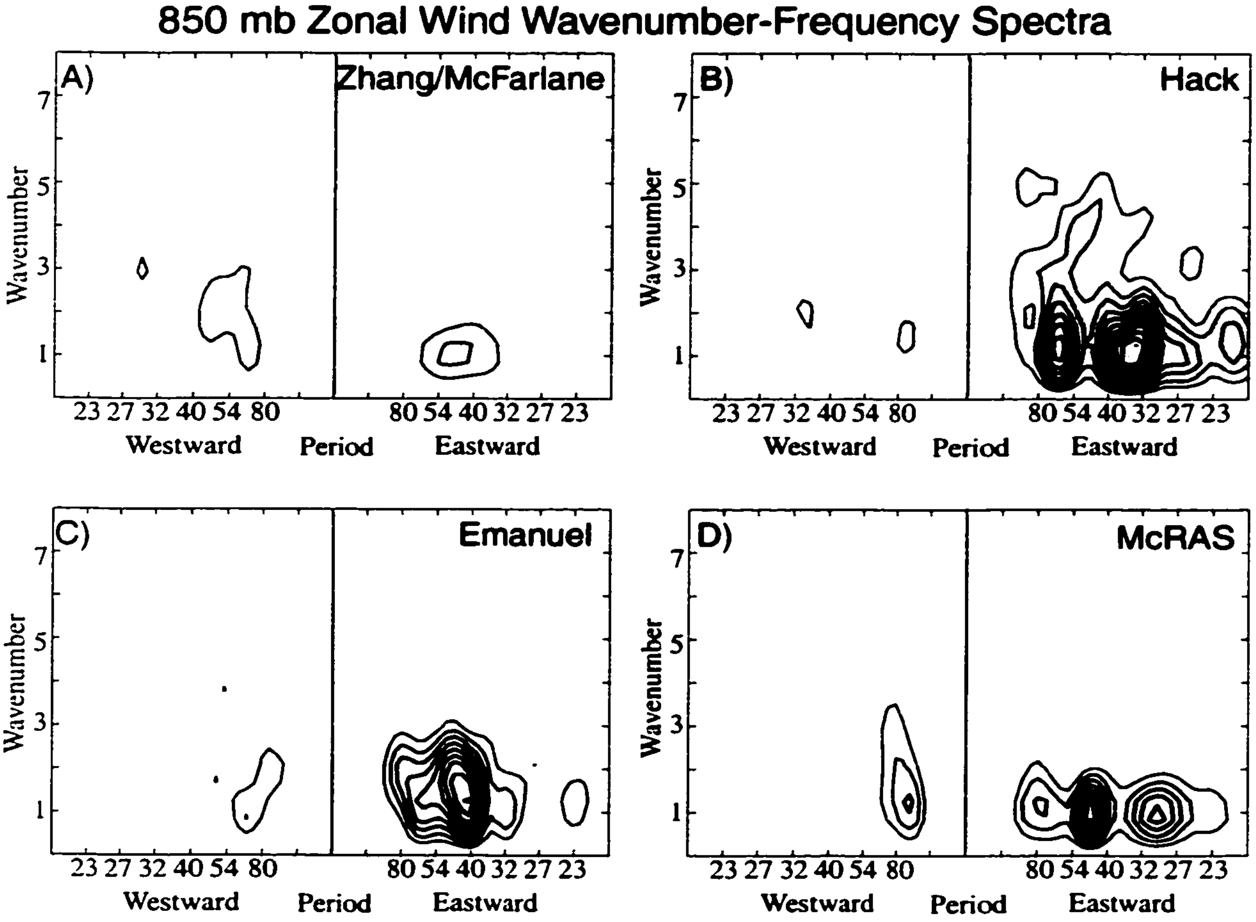

Figure 3.7. CCM3 zonal wind spectra. Same as Fig.3.6a, except for the perpetual March CCM3 simulations with the a) Zhang/McFarlane, b) Hack, c) Emanuel, and d) McRAS scheme.

observed spectrum. Model timeseries were converted to pentad format before calculation of the spectra to make a direct comparison with observations. All model simulations show a preference for eastward propagating disturbances. The ZM scheme produces much less variance at intraseasonal timescales than observations. The McRAS, Hack, and Emanuel schemes produce improved intraseasonal power over ZM convection scheme with magnitudes comparing favorably with observations. All tend to have the highest power at slightly higher frequencies than observed. The McRAS simulation has power concentrated at wavenumber 1, peaking at 40-50 days. Intraseasonal variance is high at both wavenumbers 1 and 2 with the Hack and Emanuel schemes. The highest power in the Hack scheme is at 30-40 days and wavenumber 1, while the highest power in the Emanuel scheme is near 40 days and wavenumbers 1 and 2. The Hack scheme has a prominent secondary maximum near 60 days.

The McRAS scheme is the only scheme with notable eastward power at intraseasonal periods in the convective precipitation spectrum (Figure 3.8). This spectrum highlights a limitation of the simulation, however, in that power is lower than observed, although the intraseasonal variance of the Xie/Arkin precipitation product may be higher than that of other observed precipitation products (see Figure 3.10 and below). Note that the CCM3 contour interval is different than the contour interval in the observed precipitation spectrum. We compare convective precipitation generated by the model to total precipitation from observations because the convective parameterization accounts for almost all tropical precipitation in CCM3. One exception, as noted earlier, is that the Emanuel scheme tends to produce excessive large-scale precipitation in certain tropical areas. Including large-scale precipitation for the Emanuel scheme, however, does not alter the wavenumber-frequency spectrum. The Hack and Emanuel schemes produce reasonable eastward power in zonal winds, but no coherent spectral peaks in precipitation. Interestingly, both the ZM and McRAS schemes have heightened westward convective precipitation power at wavenumbers 3 and 4 at intraseasonal periods. These spatial and temporal scales are not present in observations. Regardless of this fact, the McRAS scheme is superior to the other three convective schemes in simulating eastward intraseasonal convective precipitation variance.

We now want to compare the distributions of tropical equatorial intraseasonal variance in observations to the CCM3 simulations. Intraseasonal variance plots of the equatorial 850 mb zonal wind as a function of longitude for observations (NCEP, December-May) and for the four CCM3 configurations are displayed in Figure 3.9. Winds at every longitude were filtered to 20-80 days and then averaged from 10°N to 10°S. Observed zonal wind variance is maximum over the western and central Pacific and Indian Oceans.

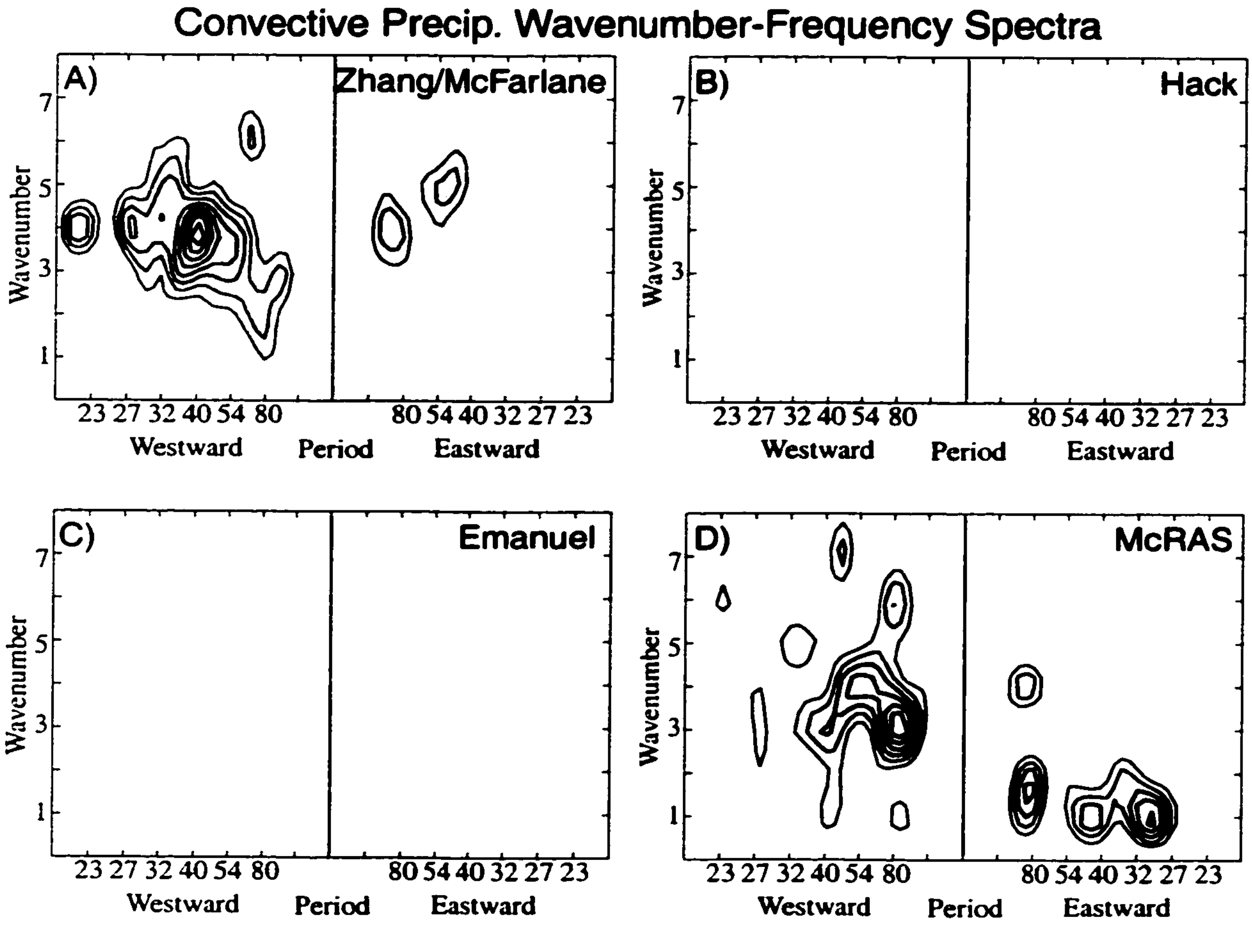

Figure 3.8. CCM3 precipitation spectra. Same as Fig3.6b, except for the perpetual March CCM3 simulations with the a) Zhang/McFarlane, b) Hack, c) Emanuel, and d) McRAS schemes, and with a contour interval of 0.5 mm^2 day^{-2} starting at 2.0 mm^2 day^{-2}. Values greater than 2.5 mm^2 day^{-2} are shaded.

The Hack and Emanuel schemes produce 850 mb zonal wind variances over the Indian and western Pacific Oceans that are far too high. The Hack scheme also shows excessive variances in other regions of the tropics. The ZM scheme produces reasonable zonal wind variance over the Indian Ocean, but very low variance over the western Pacific Ocean. Intraseasonal zonal wind variance is close to observed over both the Indian and western through central Pacific Oceans with the McRAS convection scheme.

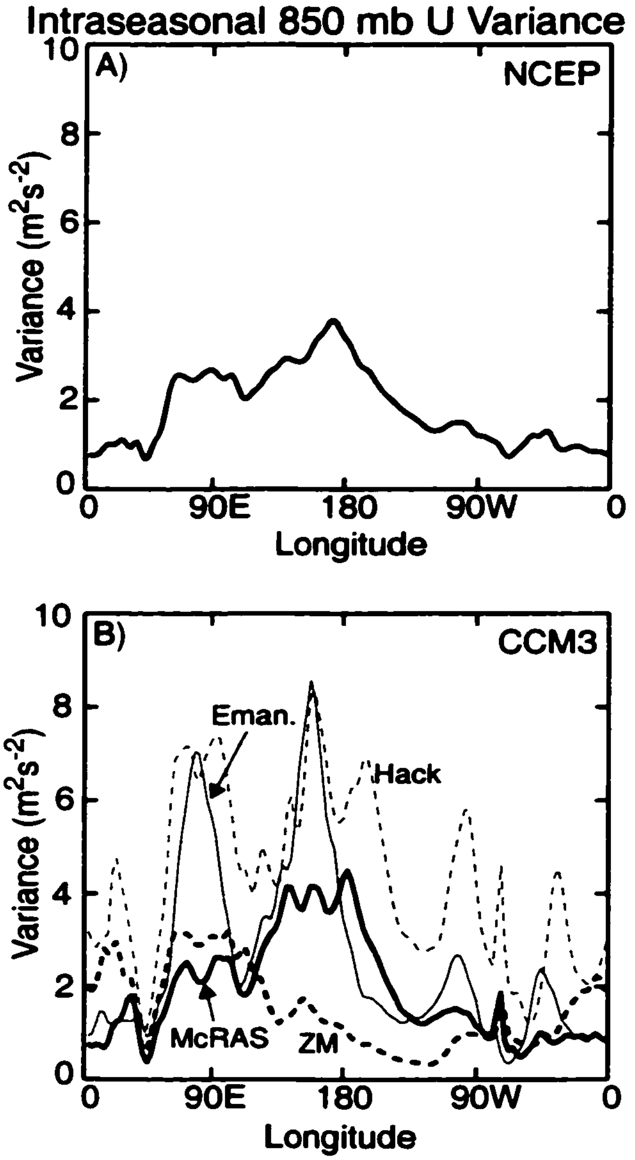

Figure 3.9. 10°N to 10°S averaged 20-80 day 850 mb zonal wind variance as a function of longitude for a) NCEP and b) CCM3 with Zhang/McFarlane (bold dashed), McRAS (bold solid), Hack (thin dashed), and Emanuel (thin solid).

Figure 3.10 shows a similar plot of intraseasonal convective precipitation variance. Note that the scales on the observation plot and CCM3 plot are different. Precipitation variance derived from the Microwave Sounding Unit (MSU, Spencer 1993) during 1979-

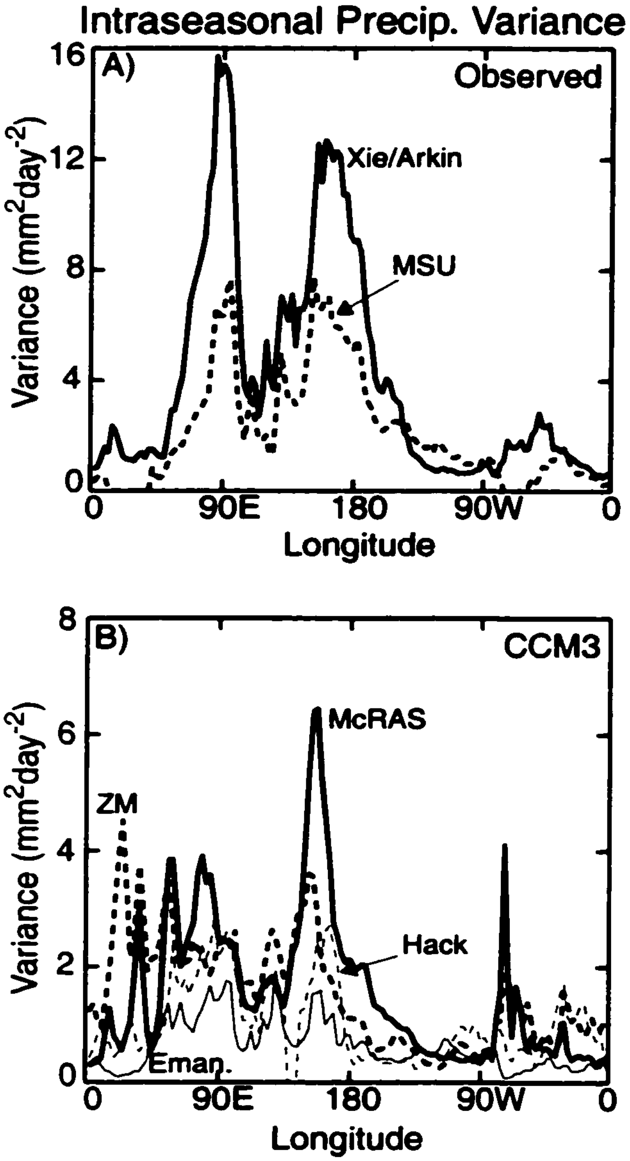

Figure 3.10. Precipitation variance. Same as Fig. 3.9, except for a) Xie/Arkin and MSU precipitation and b) CCM3 convective precipitation.

1994 is plotted along with the Xie/Arkin precipitation product. The MSU precipitation product indicates lower intraseasonal variability over the Indian and western Pacific Oceans than the Xie/Arkin product, and consequently the McRAS scheme precipitation variance agrees more closely with MSU precipitation than with Xie/Arkin. We however use the Xie/Arkin product in most of this paper because the MSU product is only valid over ocean areas, and therefore has significant gaps over the Maritime Continent, Africa, and South America. The differences between the two data products should be noted as a caveat when considering the results derived from Xie/Arkin precipitation.

All convective schemes produce intraseasonal precipitation variability that is lower than observed. However, the McRAS convection scheme produces significantly higher variability over the Indian and western Pacific Oceans than the other three convection schemes, particularly over the western Pacific. The lower than observed variability of precipitation with McRAS over the Indian Ocean is not surprising, since the simulated climatology of convection over that region is poor (Figure 3.2). The Hack scheme in general produces extremely variable convection (not shown), but little of it seems to be organized in intraseasonal timescales at low wavenumbers. The Hack scheme has much higher precipitation variability than the other schemes at high wavenumbers (not shown). With the Hack scheme convection tends to be very intense, short lived, spatially isolated, and without a preferred timescale for recurrence. The convection is not efficiently coupled with the large-scale circulation. These results suggest that intraseasonal equatorial wave disturbances in certain GCMs may be forced stochastically by convection, rather than by convective-dynamical coupling as seems to occur in nature.

In summary, the McRAS convective scheme shows superior performance at intraseasonal timescales to the ZM (default CCM3), Emanuel, and Hack schemes. The ZM scheme produces much lower than observed tropical intraseasonal variability in both 850 mb zonal winds and convective precipitation. The Hack and Emanuel schemes produce high variability in tropical 850 mb zonal winds, but no coherent intraseasonal precipitation signal. The McRAS scheme produces improvements in the simulation of both tropical winds and convective precipitation at intraseasonal timescales over the standard CCM3 ZM scheme. We will use the McRAS convection scheme in tests to determine which aspects of the scheme are important for improving the simulation of intraseasonal variability.

3.4) Composites

Before we conduct sensitivity tests using the CCM3 with McRAS, we should briefly examine the structure of model-generated intraseasonal oscillations to ensure that they are realistic. An 8-year perpetual March CCM3 simulation with McRAS was conducted. Data were saved in pentad (5-day mean) format. A composite MJO lifecycle was created following the method used in Chapter 2. Zonal winds at 850 mb were filtered to 20-80 day intraseasonal periods and then averaged from 7°N to 7°S at every longitude. Empirical orthogonal function (EOF) analysis on the zonal wind timeseries yields two significant EOFs (Figure 3.11). EOF1 explains 27% of the variance and EOF2 explains 18% of the variance. EOF1 and EOF2 are significantly different from the other EOFs based on the eigenvalue criterion of North et al. (1982). EOF1 resembles the second EOF in Figure 2.1 with a maximum amplitude over the western Pacific. EOF 2 is analogous to their first EOF with highest amplitudes over the Indian Ocean and central Pacific,

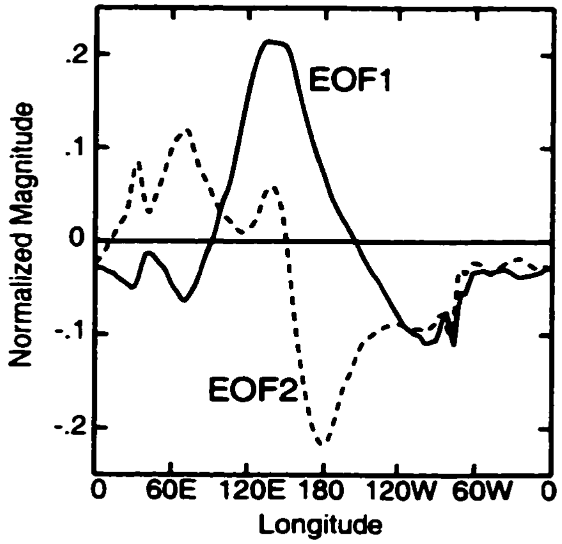

Figure 3.11. First two EOFs of the equatorially averaged (7°N-7°S) 20-80 day 850 mb zonal wind from the CCM3 with McRAS convection. Magnitudes are normalized.

although somewhat more noisy.

Principal components (PCs) are derived by projecting the first two EOFs onto the filtered data. A lag correlation analysis indicates that when PC1 lags PC2 by two pentads, the principal components are correlated at 0.4, and when PC1 leads -PC2 by two pentads, the principal components are correlated at 0.5. These correlations are somewhat lower than those between observed PCs, but are still significantly different from zero at the 95% confidence level. Thus, EOF 1 and EOF 2 describe an eastward propagating signal in the intraseasonal equatorial 850 mb zonal wind. For consistency with Chapter 2, we define an MJO index as follows, where t is the time in pentads:

$$Index(t) = PC2(t) + PC1(t+2) \tag{3.1}$$

To ensure that this index describes a coherent intraseasonal signal in unfiltered data, we project the first two EOFs onto the unfiltered equatorial timeseries, reconstruct the index, and then compute the power spectrum (Fig 3.12). Adjacent 64 pentad segments of the 8-year timeseries were used to compute the spectrum. Spectral peaks, significantly different from the red noise spectrum at the *a priori* 95% confidence level, are found at intraseasonal periods. Thus, the index represents a coherent signal, evident even in the unfiltered data.

Phases of the composite lifecycle were chosen as in Chapter 2, with positive deviations of the index greater than one standard deviation from zero defining significant events. As a result of this selection criterion, 33 events are isolated. Phase 5 is assigned to maximum peak amplitude in each event. Phases 1 and 9 are assigned to the troughs before and after the significant peak, respectively. Phases 3 and 7 are times where the index crosses zero. See Chapter 2 for more details.

Figure 3.13 shows tropical Pacific and Indian Ocean 850 mb wind and convective precipitation anomalies for phases 3,5,7, and 9 of the composite lifecycle. The panels in Figure 3.13 average two pentads apart. These composites are similar in many ways to composites derived from observations (Chapter 2). Convection first forms over the Indian

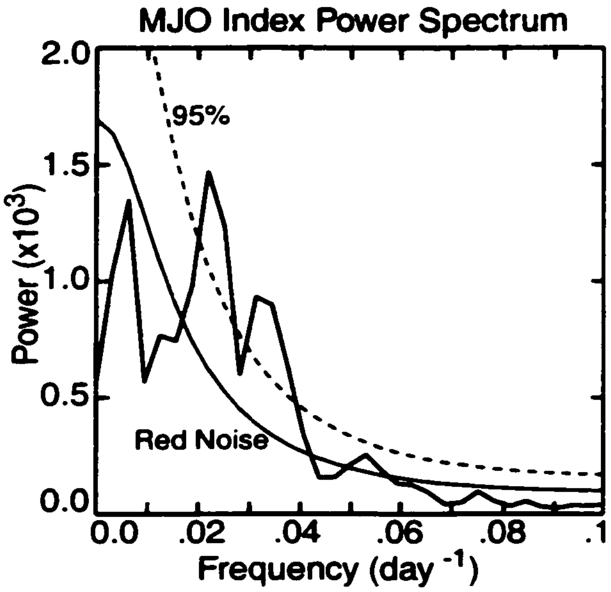

Figure 3.12. Power spectrum of the MJO index reconstructed by projecting the first two EOFs onto the unfiltered data. The red noise spectrum is displayed with the *a priori* 95% confidence limit.

Ocean (Phase 3) with easterly 850 mb anomalies extending over the western Pacific. Convection then shifts eastward into the western Pacific (Phase 5), where westerly anomalies ensue soon afterward (Phase 7). Suppressed convection is present over the western Pacific by Phase 9. Wind anomalies in the upper troposphere (not shown) are out of phase with those at 850 mb. Notable differences do exist between the observed and model composites. Convection tends to be less concentrated along the equator in the model than in observations, the model convection favors low-level anomalous easterly winds across the equatorial Pacific, and the simulation of Indian Ocean convection and winds is weaker than observed.

Figure 3.14 compares intraseasonal equatorial precipitation and 850 mb zonal wind anomalies as a function of phase during composite lifecycles for the CCM3 with McRAS and observations. Only observed events during December-May are included in the composite. Model convection tends to be shifted more toward the center of the 850 mb east-

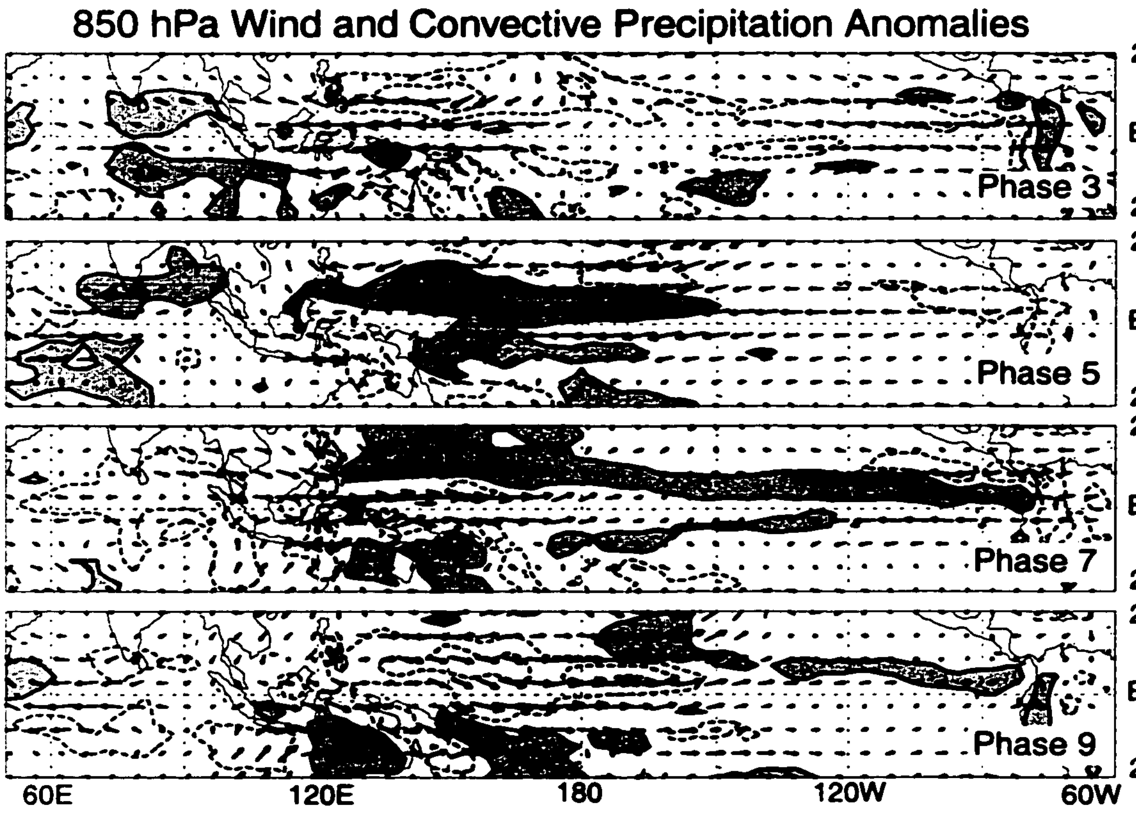

Figure 3.13. Intraseasonal 850 mb wind and convective precipitation anomalies for an MJO composite lifecycle in CCM3 with McRAS. Phases 3,5,7, and 9 are displayed. Contour interval is 1.2 mm day^{-1} starting at 0.6 mm day^{-1}. Negative contours are dashed. Maximum vectors are 3.6 m s^{-1}.

erly wind anomalies than in observations. This phase relationship may result from simulated intraseasonal convection being more highly correlated with surface convergence along the equator than is observed convection. Experiments were conducted using fixed surface wind speeds to calculate surface heat fluxes (not shown), and the phase relationship between convection and easterlies remained the same. The wind-induced surface heat exchange (WISHE) mechanism (Emanuel 1987, Neelin and Yu 1994) therefore cannot explain the preference for intraseasonal convection to form in anomalous easterly winds. Western Pacific model intraseasonal convection has a correlation of about 0.7 with

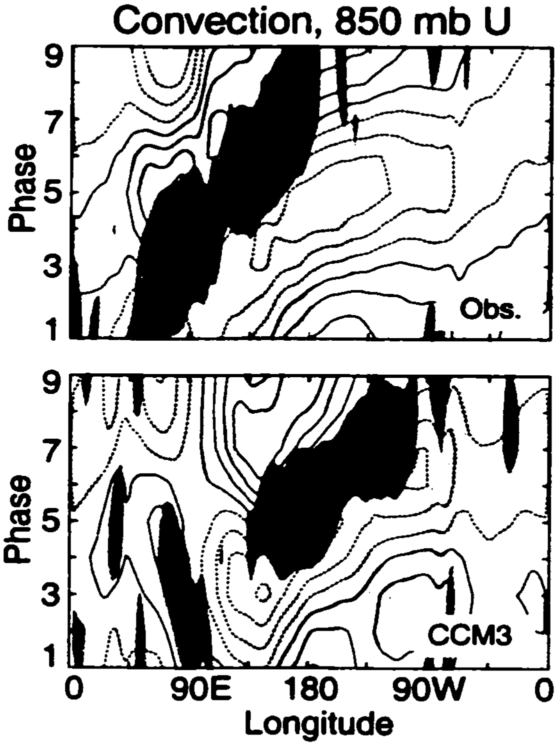

Figure 3.14. Equatorial 20-80 day 850 mb wind (contours) and precipitation (shading) anomalies as a function of MJO phase for a) observations (NCEP winds and Xie/Arkin precipitation, 5°N-5°S averaged) and b) CCM3 with McRAS (7°N to 7°S averaged). Contour interval is 0.50 m s^{-1} starting at 0.25 m s^{-1}. Easterlies are dashed. Dark shading represents precipitation anomalies greater than 0.3 mm day^{-1}. Light shading represents anomalies less than -0.3 mm day^{-1}.

surface convergence at zero lag, whereas observed convection is less highly correlated (about 0.4) with surface convergence, and convergence tends to lead intraseasonal convection slightly. Pacific intraseasonal precipitation anomalies in the model extend farther east than in observations.The simulation over the Indian Ocean is notably weaker than in observations with some indications of westward propagation across this region. Some of these differences may be caused by comparing a perpetual March simulation to observed composites derived during December-May. Further study is warranted to explore the differences between the model and observations. However, the simulation of the MJO in the

CCM3 with McRAS shows some broad similarities to observations.

Although the MJO equatorial convective envelope in the CCM3 generally moves eastward across the Pacific (Figure 3.14), westward propagating signals can be found in convection during enhanced periods of the MJO. An example of such westward propagation during an enhanced MJO period is shown in Figure 3.15. These westward-propagating convective signals are strongest off the equator, and are likely due to convectively coupled Rossby or mixed Rossby-gravity waves (e.g. Wheeler and Kiladis 1999). These waves may be strengthened during active MJO periods in the model, and heating associated with them may project strongly onto the model MJO, strengthening the equatorial

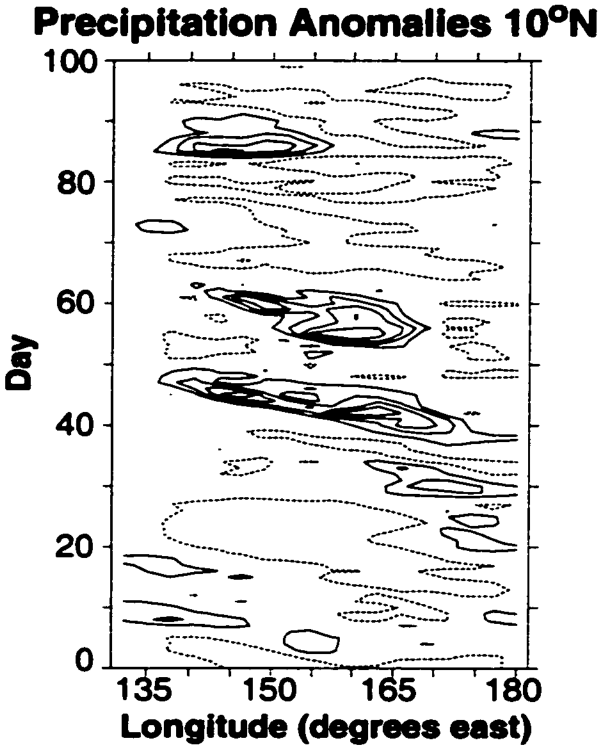

Figure 3.15. Time-longitude diagram of precipitation anomalies (long-term mean removed) at 10°N for a period with strong westward propagation. The contour interval is 12 mm day^{-1}, starting at 6 mm day^{-1}. Negative values are dashed.

circulation. Further study is needed, however, to explain their role in the model oscillation.

3.5) Sensitivity Tests

We will now assess the sensitivity of the MJO simulation in the CCM3 with McRAS to 1) relative humidity threshold (RH_c) and 2) to convective rain evaporation and unsaturated downdrafts. Four-year perpetual March simulations at standard model resolution were conducted for all the sensitivity tests. Wang and Schlesinger (1999, hereafter WS99) found intraseasonal variability in an 11-layer GCM to be sensitive to RH_c with a variety of convection schemes. We hypothesize that GCM performance on MJO timescales is sensitive to the parameterization of rain evaporation and subsequent downdrafts in unsaturated regions near convection. Although the Emanuel convection scheme also includes a parameterization of unsaturated downdrafts, issues such as excessive large-scale tropical precipitation and the dependence of model performance on vertical resolution (see Section 3b) need to be addressed before the sensitivity of GCM performance to unsaturated downdrafts with the Emanuel scheme can be examined. The Emanuel scheme also does not account for cooling and moistening by lighter convective rainfall away from downdraft areas, as does the McRAS scheme. We note, however, that every convective scheme interacts with its environment differently. Implementing the rain evaporation and downdraft scheme of McRAS into a different convective parameterization may not produce similar behavior.

3.5.1) Relative humidity threshold

Bladé and Hartmann (1993) and Hu and Randall (1994) suggested that MJO convective events stabilize the atmosphere and that time for atmospheric preconditioning is needed before significant convective events can recur. WS99 hypothesized that a boundary layer RH_c for initiation of deep convection is consistent with the idea of preconditioning. They found that imposing an RH_c in the UIUC 11-layer GCM significantly improves

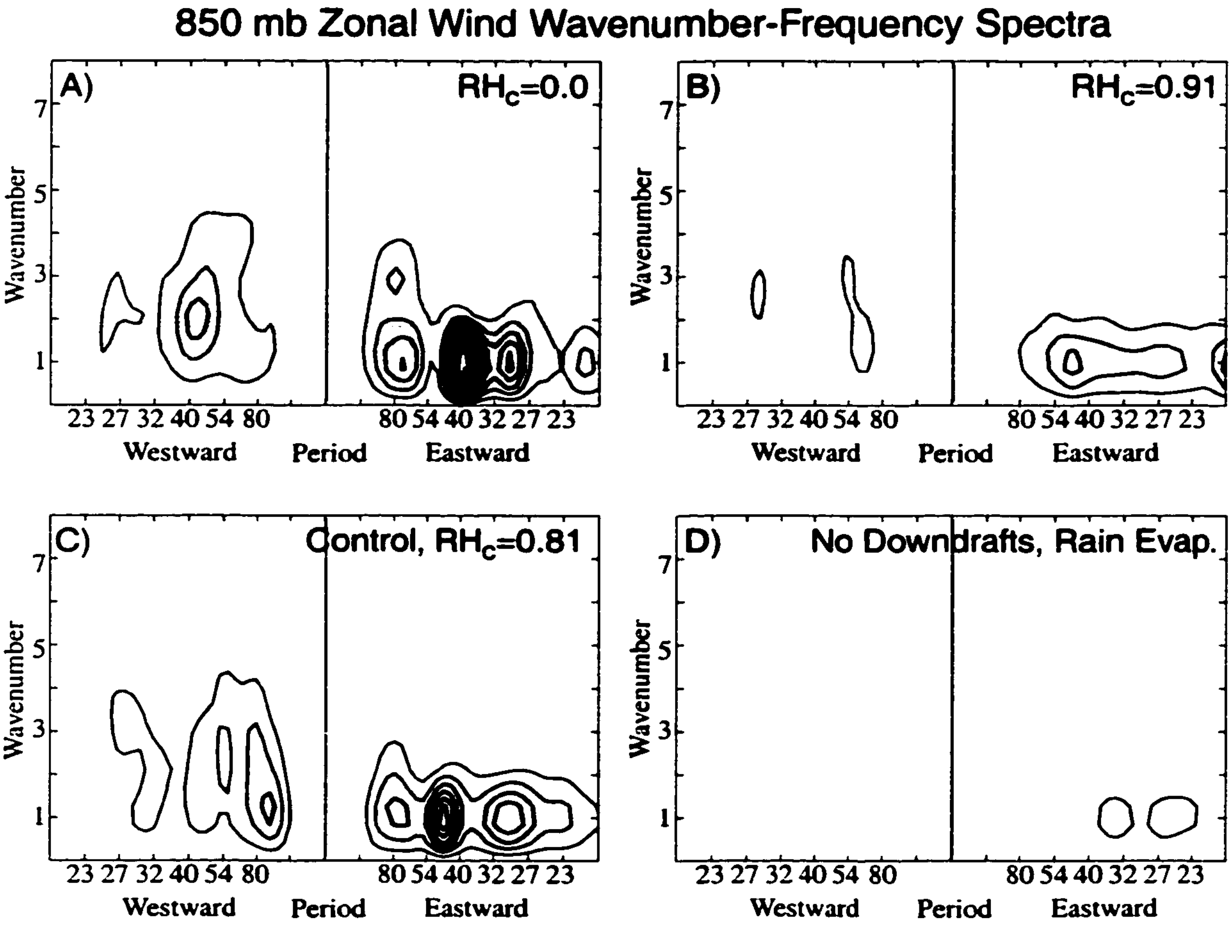

Figure 3.16. McRAS sensitivity spectra. Same as Fig. 3.6a, except for CCM3 McRAS simulations with a) RH_c=0.0, b) RH_c=0.91, c) RH_c=0.81 (control), and d) no unsaturated downdrafts or convective precipitation evaporation, and with a contour interval is 3.5 m^2s^{-2} starting at 3.5 m^2s^{-2}. Values greater than 7.0 m^2s^{-2} are shaded.

intraseasonal variability with certain convection schemes. Higher thresholds produced the most realistic intraseasonal oscillations.

The McRAS control run has an RH_c of 0.81 for initiation of convection. Cloud base is designated as the lowest level between 700 mb and 960 mb satisfying this threshold. None of the other convection schemes we use with CCM3 have such a threshold. We compare the McRAS base run to simulations having RH_c of 0.0 and 0.91. Tropical mean relative humidities in the lower and middle troposphere in the western Pacific and Indian Oceans generally do not vary by more than 2% among these experiments.

Figure 3.16 includes equatorial 850 mb zonal wind wavenumber-frequency spectra for RH_c=0.91, RHc=0.81 (the control run), and RH_c =0.0. Note that the contour interval is slightly different than that in Figure 3.7. Eastward power at intraseasonal periods is diminished for the higher RH_c of 0.91, a somewhat surprising result, in view of the findings of WS99. The highest power at eastward periods and intraseasonal timescales occurs for a RH_c of 0.0. No significant differences in the dominant frequency or wavenumber can be discerned among the runs, and the exact location of spectral peaks may change slightly for two different simulations with the same RH_c. The dominant periods are more robust for simulations in which the WISHE mechanism is removed (not shown), suggesting that differential surface evaporation may influence the run-to-run consistency of the dominant periods. The deterioration of the eastward intraseasonal signal with higher RH_c is confirmed by an equatorial lag regression analysis of 850 mb zonal wind (not shown).

Figure 3.17 compares the equatorial intraseasonal 850 mb zonal wind variance as a function of longitude for the three relative humidity experiments. The highest intraseasonal variance in 850 mb zonal wind occurs with the RH_c=0.0 simulation. The locations of the maximum variance coincide with those of the McRAS control simulation. Intraseasonal variability decreases slightly with the higher RH_c of 0.91, particularly over the central Pacific. Intraseasonal precipitation variances show analogous differences among the relative humidity experiments (not shown).

These results differ from those of WS99. In some of their experiments, they use a RAS scheme that implements a relative humidity threshold at the top of the boundary layer for initiation of convection. Increasing values of RH_c produce stronger intraseasonal variability in winds and convection. As mentioned above, RH_c is used somewhat differently in the McRAS scheme than in WS99. However, we can say with confidence that this threshold is not the reason for the improved intraseasonal variability in the CCM3 with McRAS. The interactions between convection and boundary layer relative humidity are

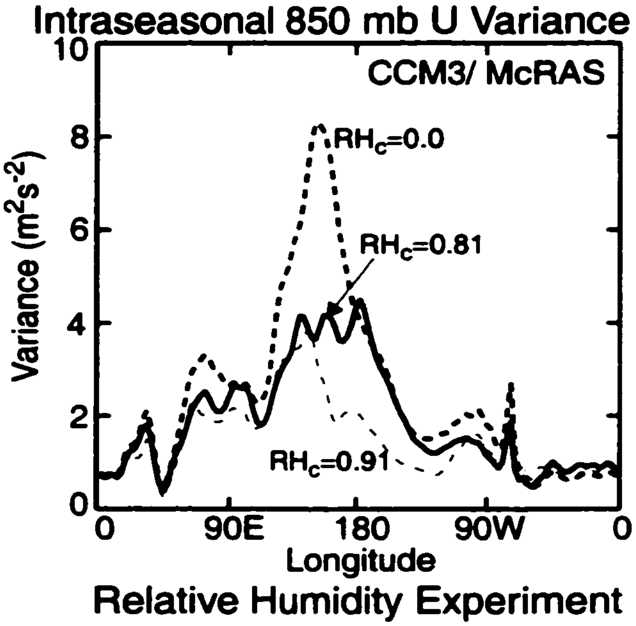

Figure 3.17. Relative humidity experiment variance. Same as Fig. 3.9b except for CCM3 McRAS simulations with RH_c=0.0 (bold dashed), RH_c=0.81 (control, bold solid), and RH_c=0.91 (thin dot-dash).

likely different in McRAS than in the convection schemes of WS99. A high RH_c in McRAS may stifle intraseasonal variability by making convection too sporadic, preventing realistic moisture processes in the McRAS scheme (such as the rain evaporation and downdraft scheme) from properly functioning.

3.5.2) Evaporation of convective precipitation and unsaturated downdrafts

Evaporation of convective precipitation by the McRAS scheme in unsaturated environmental air drives unsaturated downdrafts in the convective core, and moistens and cools the atmosphere in regions of lighter precipitation outside of the convective core (such as below the anvil). The Zhang and McFarlane scheme has saturated downdrafts, but downdrafts are caused by convective evaporation within the cloud. Therefore, evaporation only contributes toward keeping the in-cloud downdrafts in a saturated state during descent. The effects of these downdrafts are small. As mentioned above, the Emanuel scheme does have unsaturated downdrafts, but it does not account for the evaporation of convective precipitation outside of downdraft regions. The Hack scheme has no downdraft parameterization.

Figure 3.16d shows a wavenumber-frequency spectrum for a CCM3 McRAS simulation in which the tendencies associated with convective downdrafts and rain evaporation are set to zero. We will call this simulation the "no-downdraft" simulation. Eastward power at intraseasonal timescales and wavenumber 1 is strongly reduced over the control simulation. An 850 mb zonal wind lag regression analysis (not shown) indicates that eastward propagation appears to be more rapid than in the control run, and the amplitude of the signal is strongly reduced. This observation is reinforced by Figure 3.18, which plots intraseasonal equatorial 850 mb zonal wind variance as a function of longitude. Zonal

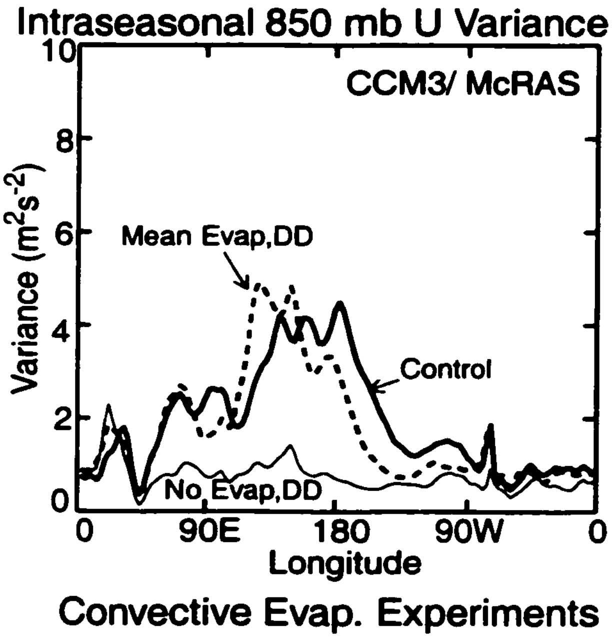

Figure 3.18. Downdraft experiment variance. Same as Fig. 3.9b except for CCM3 McRAS simulations with RH_c=0.81 (control, bold solid), no convective evaporation, downdrafts (thin solid), and time-invariant (mean) convective evaporation, downdrafts (bold dashed).

wind variance dramatically decreases without convective evaporation with few prominent features at any longitude along the equatorial belt. Similar trends are found in precipitation variance (not shown). When comparing the precipitation climatologies of the simulations (not shown), the simulation without downdrafts and rain evaporation tends to have slightly stronger mean ITCZ structures over the central and eastern Pacific and slightly stronger mean convection over the northern Indian Ocean. Equatorial precipitation is greater when downdrafts are included. Rain evaporation and downdrafts considerably moisten the lower and middle troposphere in the mean (see below). In addition to moistening by the direct effects of rainfall evaporation, downdrafts can lead to less compensating subsidence away from convection, promoting a moister lower and middle troposphere (Johnson 1976).

Evaporation of convective precipitation in downdrafts and in the larger environment appears to be crucial in simulating realistic intraseasonal oscillations with the McRAS scheme. A serious degradation of the simulation of intraseasonal variability occurs when convective evaporation is not accounted for in the model. The improvement in tropical intraseasonal variability supplements the documented beneficial effects that including unsaturated downdrafts in convection schemes have on the mean temperature and moisture profiles of the tropical atmosphere (e.g. Sud and Walker 1993).

Figure 3.19 shows the contributions to the specific humidity and temperature tendencies by convective rain evaporation processes at the equator and 160°E during several phases of the CCM3 with McRAS MJO composite lifecycle described in Section 4. The contributions due to both unsaturated downdrafts in convective cores and convective precipitation evaporation in lighter precipitation areas are included. All of the drying due to unsaturated downdrafts occurs at the lowest model layer with a notable peak in moistening near 900 mb, where boundary layer air has been displaced upwards. Moistening at the 900 mb level is 34% higher at phase 5 than phase 9. Rain evaporation moistening occurs into the upper troposphere. The maximum cooling occurs at the lowest model layer with lesser cooling aloft. Boundary layer diffusion will act to mix the lowest level tendencies throughout the boundary layer (see below). Since the downdraft tendency variations in our simulation are considerably smaller than the mean tendencies, time-mean downdraft effects may be important for improving model intraseasonal variability. We will examine this hypothesis in the next section. Variations of downdraft tendencies with phase may, however, contribute to MJO variability. Downdrafts may help stabilize the atmosphere after a strong convective event by bringing low moist entropy air into the boundary layer. The atmosphere must be sufficiently destabilized before strong convection can again occur. Evaporation of convective precipitation into the environment may be a factor in preconditioning the atmosphere for strong MJO convective events. Moist boundary layer air displaced upward when unsaturated downdrafts reach the surface can contribute to atmospheric moistening. Sud and Walker (1999b) compared MJO simulations in the Goddard Earth Observing System II (GEOS II) GCM with and with without McRAS and found that MJO variability was similar in both models. The GEOS II GCM does however have a parameterization of evaporation of falling convective precipitation (Sud and Molod 1988) in use with a RAS convective scheme.

3.5.3) Time-invariant downdraft experiment

Figure 3.19 indicates that variations in moisture and temperature tendencies due to downdrafts and rain evaporation in the CCM3 with McRAS are smaller than the mean values. Slingo et al. (1996) suggested that the GCMs with the most realistic mean climates produce the most realistic intraseasonal oscillations. We will now determine whether the mean effects of convective evaporation and downdrafts, and not their variability, are most important for producing realistic tropical intraseasonal oscillations in the CCM3 with McRAS.

A four-year, perpetual March simulation was conducted with the convective rain evaporation and unsaturated downdraft schemes removed. Time-invariant rain evaporation and downdraft tendencies were imposed at each convective time step, however. The imposed temperature and moisture sources are the climatological rain evaporation and downdraft tendencies derived from a McRAS simulation with convective evaporation included. For example, the climatological temperature and moisture tendencies at 160°E,

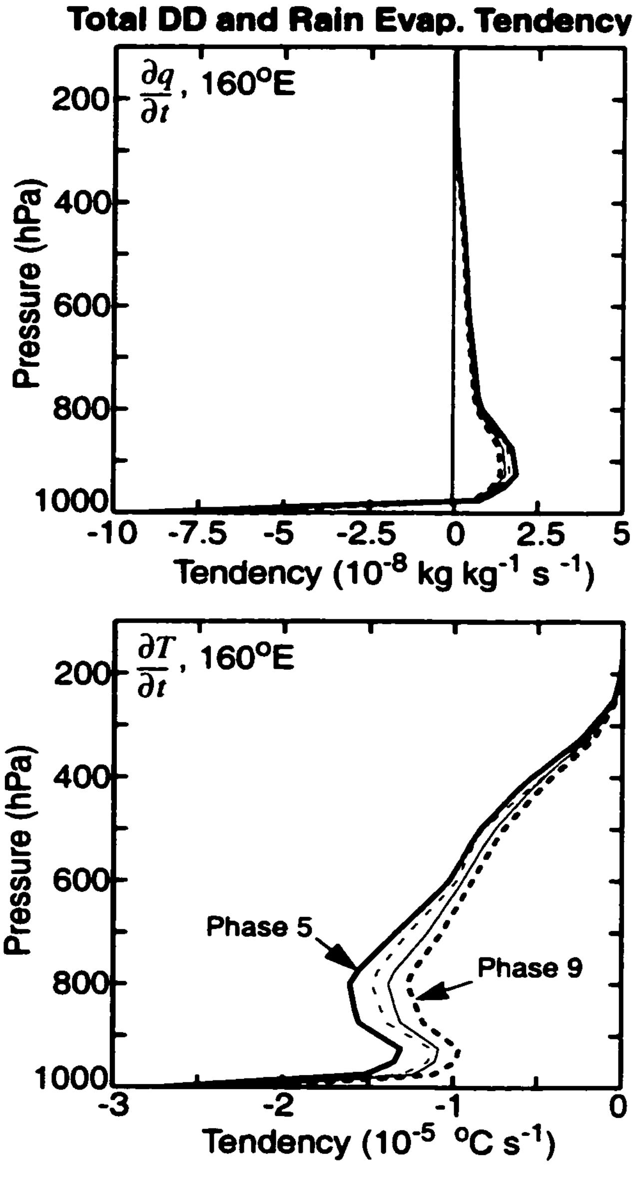

Figure 3.19. Specific humidity and temperature tendencies due to the evaporation of convective precipitation, including unsaturated downdrafts, for phase 3 (thin, dot-dash), phase 5 (thick, solid), phase 7 (thin, solid), and phase 9 (thick, dotted) of an MJO lifecycle in CCM3 with McRAS.

0°N would lie between phase 5 and phase 9 in Figure 3.19. The tendencies at other grid cells show similar structure, but vary in amplitude with the strength of mean convection. We will call this simulation the "mean-downdraft" simulation.

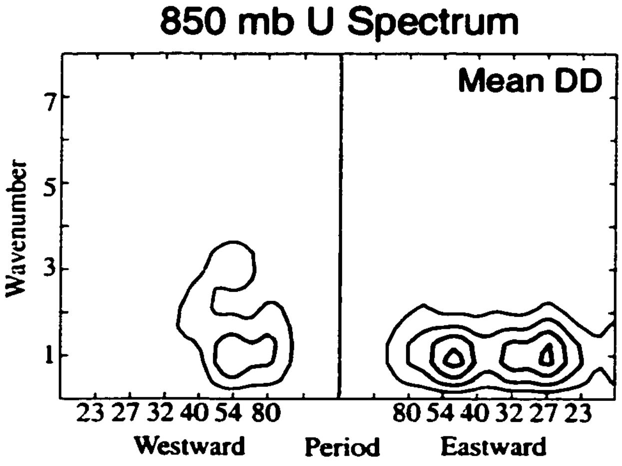

Figure 3.20. Mean downdraft simulation spectrum. Same as Fig. 3.16, except for a CCM3 McRAS simulation with time-invariant (mean) convective evaporation, downdrafts.

Figure 3.20 displays a wavenumber-frequency spectrum for the mean-downdraft simulation. Intraseasonal variance at eastward wavenumbers is increased considerably over the no-downdraft simulation (Figure 3.16d), and power approaches that of the McRAS control simulation. The distributions of 850 mb intraseasonal zonal wind variance as a function of longitude for the mean-downdraft and McRAS base runs are also similar (Figure 3.18). These results provide evidence that the mean effects of convective evaporation processes, and not their variations, are responsible for the large difference in intraseasonal variability between the McRAS control simulation and the no-downdraft simulation.

We will now diagnose model climate changes that accompany the improvement in intraseasonal variability due to time-mean rain evaporation and downdraft tendencies. Temperature and humidity climatologies from the McRAS base run and the mean-down-

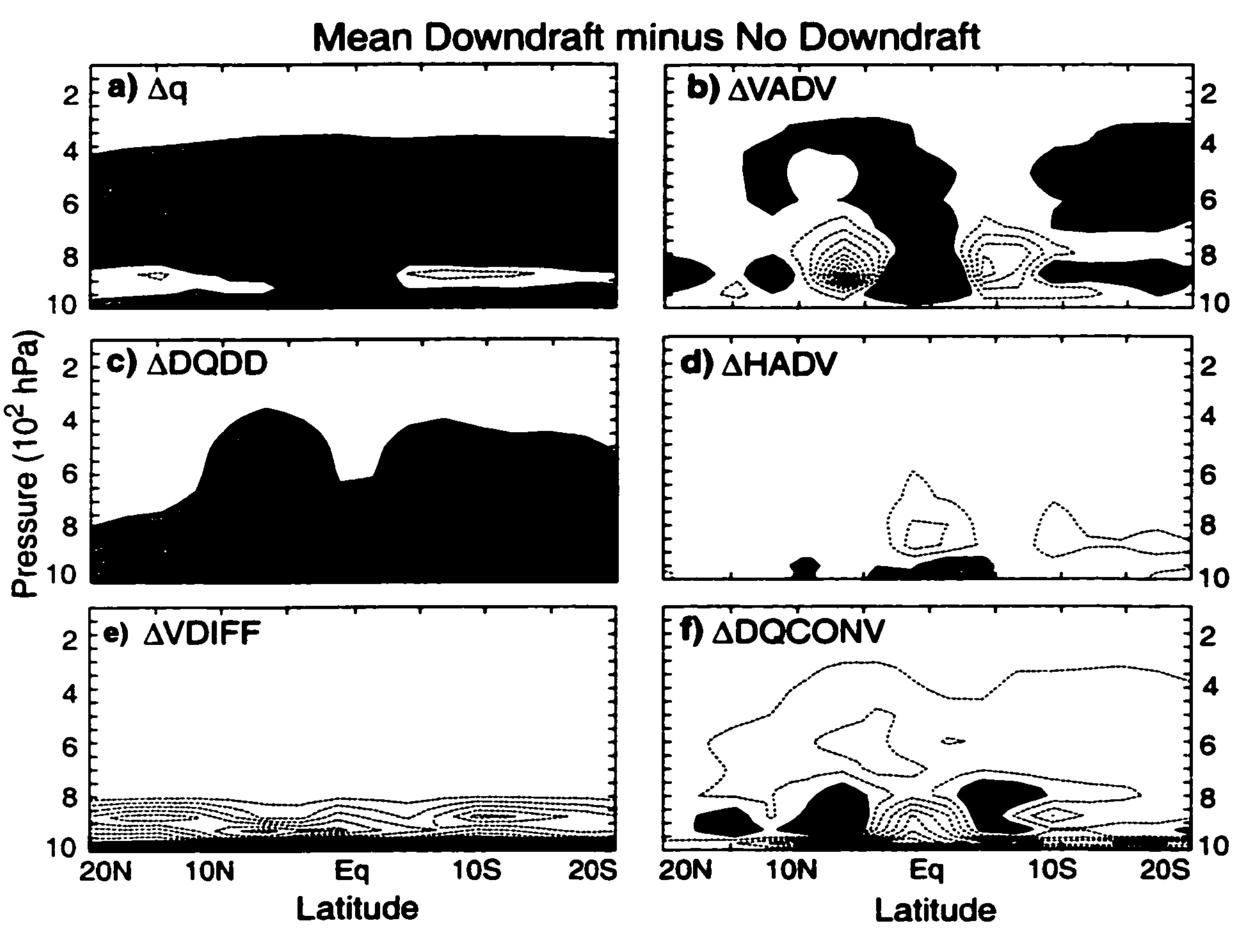

Figure 3.21. Zonally averaged (150°E-110°W) differences in a) specific humidity, and specific humidity tendencies due to b) vertical advection, c) unsaturated downdrafts and rain evaporation, d) horizontal advection, e) boundary layer vertical diffusion, and f) convective updraft moistening or drying (McRAS mean-downdraft simulation minus McRAS no-downdraft simulation). Contour interval in a) is 0.6 g kg^{-1}, starting at 0.3 g kg^{-1}. Values greater than 0.3 g kg^{-1} are shaded. Contour interval in b)- f) is 0.3 g kg^{-1} day^{-1}, starting at 0.15 g kg^{-1} day^{-1}. Values greater than 0.15 g kg^{-1} day^{-1} are shaded. Contours less than zero are dashed.

draft simulation are almost indistinguishable (not shown). Figure 3.21a compares Pacific mean specific humidity as a function of latitude (150°E-110°W averaged) between the mean-downdraft and no-downdraft simulations. The longitudes selected for the average include those containing significant Pacific MJO convective activity (Figure 3.14). No land points fall within 20° of the equator at these longitudes. Downdrafts and rain evaporation considerably moisten the troposphere, especially near the equator. The largest equatorial Pacific moisture increases in the mean-downdraft simulation occur near the 800 mb level. A hint of drying occurs near 900 mb off the equator.

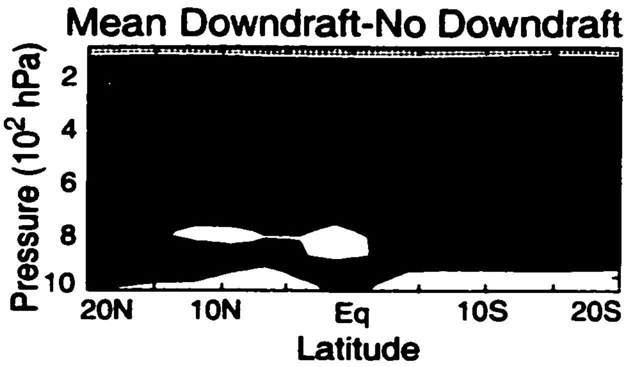

Figure 3.22. Mean downdraft minus no downdraft temperatures. Same as Fig. 3.21a, except for temperature differences. Contour interval in a) is 0.6 °K, starting at 0.3 °K. Values greater than 0.3 °K are shaded.

Figure 3.21 also shows the change in specific humidity tendency between the mean-downdraft and no-downdraft simulations due to vertical advection (19b), mean downdrafts and convective rain evaporation (19c), horizontal advection (19d), boundary layer diffusion (19e), and convective adjustment (19f). Changes in the specific humidity tendency terms conspire to produce a moister equatorial troposphere in the mean-downdraft simulation. Increased vertical advection on the equator fosters a moister equatorial troposphere, and increased horizontal advection contributes to moistening at the lowest levels. Increased convective drying partially balances this moistening due to advection. The prescribed convective evaporation processes directly moisten all levels above the surface layer, although boundary layer diffusion drys the boundary layer by redistributing the dry surface air generated by the downdraft scheme. Seager and Zebiak (1995) noted that downdrafts in their model tend to inject low θ_e air into the boundary layer, leading to convection being favored over the warmest SSTs. This may contribute to equatorial convection being favored in our McRAS simulation with downdrafts (see below). The mean-downdraft simulation also produces a warmer troposphere than the no-downdraft simulation, especially at upper levels (Figure 3.22).

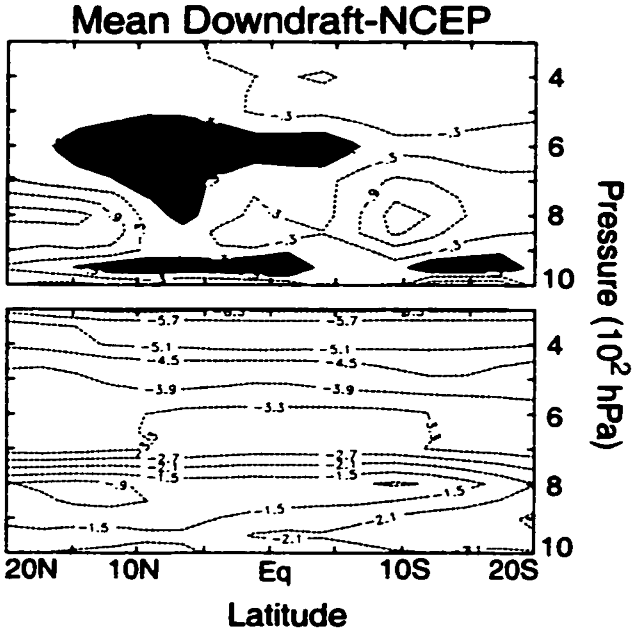

Figure 3.23. Zonally averaged (150°E-110°W) differences in a) specific humidity and b) temperature (McRAS mean-downdraft simulation minus March NCEP climatology). Contour interval in a) is 0.6 g kg^{-1}, starting at 0.3 g kg^{-1}. Values greater than 0.3 g kg^{-1} are shaded. Contour interval in b) is 0.6°K, starting at 0.3°K. Contours less than zero are dashed.

Figures 3.21a, 3.22, and 3.23 show that the mean-downdraft simulation produces tropospheric temperature and moisture values closer to March observed values (NCEP reanalysis) than the no-downdraft case. A realistic mean climate is more likely to produce realistic intraseasonal variability. The no-downdraft simulation is severely dry across the tropics compared to observations, especially at the equator. One caveat in this comparison is that the NCEP specific humidity analyses may contain large uncertainties in the tropics (Trenberth and Guillemot 1995). Although closer to observations, the mean-downdraft simulation does show a considerable cold bias of up to 6°C in the upper troposphere. Temperature biases may be reduced with a radiation parameterization that explicitly interacts with the cloud microphysics.

Mean equatorial Pacific precipitation is 4 mm day^{-1} greater in the mean-downdraft case than in the no-downdraft case (Figure 3.24), a two- to three-fold increase. Mean equatorial precipitation for the McRAS control simulation (not shown) is also higher (2 mm day^{-1}) than the no-downdraft case. Increased equatorial convection may be important for intraseasonal variability, since Salby and Hendon (1994) observed that the MJO signal is greatest when climatological convection is near the equator. Observed mean western Pacific precipitation is high along the equator during March (Figure 3.2), a month of significant MJO activity.

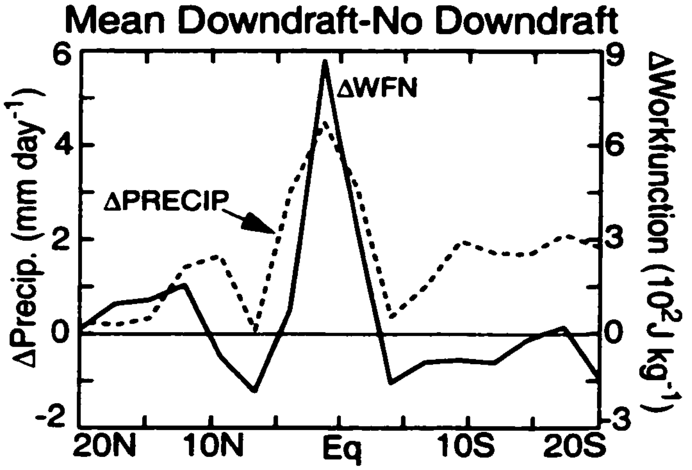

Figure 3.24. Zonally averaged (150°E-110°W) differences in precipitation and upper tropospheric cloud work function (McRAS mean-downdraft simulation minus McRAS no-downdraft simulation).

The degree of convective adjustment in McRAS is determined by the cloud work function, a measure of the total buoyancy of lower-tropospheric parcels for moist convective ascent (see Moorthi and Suarez 1992, Appendix B). The difference in cloud work function for clouds detraining at model level 6 (near 150 mb) between the mean-downdraft and no-downdraft simulations is shown in Figure 3.24. Convection is assumed to originate in level 17 (one level above the surface), the level at which McRAS tropical convection originates the vast majority of the time. The equatorial cloud work function is over 800 J kg^{-1} higher in the mean-downdraft simulation, almost doubling the mean equatorial work function of the no-downdraft case. The increase in equatorial cloud work function is predominately due to the moister equatorial boundary layer in the mean-downdraft simulation. Although tropospheric temperatures are generally higher, the temperature increases are overwhelmed by the moisture signal on the equator, leading to a greatly increased cloud work function. Similar results are obtained for clouds detraining at other model levels. In practice, one cloud type will affect the environmental conditions felt by other cloud types during the adjustment process. Our calculations give a general indication, however, of the likelihood of tropical deep convection.

Increased equatorial convection in GCMs may not be a sufficient condition for improved intraseasonal variability, however, since both the Hack and Emanuel schemes produce significant equatorial convection, but unrealistic intraseasonal variability. The McRAS scheme also produces mean Pacific equatorial convection that is only slightly higher than that produced by the Zhang/McFarlane scheme. We therefore cannot generalize to all convection schemes the importance of equatorial convection in producing realistic intraseasonal variability. Our results do indicate, however, that equatorial convection may be important for intraseasonal variability with the McRAS scheme.

In summary, the McRAS simulations with parameterized convective rain evaporation and unsaturated downdrafts produce an improved climate over a McRAS simulation where these processes are neglected. The simulation without downdrafts produces a troposphere that is excessively dry, especially at the equator. The excessively dry equatorial atmosphere reduces the mean cloud work function, a measure of buoyancy that regulates convection in McRAS. The cloud work function is most sensitive to moisture variations in the boundary layer. Increased equatorial convection associated with a more realistic climate may foster improved intraseasonal variability.

3.6) Conclusions

The NCAR CCM3.6 with the RAS convection scheme of Moorthi and Suarez (1992), modified by Sud and Walker (1999a, McRAS), exhibits superior performance in the tropics at intraseasonal timescales, compared to simulations with the convection schemes of Zhang and McFarlane (1995) (the CCM3 default deep convection scheme), Hack (1994), and Emanuel (Emanuel and Zivkovic-Rothman 1999). The standard CCM3 with the Zhang and McFarlane convection scheme produces only weak equatorial intraseasonal zonal wind signals at eastward periods and very little variability in convection. The McRAS scheme produces a much improved simulation in intraseasonal zonal wind variability with realistic eastward phase speeds. Precipitation variability is also much improved, particularly over the western Pacific warm pool regions. Deficiencies remain over the Indian Ocean. MJO convection also tends to be more closely aligned with easterly wind anomalies, indicating a stronger relationship between convection and surface convergence than in the observations. The Hack and Emanuel schemes tend to produce high amplitude eastward propagating signals in intraseasonal equatorial zonal winds with realistic propagation speeds, but little coherent intraseasonal variability in convective precipitation. The atmospheric circulation and convection do not seem to be very well coupled. The intraseasonal wind signals may be due to stochastic forcing by convection. Performance of the convection schemes as implemented in the T42L18 CCM3 may not be indicative of their performance in higher resolution models.

Sensitivity tests suggest that convective precipitation evaporation processes are important to the success of the McRAS scheme in simulating the MJO. Removal of the evaporation of convective precipitation in unsaturated downdraft regions and in the larger environment greatly reduces the amplitude of intraseasonal oscillations in the CCM3. The time-mean effects of downdrafts and rain evaporation, and not their variations, may be most important for improving intraseasonal variability. Including a parameterization of convective evaporation effects lead to more realistic specific humidity and temperature climatologies, and increases equatorial convection. The mean equatorial cloud work function for convective plumes detraining at upper levels is increased due to a moister lower troposphere. Our results suggest that a realistic simulation of specific humidity is crucial for correctly simulating the Madden-Julian oscillation.

Imposing a relative humidity threshold does not improve the success of the McRAS scheme in simulating intraseasonal variability. In fact, removal of the threshold somewhat increases intraseasonal variability. These results suggest that the interaction between convection and lower tropospheric humidity are different in CCM3 with McRAS than in the model simulations of Wang and Schlesinger (1999), where intraseasonal variability in their atmospheric GCM strengthens with increasing relative humidity threshold for a variety of convective parameterizations. Our work and that of Wang and Schlesinger (1999) are consistent in that they point to the importance of lower tropospheric moisture processes for tropical intraseasonal variability.

A relative humidity threshold and a thorough treatment of convective precipitation evaporation with unsaturated downdrafts are two major differences between the McRAS scheme and the other convective schemes we use in this study. The Emanuel scheme contains unsaturated downdrafts, but does not account for the evaporation of convective precipitation in lightly precipitating areas away from downdrafts. We do not claim that implementing the McRAS parameterization of downdrafts and rain evaporation in the other convective schemes will necessarily improve intraseasonal variability, since every scheme interacts with its environment differently. Our results indicate, however, that a proper simulation of lower tropospheric water vapor may be crucial in producing realistic GCM intraseasonal variability. More analysis needs to be done on the McRAS simulations to understand the feedbacks between lower troposphere water vapor and atmospheric convection during an MJO lifecycle.

4) Frictional Convergence in the CCM3 with McRAS

4.1) Introduction

Previous studies have suggested the importance of frictional convergence during a Madden-Julian oscillation (MJO) lifecycle (e.g. Wang and Rui 1990, Hendon and Salby 1994). Hendon and Salby (1994) found that amplifying MJO convective anomalies are supported by surface convergence. Maximum convergence at the surface leads convergence at 850 mb, and leads peak positive convective anomalies (Jones and Weare 1996). Surface convergence during an MJO lifecycle may be enhanced through interactions with sea surface temperatures and the oceanic mixed layer (Waliser et al. 1999). The inclusion of surface friction improves upon MJO theories espousing wave-CISK (conditional instability of the second kind) by explaining the selection of unstable, planetary-scale modes (Wang and Rui 1990).

Other work has indicated the importance of atmospheric preconditioning to the MJO (Bladé and Hartmann 1993, Hu and Randall 1994). After the atmosphere has been stabilized by a strong MJO convective event through latent heating and lower tropospheric drying and cooling from downdrafts, the atmosphere must be preconditioned before strong MJO convection can again occur. Moistening of lower levels and radiative cooling aloft may be particularly important for atmospheric preconditioning (Hu and Randall 1994). Raymond and Torres (1998) hypothesized that convection of low precipitation efficiency and surface fluxes are important for moistening the middle and lower troposphere during an MJO lifecycle.

Frictional convergence can also contribute to lower-tropospheric moistening. Maloney and Hartmann (1998) found that lower-tropospheric precipitable water and 1000-mb convergence are significantly correlated during an MJO lifecycle. Wang and Schlesinger (1999) concluded, using the University of Illinois Urbana-Champaign (UIUC) general circulation model (GCM) with several convective parameterizations, that frictional moisture convergence and lower-tropospheric moistening may be important for simulating realistic intraseasonal variability. They found that a relative humidity threshold for initiation of convection improved model intraseasonal variability in their GCM, although Maloney and Hartmann (2000c, hereafter MH00, Chapter 3) found that a relative humidity threshold may not improve the performance of all models.

MH00 (Chapter 3) examined MJO variability in the National Center for Atmospheric Research (NCAR) Community Climate Model 3 (CCM3, Kiehl et al., 1998) using several deep convection schemes. MH00 found that the microphysics of clouds with relaxed Arakawa-Schubert (McRAS, Sud and Walker 1999a) convection scheme produced the most realistic MJO variability of the four convective schemes used. Intraseasonal zonal wind variability with McRAS is close to observed, and McRAS tropical intraseasonal precipitation variability is more realistic than that of the other convection schemes. The parameterization of convective rain evaporation in unsaturated air and unsaturated downdrafts is important for producing realistic intraseasonal variability in McRAS (MH00). Intraseasonal variability in McRAS varies inversely with relative humidity threshold, contrary to the findings of Wang and Schlesinger (1999).

McRAS intraseasonal oscillations differ from those observed, however, in that positive convective anomalies tend to occur in association with lower tropospheric easterly wind anomalies. Hendon (2000) found a similar phase relationship in a GCM simulation with strong intraseasonal variability. Observed MJO convective anomalies tend to occur closer to the nodal points in 850 mb zonal wind anomalies, and may even extend westward into regions of surface westerlies (Hendon and Salby 1994).

This chapter will examine the importance of surface convergence and low-level specific humidity to the MJO, as simulated by the CCM3 with McRAS. The phase relationship between model anomalous MJO convection and lower tropospheric easterly wind anomalies will also be examined. Model results will be compared to those from observations. Analysis will show that moistening of the lower troposphere by frictional convergence is important for maintaining the model MJO. This mechanism was also found to be important during an observed MJO lifecycle (Maloney and Hartmann 1998, Chapter 2). The last section will discuss whether the wind-induced surface heat exchange (WISHE) mechanism of Emanuel (1987) and Neelin and Yu (1994) is important for supporting intraseasonal variability.

4.2) Data and Model Simulations

Xie/Arkin precipitation and NCEP wind reanalyses during 1979-1997 are used as observations, and described in section 3.3.1. An 8-year perpetual March simulation of the CCM3 with McRAS convection is used in this chapter. This simulation is identical to the 8-year McRAS control simulation used in MH00 (Chapter 3). An alternate 8-year run was generated to examine surface latent heat flux anomalies. Climatological March sea surface temperatures (Figure 3.1) and March 15 insolation are used as boundary conditions. A third simulation was also conducted, as described in section 4 below, that documents the effects of removing the WISHE mechanism of Emanuel (1987). I will use the term "intraseasonal" to describe fields filtered to retain 20-80 day periods, although perpetual March simulations technically do not have seasons. A non-recursive filter having a frequency response with half-power points at 20 and 80 days was used in filtering.

4.3) Frictional Convergence

This section analyzes the relationship between surface convergence and MJO convection, in both the CCM3 with McRAS and observations. Composite intraseasonal equatorial 850 mb zonal wind and precipitation anomalies for the CCM3 with McRAS were shown in Figure 3.14. Model positive precipitation anomalies tend to occur in association with anomalous easterly 850 mb zonal wind anomalies during an MJO lifecycle, unlike observations, where anomalous precipitation is closer to the nodal point in 850 mb zonal wind anomalies. Figure 4.1 displays composite equatorial (5°N-5°S averaged) Xie/Arkin precipitation and NCEP convergence anomalies at 850 mb and 1000mb for an observed MJO composite lifecycle. Note that the contour interval is different for the two plots. Fields are composited based on the first two empirical orthogonal functions (EOFs) of the equatorial 850 mb zonal wind, as described in Maloney and Hartmann (1998, Chapter 2). Observed surface convergence tends to lead precipitation anomalies, and 850 mb conver-

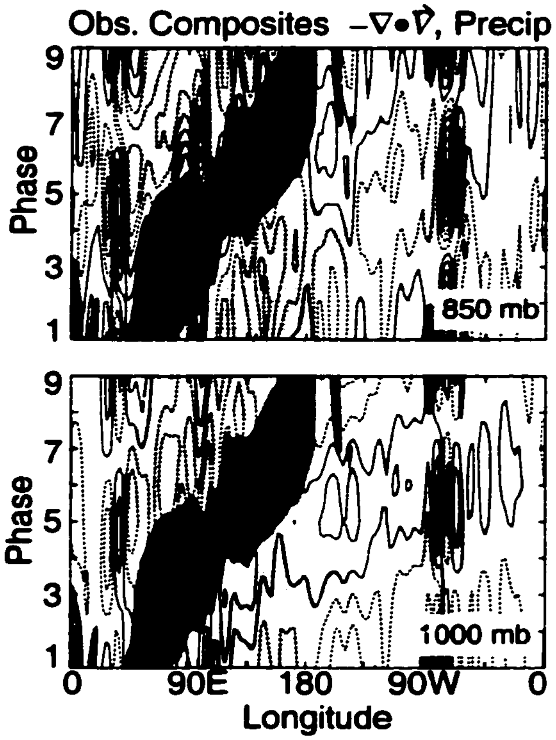

Figure 4.1. Observed composite equatorial 20-80 day NCEP 850 mb and 1000 mb convergence and Xie/Arkin precipitation anomalies as a function of MJO phase. Precipitation anomalies greater (less) than (-)3 mm day^{-1} are shaded dark (light). 850 mb convergences are plotted every 1×10^{-7} s^{-1}, starting at 0.5×10^{-7} s^{-1}. 1000 mb convergences are plotted every 2×10^{-7} s^{-1} starting at 1×10^{-7} s^{-1}. Divergences are dashed.

gence tends to be in phase with enhanced precipitation. Lag-correlations during an observed MJO composite lifecycle between precipitation anomalies and convergence at 850 mb and 1000 mb (5°N-5°S averaged) are shown in Figure 4.2. Correlations significant at the 95% confidence level are shaded. Convergence at 1000 mb over the Indian and western Pacific Oceans generally leads anomalous precipitation by one or two phases. Maximum correlations are near 0.4 over the Indian and western Pacific Oceans. Convergence at 850 mb is most highly correlated with precipitation near zero lag, with values approaching 0.5 over the western Pacific.

The phase relationships between convective precipitation and convergence during a

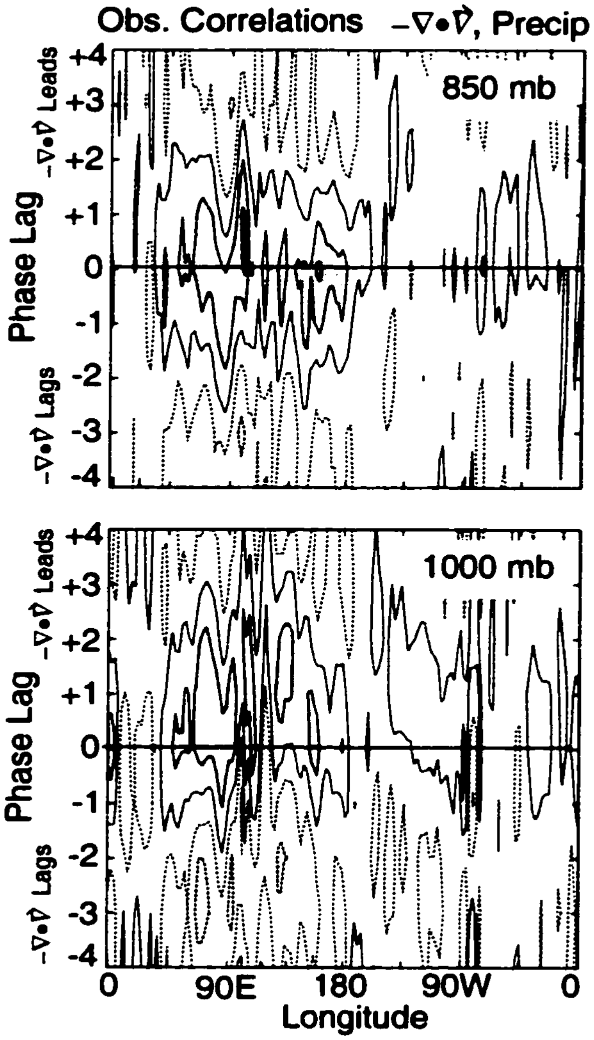

Figure 4.2. Observed lag correlations between 20-80 day equatorial NCEP 850 mb and1000 mb convergence and Xie/Arkin precipitation anomalies during an MJO lifecycle. Correlations are plotted every 0.2, starting at 0.1. Correlations significant at the 95% level are shaded. Negative correlations are dashed.

composite MJO lifecycle in the CCM3 with McRAS are somewhat different than observed. Figure 4.3 displays composite intraseasonal equatorial precipitation anomalies, and convergence anomalies at 850 mb and the surface (7°N-7°S averaged) during an MJO lifecycle in the model. Positive model surface convergence anomalies are coincident with

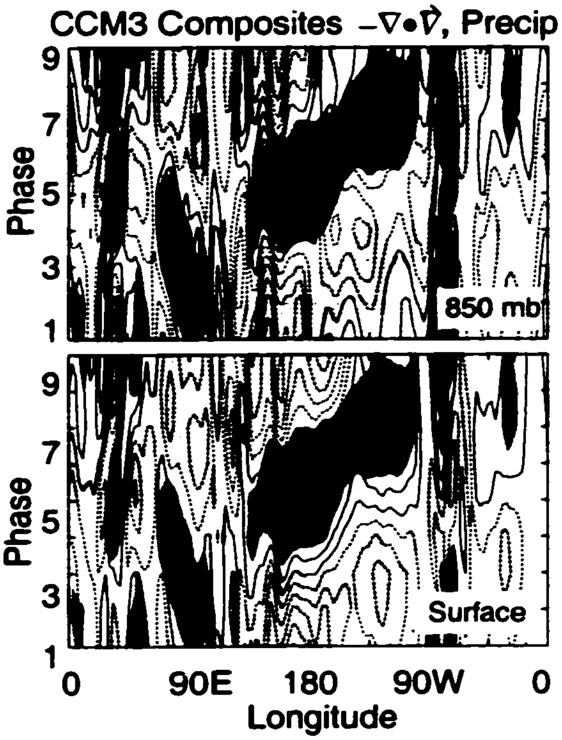

Figure 4.3. Model composite equatorial 20-80 day 850 mb wind, surface convergence, and convective precipitation anomalies as a function of MJO phase. Otherwise, same as Figure 4.1.

850 mb easterly wind anomalies, particularly over the Pacific Ocean (compare with Figure 3.14). Convective precipitation tends to be located within both surface convergence and 850 mb convergence, although surface convergence leads that at 850 mb. Surface convergence anomalies over the central Pacific tend to be 2-3 times stronger than observed. A lag-correlation analysis (Figure 4.4) confirms this relationship. Convergence anomalies at each longitude are correlated with precipitation anomalies at the same longitude as a function of phase lag. Model convective precipitation anomalies during an MJO lifecycle are strongly correlated (greater than 0.7) with surface convergence anomalies at zero lag across the tropics. Correlations with convergence at 850 mb are also strong, but slightly weaker. These results suggest that a strong coupling between intraseasonal surface con-

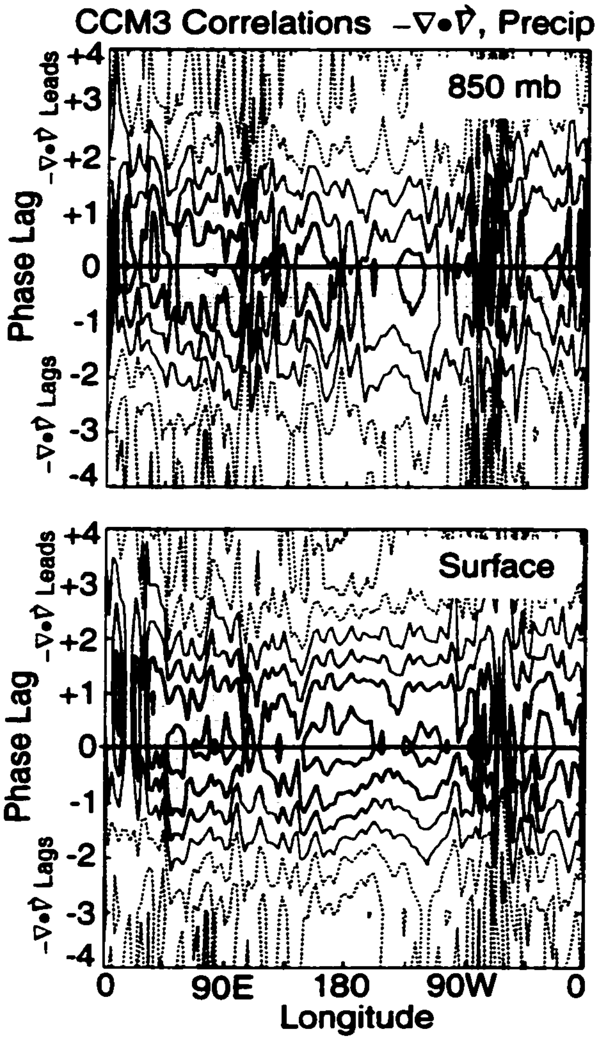

Figure 4.4. Model lag correlations between 20-80 day equatorial 850 mb and surface convergence and convective precipitation anomalies during an MJO lifecycle. Otherwise, same as Figure 4.2.

vergence and convective precipitation is responsible for the coincidence of model easterly 850 mb wind anomalies with convective precipitation. Model convection is more closely tied to surface convergence than observed convection, and equatorial intraseasonal surface convergence is stronger than observed.

Figure 4.5 shows the composite meridional component of surface convergence anomalies as a function of MJO phase for both observations and the CCM3 with McRAS. Meridional convergence onto the equator tends to dominate the convergence signal in

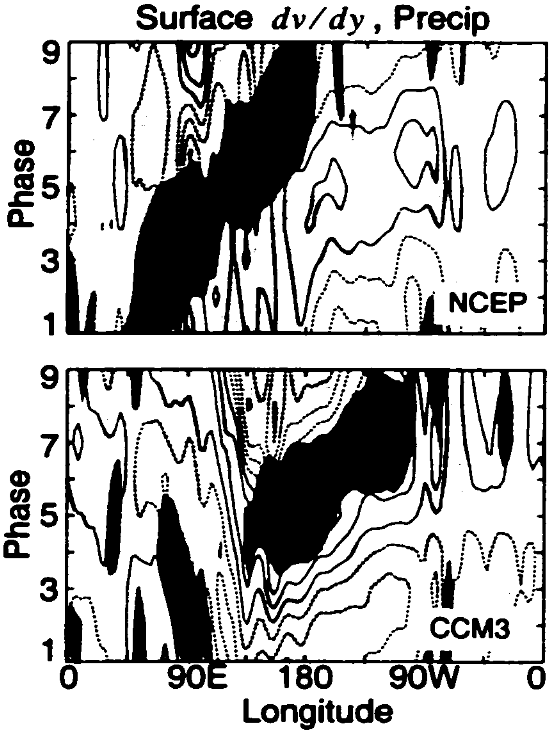

Figure 4.5. Composite 20-80 day meridional surface convergence and precipitation anomalies as a function of MJO phase for observations (1000 mb) and the model. Precipitation anomalies greater (less) than (-)3 mm day^{-1} are shaded dark (light). Convergences are plotted every 2×10^{-7} s^{-1}, starting at 1×10^{-7} s^{-1}. Divergences are dashed.

both observations and the model. Meridional convergence in the model is stronger than observed, especially across the Pacific. The coincidence of meridional convergence anomalies with anomalous easterly 850 mb winds is consistent with anomalous frictional convergence into an equatorial pressure trough, as might be associated with the easterly perturbation region of an equatorial Kelvin wave (Holton 1992).

The spatial distribution of model MJO surface convergence anomalies can be examined to judge their collocation with convective precipitation anomalies. Figure 4.6 maps

CCM3 with McRAS composite 850 mb wind anomalies and surface convergence anomalies for phases 3,5,7, and 9 of an MJO composite lifecycle. The pattern of convergence anomalies looks strikingly similar to the distribution of precipitation in Figure 3.13. This figure reiterates the strong coupling between model convergence and intraseasonal precipitation across the tropics.

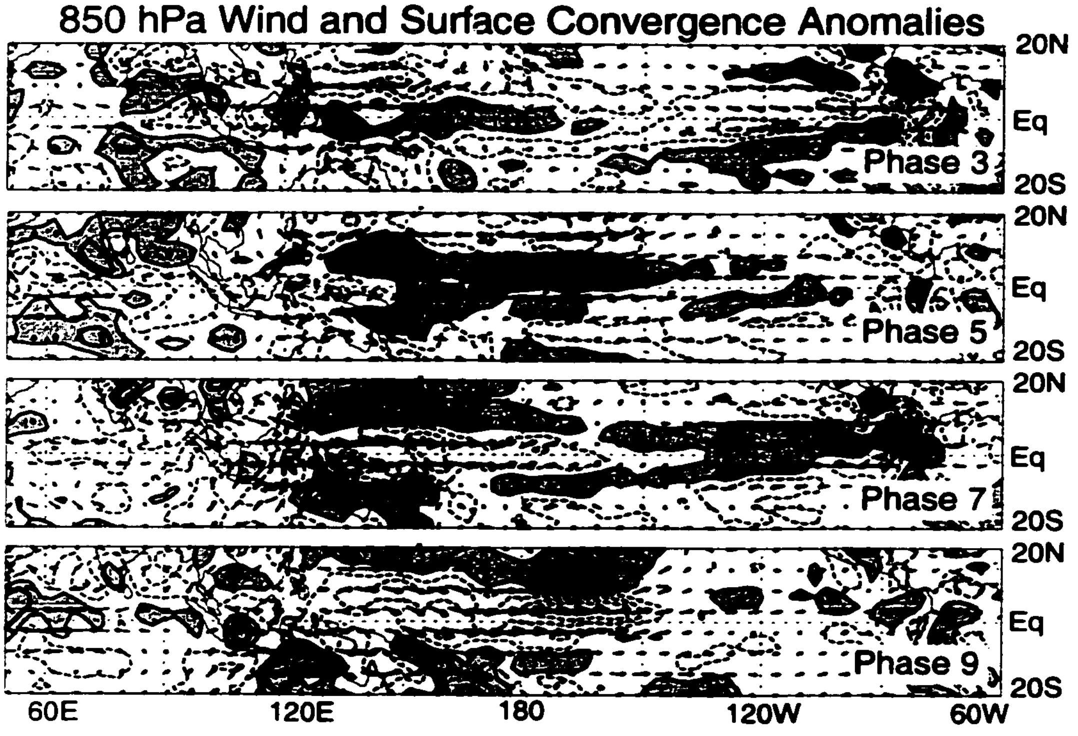

Figure 4.6. Model 20-80 day 850 mb wind and surface convergence anomalies for an MJO composite lifecycle. Phases 3,5,7, and 9 are displayed. Contour interval is 6×10^{-7} s^{-1}, starting at 3×10^{-7} s^{-1}. Divergences are dashed. Maximum vectors are 3.6 m s^{-1}.

Figure 4.7 shows a plot similar to Figure 4.6, but for 850 mb intraseasonal convergence anomalies. The contour interval is that same as in Figure 4.6. Notable is that 850 mb convergence anomalies are much weaker during an MJO lifecycle than those near the surface. Maximum 850 mb anomalies also generally lie west of surface anomalies, highlighting the effects of surface friction. This relationship can be difficult to see at times, since 850 mb convergence anomalies are generally less coherent than those at the surface.

I will next try to determine the means by which the intraseasonal surface convergence field interacts with convection. Correlations between several fields in the lower equatorial troposphere are now examined during an MJO lifecycle in CCM3 with

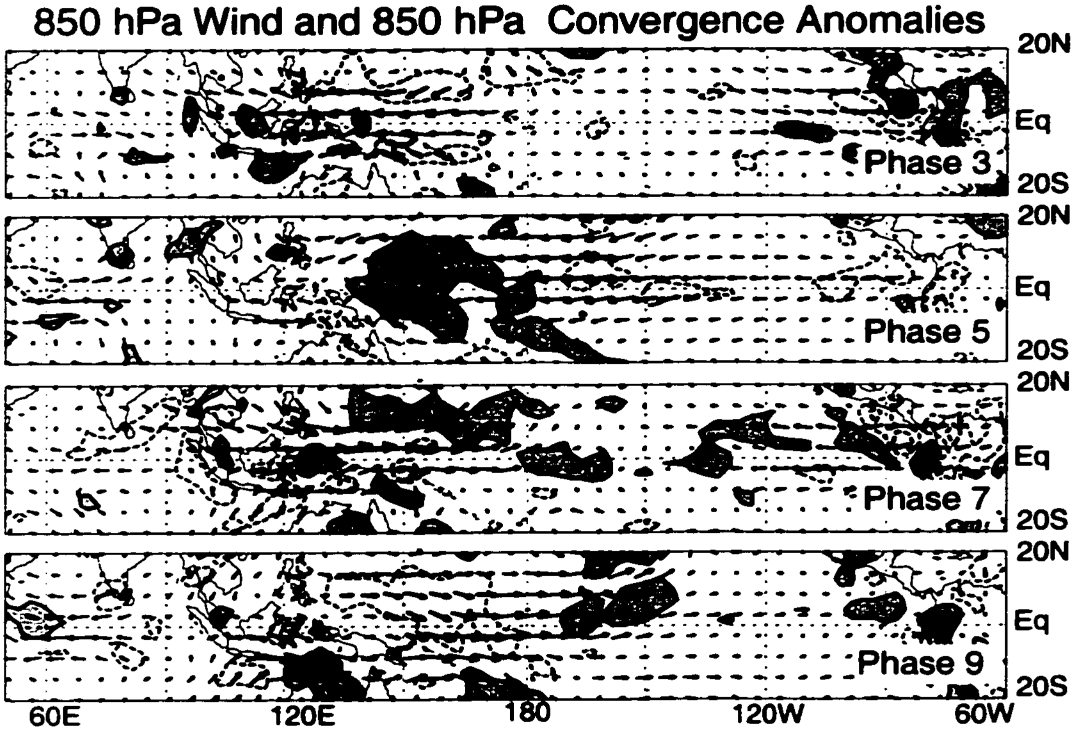

Figure 4.7. Model 20-80 day 850 mb wind and 850 mb convergence anomalies for an MJO composite lifecycle. Phases 3,5,7, and 9 are displayed. Contour interval is 6×10^{-7} s^{-1}, starting at 3×10^{-7} s^{-1}. Divergences are dashed. Maximum vectors are 3.6 m s^{-1}.

McRAS. Equatorial convective precipitation (7°N-7°S averaged) is strongly correlated with lower tropospheric specific humidity (750 mb-990 mb averaged) at zero lag across the tropics during an MJO lifecycle (Figure 4.8a). Correlations of greater than 0.7 can be found across the Indian and western Pacific Oceans. Specific humidity at upper levels (not shown) also has high correlations (0.7 or greater) with convective precipitation, although precipitation tends to lead the humidity signal. I will discuss this phasing between lower-

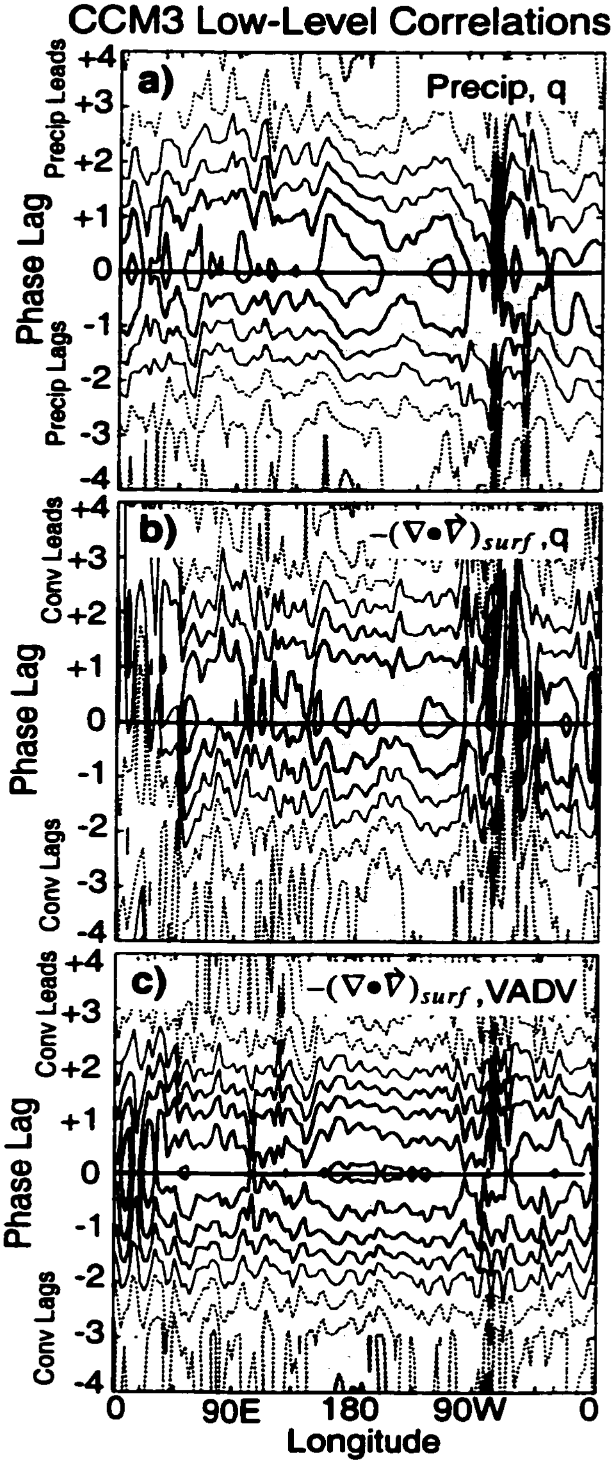

Figure 4.8. Model lag correlations between 20-80 day equatorial a) convective precipitation and low-level q, b) surface convergence and low-level q, and c) surface convergence and low-level moistening by vertical advection during an MJO lifecycle.

level and upper-level specific humidity anomalies later. Correlations between convective precipitation and lower tropospheric temperature (Figure 4.9a) are not as strong as those with specific humidity, suggesting that lower tropospheric water vapor is the dominant regulator of convection during an MJO lifecycle. The temperature signal at upper levels (450-750 mb averaged) shows similarly weak correlations with convective precipitation (Figure 4.9b). Since moisture variations dominate temperature variations in controlling

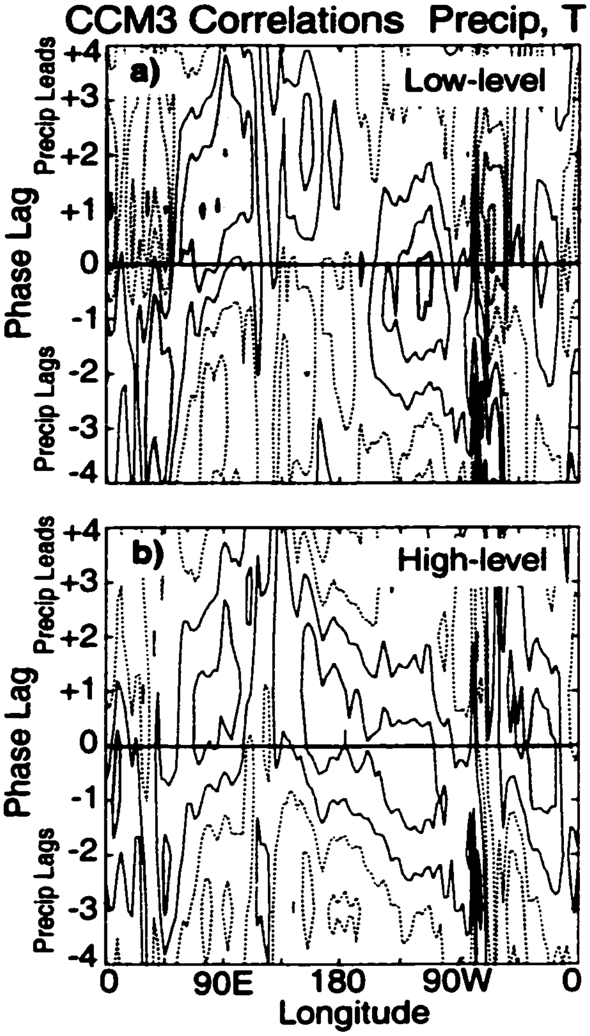

Figure 4.9. Model lag correlations between 20-80 day equatorial convective precipitation and temperature at a) 750-990 mb and b) 450-750 mb. Otherwise, same as Figure 4.2.

convection during the model MJO lifecycle, I will concentrate on the interactions between specific humidity and convection during the rest of this analysis.

Lag-correlations during an MJO lifecycle between model equatorial surface convergence and lower-troposphere specific humidity are shown in Figure 4.8b, and lag-correlations between model equatorial surface convergence and lower-troposphere moistening by vertical advection are shown in Figure 4.8c. Intraseasonal variations in surface convergence are correlated with lower-troposphere water vapor at 0.7 near zero-lag over the Pacific during an MJO lifecycle. Recall that Maloney and Hartmann (1998, Chapter 2) found western Pacific MJO lower tropospheric water vapor and surface convergence to be correlated at 0.4. These results indicate that model surface convergence impacts the MJO lower-tropospheric moisture budget more strongly than in observations, although lower-tropospheric moisture convergence is clearly important to the observed MJO. Surface convergence is correlated at 0.9 with lower-tropospheric moistening by vertical advection, a somewhat expected result due to continuity considerations. I will show below that vertical advection is, by far, the dominant term in moistening the lower troposphere for enhanced model MJO convection.

Examination of the vertical structure of CCM3 specific humidity anomalies as a function of MJO phase can be useful for diagnosing the evolution of the water vapor field. Figure 4.10 shows an equatorial vertical cross-section of model specific humidity anomalies and circulation anomalies at phases 5 and 9 of a composite lifecycle. These phases represent times of peak enhanced and suppressed convection near the dateline. The anomalous circulation is generally baroclinic with upper and lower tropospheric wind anomalies 180° out of phase, as in observations (e.g. Hendon and Salby 1994 and Chapter 2). As the entire signal propagates eastward along the equator, lower-tropospheric specific humidity anomalies lead those at upper levels. Positive specific humidity anomalies grow in regions of surface easterly wind anomalies and rising motion, consistent with moistening by surface convergence (Phase 5). Surface convergence may help precondition the lower troposphere for intense MJO convection. Wang and Schlesinger (1999) similarly found that lower-tropospheric moistening led upper-level moistening during MJO lifecy-

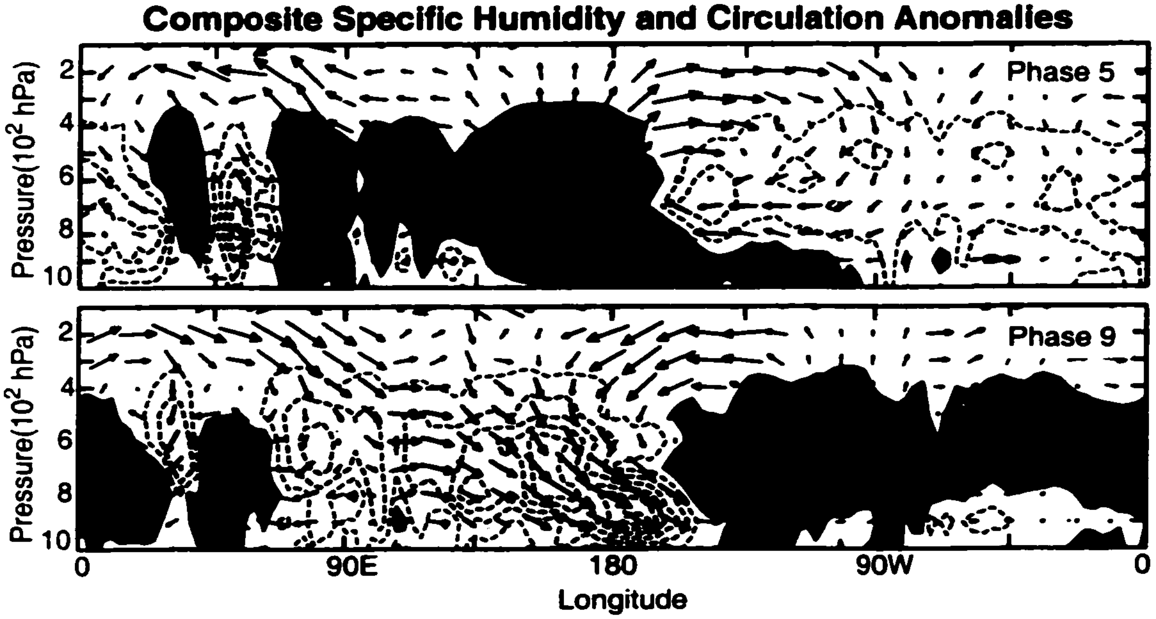

Figure 4.10. Model composite equatorial 20-80 day specific humidity and *u-w* circulation anomalies. MJO phases 5 and 9 are displayed. Contours are plotted every 0.07 g kg^{-1}, starting at 0.035 g kg^{-1}. Negative contours are dashed and lightly shaded. The largest zonal velocity is 2.1 m s^{-1}. The largest vertical velocity is 0.003 m s^{-1}.

cles from several GCM simulations, a result they attributed to low-level moistening by frictional convergence. The CCM3 with McRAS also shows that lower tropospheric dry anomalies are coincident with regions of westerly wind perturbations and sinking motion (Phase 9). Enhanced subsidence may help to dry the lower troposphere after a significant MJO event. Observed westerly MJO perturbations, associated with Rossby gyres to the north and west of equatorial MJO heating, are associated with tropospheric drying (Maloney and Hartmann 1998, Chapter 2).

The vertical structure of the CCM3 equatorial intraseasonal specific humidity signal at 180°E as a function of MJO phase is shown in Figure 4.11. Lower tropospheric specific humidity (below 800 mb) peaks during phase 5, whereas the specific humidity aloft peak during phase 6. Lower tropospheric moisture anomalies appear before those at upper lev-

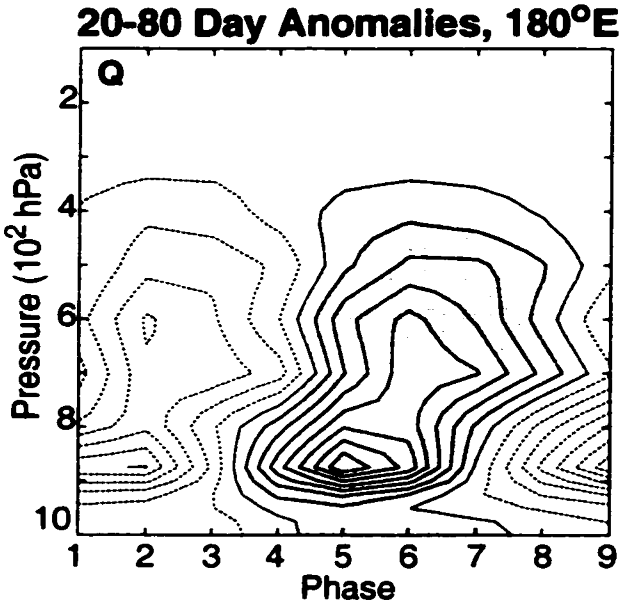

Figure 4.11. Model 20-80 day q anomalies at 180°E as a function of MJO phase. q is plotted every 0.07 g kg^{-1} starting at 0.035 g kg^{-1}. Positive values are shaded.

els. I will examine below the dependence of specific humidity in these vertical layers on various terms in the moisture budget. Figure 4.11 is typical of locations across the central and eastern Pacific Ocean, the regions of most obvious eastward propagation of the MJO signal in the CCM3 with McRAS (see Figure 3.14). At locations over the western Pacific, near the edge of the strong eastward propagating region, model upper and lower tropospheric specific humidity anomalies tend to be in phase (e.g. 150°E, Figure 4.12). A strong coupling of convection with frictional convergence may be important for sustained eastward propagation of the convective signal.

The leading terms that control intraseasonal variations in water vapor during a model MJO lifecycle in both the lower troposphere (where tropospheric moistening first peaks during an MJO lifecycle) and aloft will now be determined. Correlations between model equatorial intraseasonal specific humidity anomalies at 180°E and 1) vertical advection, 2) horizontal advection, 3) downdrafts and rain evaporation, 4) boundary layer

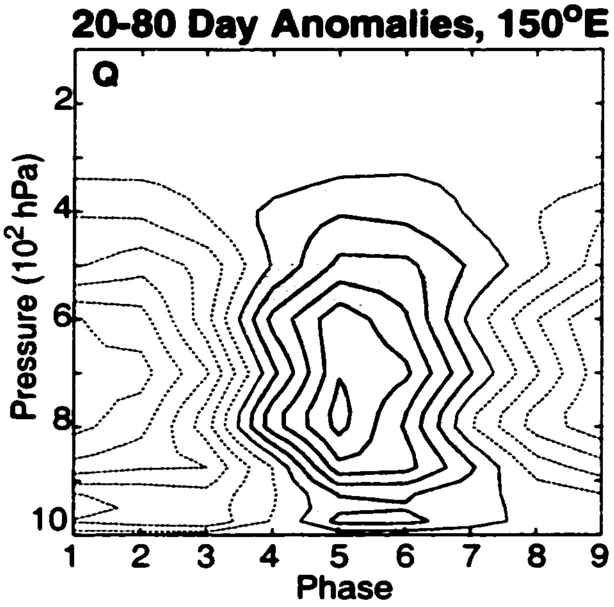

Figure 4.12. Model 20-80 day q anomalies at 150°E as a function of MJO phase. Otherwise, same as Figure 4.11.

diffusion, and 5) convective moistening/drying are shown in Figure 4.13. I neglect terms relating to stratiform clouds and evaporation of cloudwater into the environment, since they do not significantly affect intraseasonal moisture variations. Vertical advection is the term most strongly positively correlated with specific humidity. The correlation approaches 0.8 at lower levels (bottom panel) at zero phase lag. Vertical advection tends to slightly lead specific humidity aloft (top panel), with a correlation peaking near 0.6 at a lag of one phase. Moistening by downdrafts and convective rain evaporation also tends to be highly correlated with intraseasonal specific humidity. Interpretation of this result is difficult in the lower troposphere, however, since dry downdraft air deposited at the lowest model level will be carried upward by the boundary layer vertical diffusion scheme, a mechanism not accounted for by the 750-990 mb averaged correlation in Figure 4.13. The direct contributions to moistening from intraseasonal downdraft and rain evaporation anomalies are small compared to vertical advection, however, as will be shown in Figure

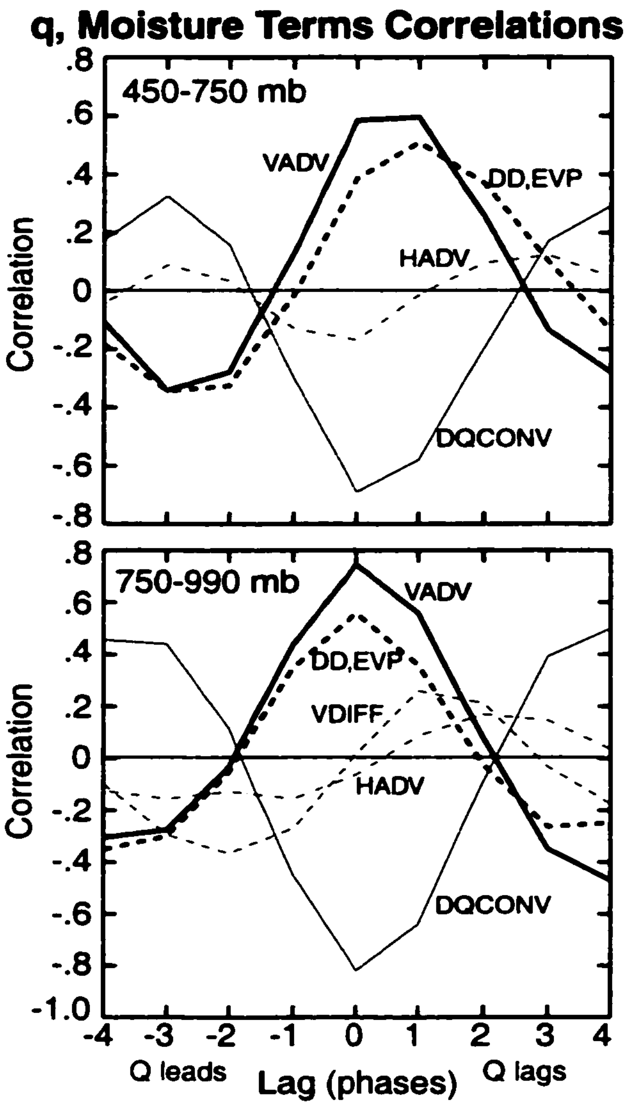

Figure 4.13. Model lag correlations at 180°E, equator between 20-80 day *q* and moisture terms during an MJO lifecycle. Vertical advection (VADV), rain evaporation and downdrafts (DD, EVP), horizontal advection (HADV), convective drying (DQCONV), boundary layer diffusion (VDIFF).

4.14. The intraseasonal moisture tendency due to convective updraft drying/moistening is strongly negatively correlated (-0.7 to -0.8) with specific humidity at both upper and lower levels at zero lag.

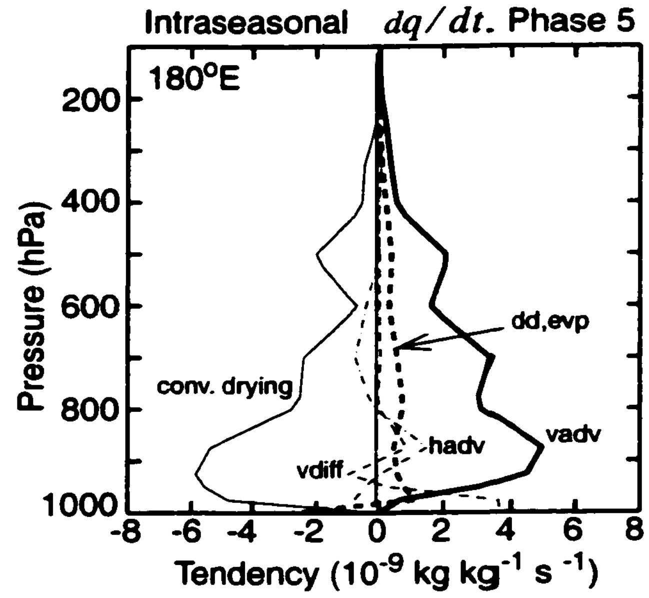

Figure 4.14. Vertical profiles of model 20-80 day equatorial moisture terms at phase 5 of an MJO lifecycle.

Since the highest correlations between intraseasonal specific humidity and lower troposphere moisture tendency terms occur at zero lag in the model, a profile of the vertical moistening terms at the time of peak intraseasonal specific humidity anomalies might be enlightening. Figure 4.14 shows intraseasonal equatorial moisture tendency terms at 180°E during phase 5 of the model composite MJO lifecycle. Apparent is the striking balance between moistening by vertical advection and convective drying. Contributions from downdrafts, boundary layer diffusion, and horizontal advection are relatively small compared to the leading terms. Vertical advection and convective drying also dominate other phases of the MJO composite lifecycle (not shown). Thus, vertical advection would seem to be the dominant term in moistening the lower troposphere during an MJO lifecycle.

By continuity, vertical motion in the lower troposphere implies that convergence must be occurring below. Anomalous moistening near 900 mb due to vertical advection should then closely match upward motion due to convergence anomalies below this level.

I will derive the vertical velocity implied from the continuity equation to check for consistency, and then determine the portion explained by meridional convergence. The pressure velocity at a pressure *P* is given by:

$$\omega(P) = \omega(p_s) - \int_{p_s}^{P} \left(\frac{\partial u}{\partial x} + \frac{\partial v}{\partial y}\right)_p dp \qquad (4.1)$$

Vertical advection of specific humidity at a given level will be given by:

$$VADV = -\omega(p)\frac{\partial q}{\partial p} \qquad (4.2)$$

I will estimate the moistening (7°N-7°S averaged) by vertical advection near 900 mb at phase 5 (see Figure 4.14) due to the anomalous convergence below 900 mb (model levels 16,17, and 18). Assuming that this moistening can be approximated by anomalous vertical advection operating on the mean vertical specific humidity gradient, and that vertical motion at the surface (p_s) is equal to zero., moistening due to anomalous surface convergence produces a specific humidity tendency of 5.7 x 10^{-9} (kg kg^{-1} s^{-1}). This value can explain the anomalous moistening from vertical advection near 900 mb in Figure 4.14. About 80% of this moistening (4.6 x 10^{-9} [kg kg^{-1} s^{-1}]) is contributed by meridional convergence onto the equator, the *dv/dy* component in (1.1), indicating that low-level meridional convergence onto the equator plays a dominant role in the CCM3 McRAS MJO lifecycle.

The coincidence of model anomalous convection with low-level easterly wind perturbations means that positive convective heating anomalies are coincident with anomalous temperature perturbations. Figure 4.15 shows model intraseasonal equatorial temperature and convective heating anomalies, averaged from the surface to model level 8 (near 220 mb in the western Pacific). Zonal means were removed from the fields during filtering. Positive heating anomalies generally lie within positive temperature anomalies during most of the MJO lifecycle, and negative heating anomalies coincide with negative temperature anomalies. This phase relationship holds across the tropical Pacific and Indian Oceans, supported by the strong relationship between convection and surface convergence. Positive correlations of perturbation temperature and convective heating indicate the production of eddy available potential energy (EAPE), which supports equatorial wave growth. Hendon and Salby (1994) found that EAPE production occurs during the amplifying stages of an observed MJO lifecycle. The model MJO is characterized by a longer period of EAPE production, due to the persistent phase relationship between low-level perturbation easterly winds and anomalous convection.

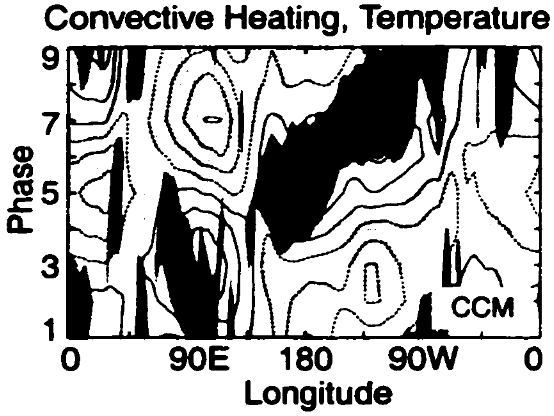

Figure 4.15. Model composite 20-80 day tropospheric mean convective heating and temperature anomalies as a function of MJO phase. The zonal mean was removed in the filtering process. Heating anomalies greater (less) than (-)1.2°K day^{-1} are shaded dark (light). Temperature anomalies are plotted every 0.05°K, starting at 0.025°K. Negative values are dashed.

4.4) WISHE Experiment

A skeptic might say that the bias of convection toward perturbation easterly winds is a sign that the wind-induced surface heat exchange (WISHE) mechanism of Emanuel (1987) plays an important role in the CCM3 with McRAS MJO simulation. The strongest model eastward propagating anomalies occur over the central Pacific, where low-level mean equatorial easterlies are located (see Figure 3.3). I will conduct a simulation in which average March daily wind speeds at each location from a McRAS control simulation are used to calculate the surface flux of evaporation. This simulation will hereafter be referred to as the No-WISHE simulation. This experiment should determine whether WISHE is important in generating the simulated intraseasonal oscillation. Surface evaporation over the ocean in the CCM3 should then only depend on the density of surface air, and the specific humidity deficit across the ocean-air interface (Kiehl et al. 1998). Average daily wind speeds used in calculating of the surface latent heat flux in the No-WISHE simulation are shown in Figure 4.16. The largest tropical average wind speeds are located over the north Pacific. just to the north of the equator, where average daily wind speeds of greater than 9 m s^{-1} can be found. An 8-year perpetual March simulation is conducted

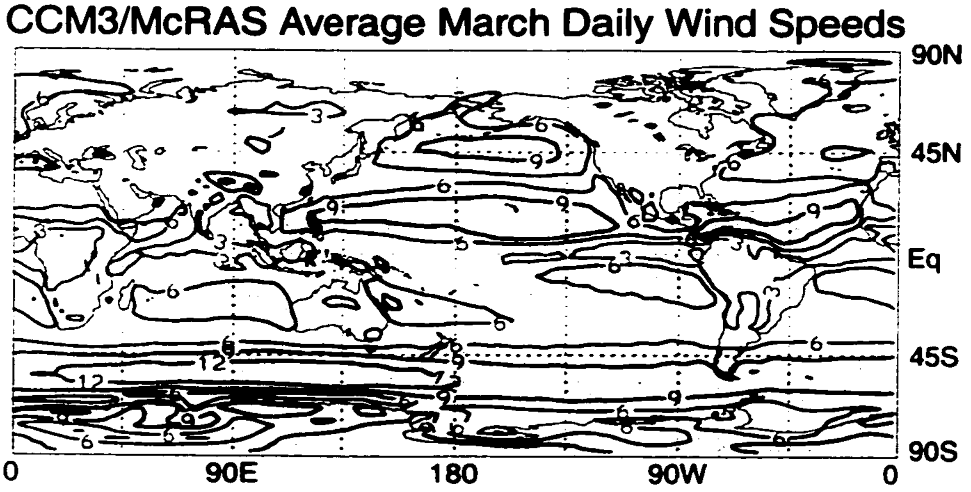

Figure 4.16. Model control simulation March average daily wind speeds. Contour interval is 3 m s^{-1}.

with insolation set at its March 15 value, and SSTs are described by March monthly mean values, as in the control simulation (Figure 3.1).

The climatology of the No-WISHE simulation in zonal winds and precipitation is not significantly different from that of the control simulation (Figure 4.17). Only slight differences in the mean climates can be found, mainly concentrated near the Maritime Continent. The surface latent heat climatology for the No-WISHE simulation, and the difference in climatologies between the control simulation and No-WISHE simulations, are

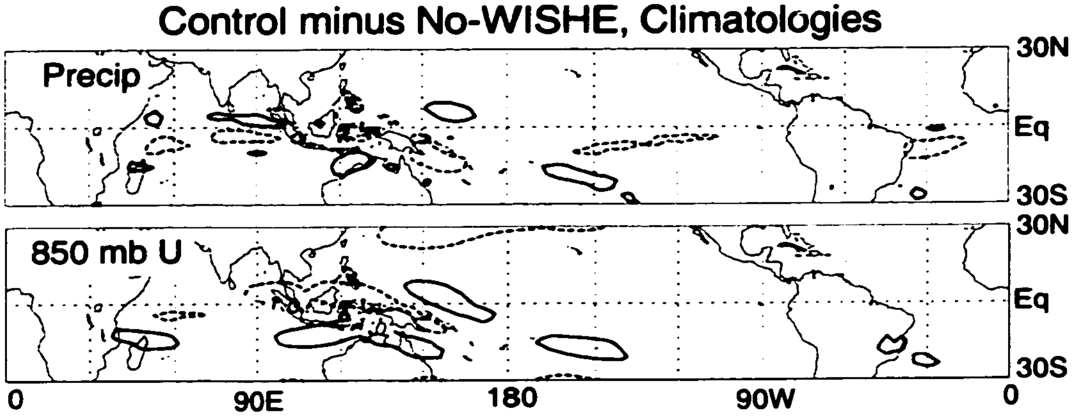

Figure 4.17. Differences in mean precipitation and 850 mb zonal winds between the control and No-WISHE simulations. Contour interval is 3.0 mm day-1 for precipitation, starting at 1.5 mm day^{-1}. Contour interval is 2.0 m s^{-1} for zonal wind, starting at 1.0 m s^{-1}. Negative values are dashed.

shown in Figure 4.18. The latent heat flux climatologies are generally within 10 W m^{-2} of each other across the tropics, with slightly higher differences at a few locations over the far western Pacific. Thus, the model climatology of the No-WISHE simulation seems quite similar to that of the control simulation.

Wavenumber-frequency spectra of equatorial 850 mb zonal wind and convective precipitation for the No-WISHE simulation are shown in Figure 4.19. These can be directly compared to the control simulation spectra in Figures 3.7 and 3.8. Variance in the No-WISHE simulation is more concentrated at wavenumber 1 and intraseasonal periods than in the control simulation. In the control simulation zonal wind spectrum, more higher frequency variance occurs. The control convective precipitation spectrum is also characterized by more westerly variance. The No-WISHE spectra feature prominent peaks near

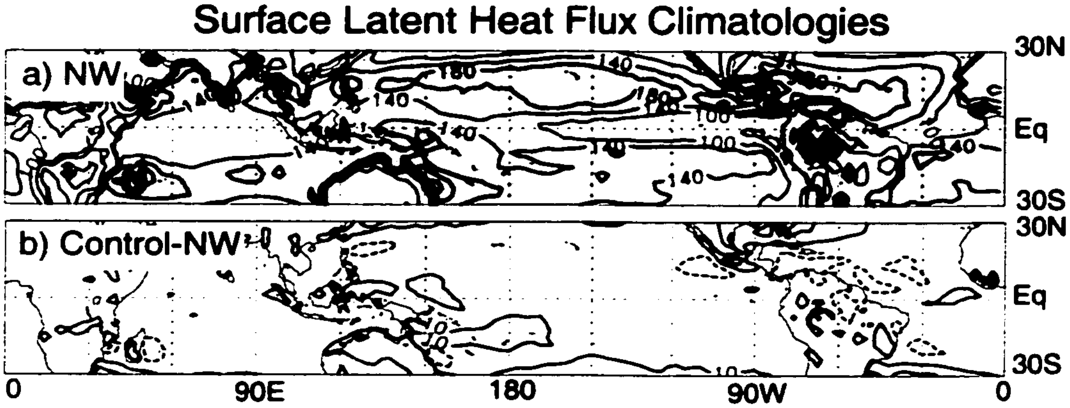

Figure 4.18. Mean surface latent heat flux for the No-WISHE simulation and the difference between the No-WISHE and control simulations. Contour interval in a) is 40 W m^{-2}. The contour interval in b) is 20 W m^{-2}, starting at 10 W m^{-2}.

60 days and wavenumber 1. Removing the WISHE mechanism appears to have created a more robust oscillating signal. Variance at 150 mb is similarly concentrated near wavenumber one and 60 days (not shown). Observed spectra tend to peak near 60 days and wavenumber 1 (Figure 3.6), although precipitation variance from the No-WISHE simulation is, like the control simulation, lower than observed.

Lag regression plots of intraseasonal equatorial NCEP zonal winds at 150 mb and 850 mb during December-May are shown in Figure 4.20. A prominent eastward propagating signal with a change in phase speed across the domain is prominent at both levels. Observed eastward-filtered intraseasonal fields (not shown) look almost identical to the total intraseasonal fields. Lag regression plots are also shown at 150 mb (Figure 4.21) and 850 mb (Figure 4.22) for the No-WISHE simulation (NW) and the 8-year control simulation (C). Model lag-regression plots are displayed for the total intraseasonal fields, and are also decomposed into eastward and westward propagating components. Significant differences between the control and No-WISHE simulations are difficult to detect in amplitude and phase speed. When both eastward and westward components are included, both simulations produce variability that is somewhat noisier than observations. When westward

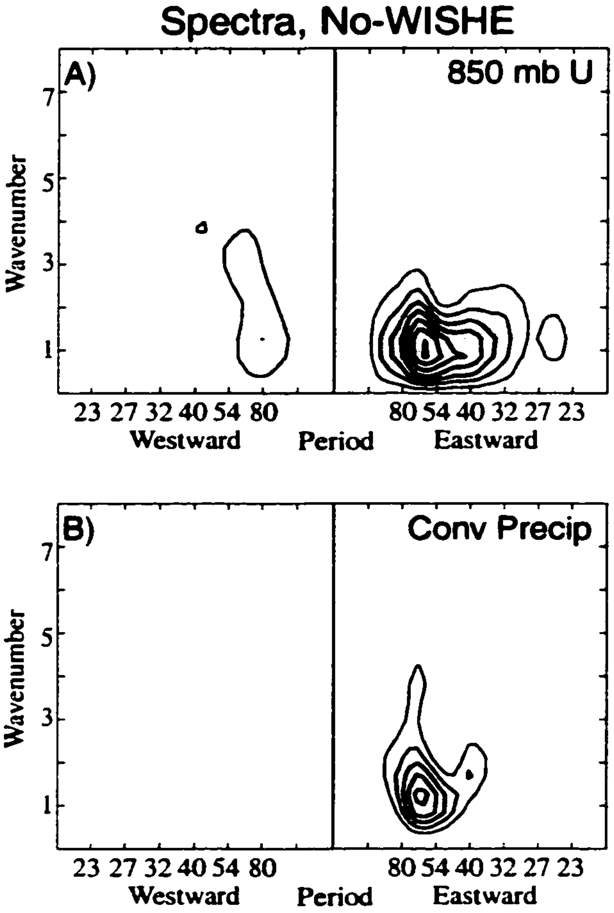

Figure 4.19. Wavenumber-frequency spectra of model 10°N to 10°S averaged a)850 mb zonal wind and b) convective precipitation from the No-WISHE simulation. The zonal wind spectrum contour interval is 3.5 m^2 s^2, starting at 3.5 m^2 s^2. Values greater than 7.0 m^2 s^2 are shaded. The precipitation spectrum contour interval is 0.5 mm^2 day^2, starting at 2.0 mm^2 day^2. Values greater than 2.5 mm^2 day^2 are shaded.

components are removed, however, both simulations produce lag-regression plots that compare very favorably to observations in magnitude and phase speed, with the exception that magnitudes at 150 mb are somewhat diminished from observations. Differences in the height of maximum convective detrainment between observations and the models may partially explain the difference in 150 mb amplitudes. The model eastward propagation

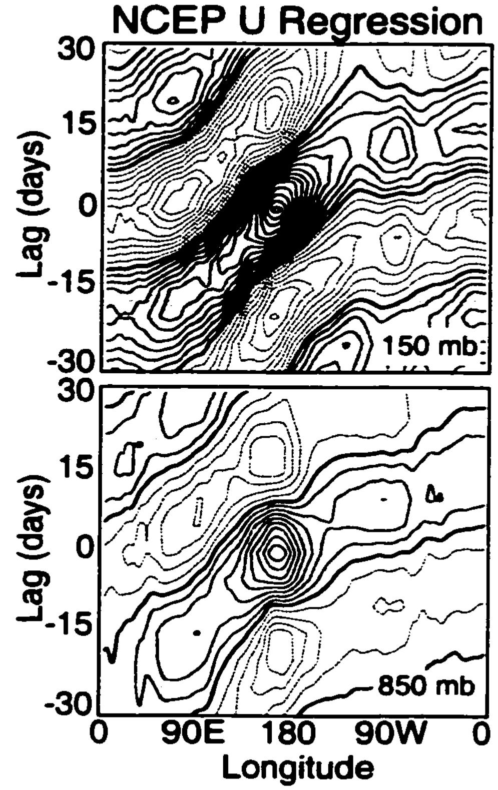

Figure 4.20. Observed lag regression plots of the 20-80 day December-May NCEP a) 150 mb zonal wind and b) 850 mb zonal wind averaged from 10°N to 10°S as a function of longitude. The regression point is 160°E. The 150 mb regression contour interval is 0.3 m s^{-1}, starting at 0.15 m s^{-1}. The 850 mb regression contour interval is 0.2 m s^{-1}, starting at 0.1 m s^{-1}. Positive values are shaded.

speeds at 150 mb are, however, close to those observed. Eastward-filtered 850 mb amplitudes and phase speeds both compare favorably with the observed signal.

A key question that remains is whether the phase relationship between convection and easterly wind anomalies remains the same in the No-WISHE simulation. Although lag-regression analyses and wavenumber-frequency spectra indicate that WISHE is not essential for producing eastward propagating intraseasonal oscillations in the CCM3 with McRAS, the structure of the oscillations need to be examined to confirm that the funda-

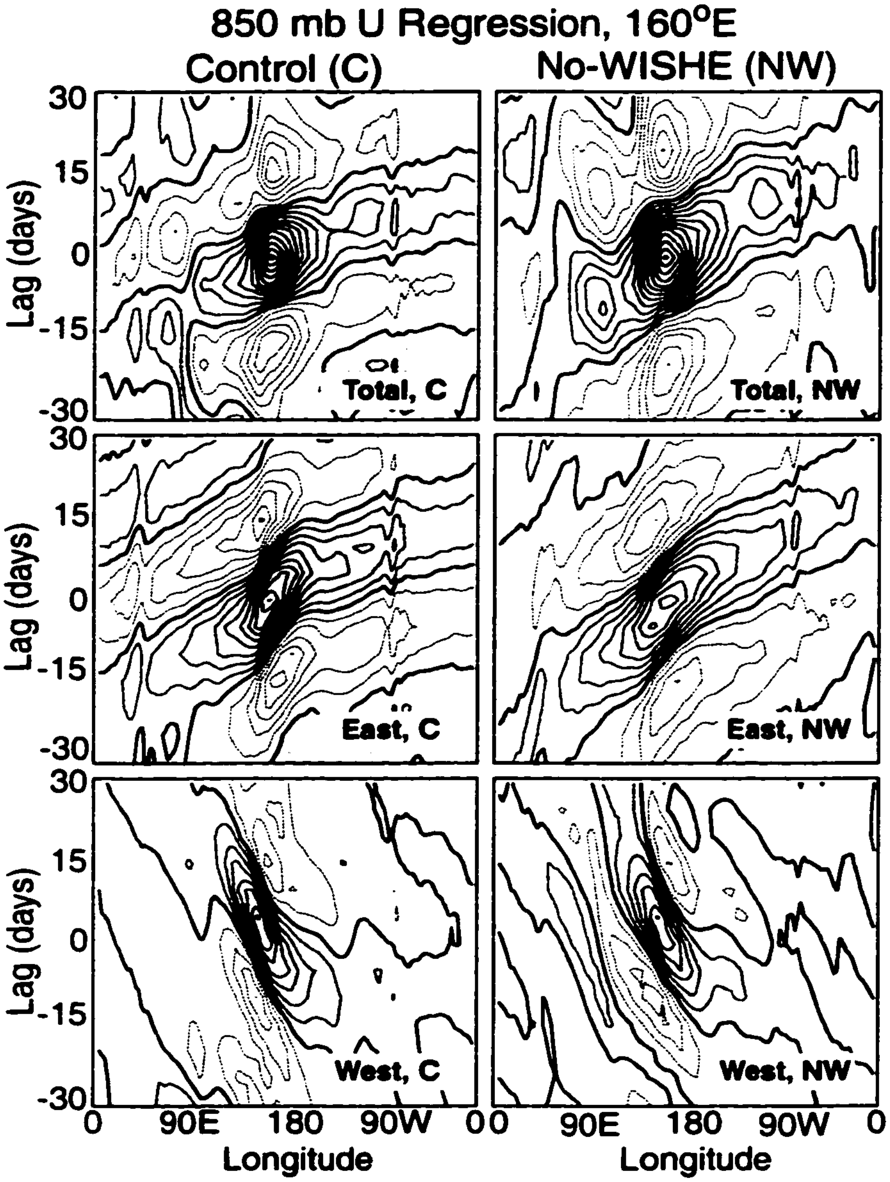

Figure 4.21. Model lag regression plots of the 20-80 day equatorial (7°N to 7°S averaged) 850 mb zonal wind for the control and No-WISHE simulations. The regression point is 160°E. Regressions for all frequencies, eastward frequencies, and westward frequencies are shown. The contour interval is 0.2 m s^{-1}, starting at 0.1 m s^{-1}. Positive values are shaded.

mental nature of the signal remains unaltered.

I will construct an MJO index for the No-WISHE simulation based upon the first

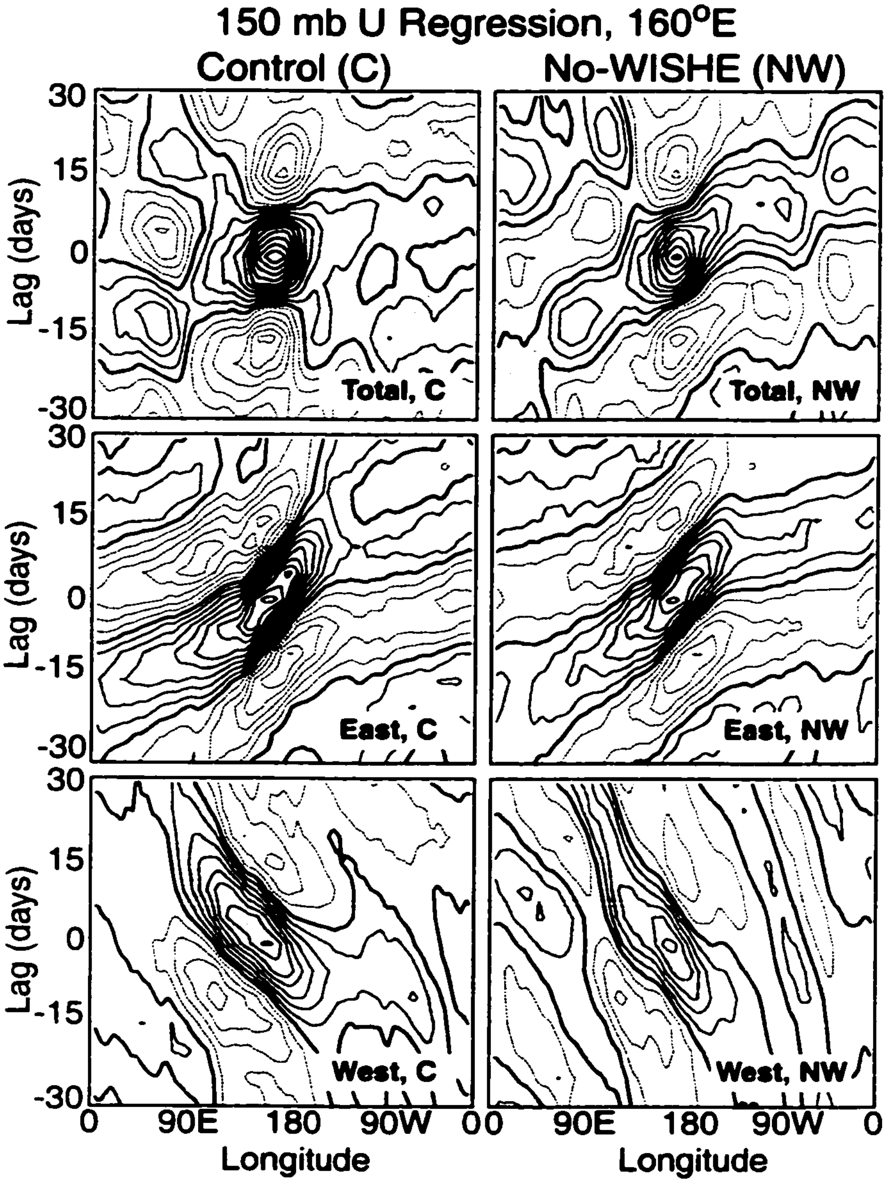

Figure 4.22. Model lag regression plots of the 20-80 day equatorial (7°N to 7°S averaged) 150 mb zonal wind for the control and No-WISHE simulations. The regression point is 160°E. Regressions for all frequencies, eastward frequencies, and westward frequencies are shown. The contour interval is 0.3 m s^{-1}, starting at 0.15 m s^{-1}. Positive values are shaded.

two EOFs of the intraseasonal equatorial (7°N-7°S averaged) 850 mb zonal wind, as was done in MH00 (Chapter 3), and first described by Maloney and Hartmann (1998, Chapter

2). The first two EOFs are displayed in Figure 4.23. The first EOF is similar to that derived from the control simulation (Figure 3.11), and the second has a smoother structure

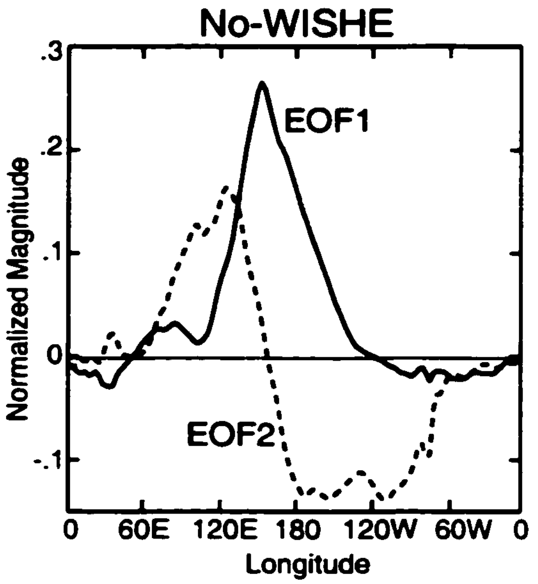

Figure 4.23. First two EOFs of the equatorially averaged (7°N-7°S) 20-80 day 850 mb zonal wind from the No-WISHE simulation. Magnitudes are normalized.

than in the control. Figure 4.24 shows the amount of variance explained by the first 10 EOFs. EOF 1 explains 37% of the variance and EOF 2 explains 20% of the variance. The leading EOFs are significantly different from the rest based on the criterion of North et al. (1982). Recall that the first two EOFs of the control simulation explained 27% and 18% of the variance. Principal components are derived by projecting the EOFs onto the intraseasonal filtered zonal wind data. Lag correlation analysis of the principal components of the first two EOFs indicates that, when PC1 lags PC2 by two pentads, the principal components are correlated at 0.5, and when PC1 leads -PC2 by two pentads, the principal components are correlated at 0.6. These correlations are higher than in the control simulation. The two EOFs explain an eastward propagating signal in the equatorial zonal wind at intraseasonal periods. Based on the amount of variance explained by the leading EOFs,

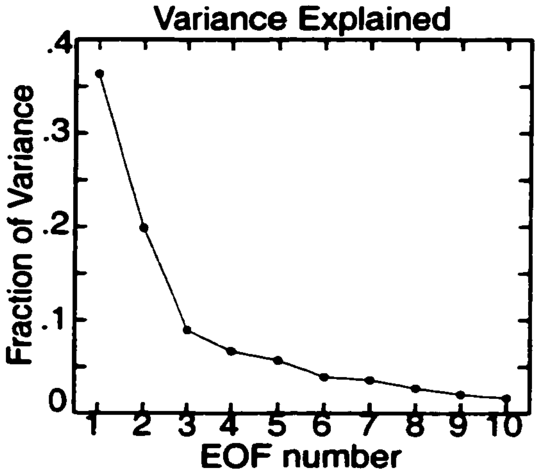

Figure 4.24. Variance explained by the first 10 EOFs of the No-WISHE simulation.

and by the correlations between their principal components, the MJO signal in the No-WISHE simulation stands more prominently above the background variance than in the control simulation. I showed earlier that the control simulation was characterized by more high frequency and westward variance than the No-WISHE simulation (compare Figure 4.19 with Figures 3.6 and 3.7).

Based on the above correlations between the first two PCs, an MJO index can be constructed as follows:, where t is the time in pentads:

$$Index(t) = PC2(t) + PC1(t+2) \qquad (4.3)$$

To check that this index is physically important on intraseasonal timescales, and is not just a construct of the EOF analysis, the index is reconstructed with principal components derived by projection onto the *unfiltered* data. If this index is physically meaningful, a prominent spectral peak should appear at intraseasonal timescales, even when unfiltered data is used in the construction. Figure 4.25 shows a power spectrum of the index constructed from unfiltered principal components. The spectrum is dominated by a significant spectral peak near 60 days, and another near 33 days, confirming that the index explains an actual eastward propagating phenomenon in the model at intraseasonal timescales. The spectral peaks obtained in the No-WISHE simulation, particularly the one near 60 days, are more distinguishable from the background spectrum than those in the control simulation (see Figure 3.12).

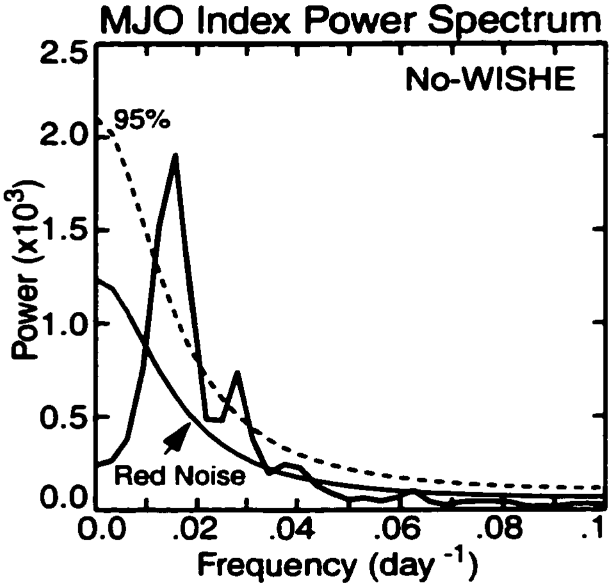

Figure 4.25. Power spectrum of the MJO index from the No-WISHE simulation reconstructed by projecting the first two EOFs onto the unfiltered data. The red noise spectrum is displayed with the *a priori* 95% confidence limit.

Composites are generated by averaging events where the index has peak positive amplitude greater than one standard deviation from zero, as was done in MH00 (Chapter 3). Based on this criterion, 28 events are selected for the No-WISHE simulation. Events average 43 days in length, as opposed to 34 days in length for the control simulation.

Composite MJO 850 mb equatorial (7°N-7°S averaged) zonal wind and convective precipitation anomalies for the No-WISHE simulation are shown in Figure 4.26. A plot of observed composite anomalies is also shown for comparison. Composite anomalies are slightly stronger in the No-WISHE simulation than in the control simulation (Figure

3.14), and coherent eastward propagation extends farther westward into the Indian Ocean. This plot lends credence to my previous observation that removal of the WISHE mechanism leads to a smoother model MJO. Notable, however, is that the phase relationship between easterly anomalies and anomalous convection does not change from the control simulation. WISHE, therefore, cannot explain the preference for anomalous enhanced convection to occur in association with easterly anomalies, and the mechanism responsible is most likely meridional surface convergence onto the equator. Figure 4.27 compares anomalous surface convergence anomalies with convective anomalies for the No-WISHE

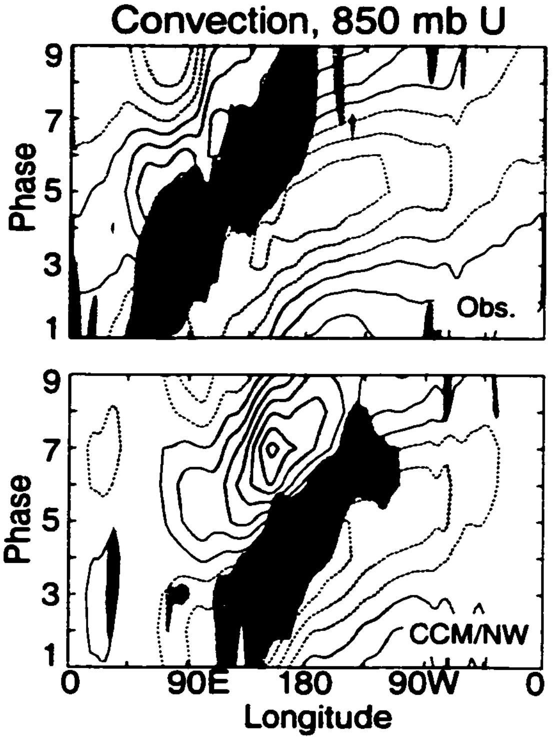

Figure 4.26. Equatorial 20-80 day 850 mb wind (contours) and precipitation (shading) anomalies as a function of MJO phase for a) observations (NCEP winds and Xie/Arkin precipitation, 5°N-5°S averaged) and b) the No-WISHE simulation (7°N to 7°S averaged). Contour interval is 0.50 m s^{-1} starting at 0.25 m s^{-1}. Easterlies are dashed. Dark shading represents precipitation anomalies greater than 0.3 mm day^{-1}. Light shading represents anomalies less than -0.3 mm day^{-1}.

simulation. Anomalous positive convection remains nearly in phase with surface convergence. The majority of this convergence is due to the meridional component, as in the control simulation (not shown).

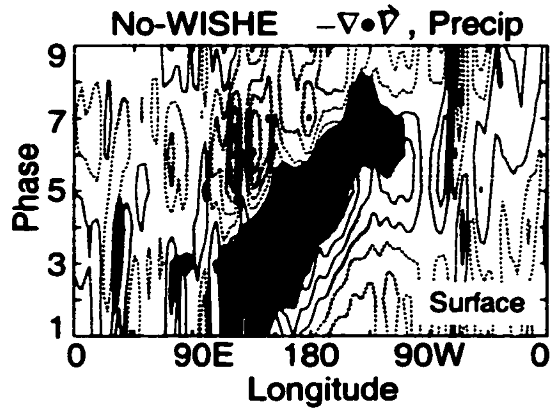

Figure 4.27. No-WISHE simulation composite equatorial 20-80 day 850 mb wind, surface convergence, and convective precipitation anomalies as a function of MJO phase. Otherwise, same as Figure 4.1.

Vertical cross-sections of No-WISHE equatorial intraseasonal specific humidity and circulation anomalies for MJO phases 5, 7, and 9 are also plotted (Figure 4.28). The general trend of low-level humidity anomalies leading those at upper levels remains unchanged from the control simulation (Figure 4.10). The lower troposphere moistens in regions of anomalous surface easterlies (Phase 5), consistent with moistening by anomalous surface convergence. Strong drying occurs at low-levels with the onset of low-level westerly anomalies (Phases 7 and 9). Vertical structures in wind and humidity are somewhat better defined than in the control simulation.

I have shown that the MJO simulated by the No-WISHE simulation stands more prominently above the background variance, and is more coherent than that simulated by the control simulation. An examination of composite intraseasonal surface latent heat flux anomalies from the control and No-WISHE simulations may be useful for explaining some of these differences. Figure 4.29 displays intraseasonal surface latent heat flux anomalies during an MJO composite lifecycle in the No-WISHE simulation, and Figure 4.30 displays anomalies for the control simulation. A positive latent heat flux anomaly designates a net upward flux of latent heat from the surface to the atmosphere. With the

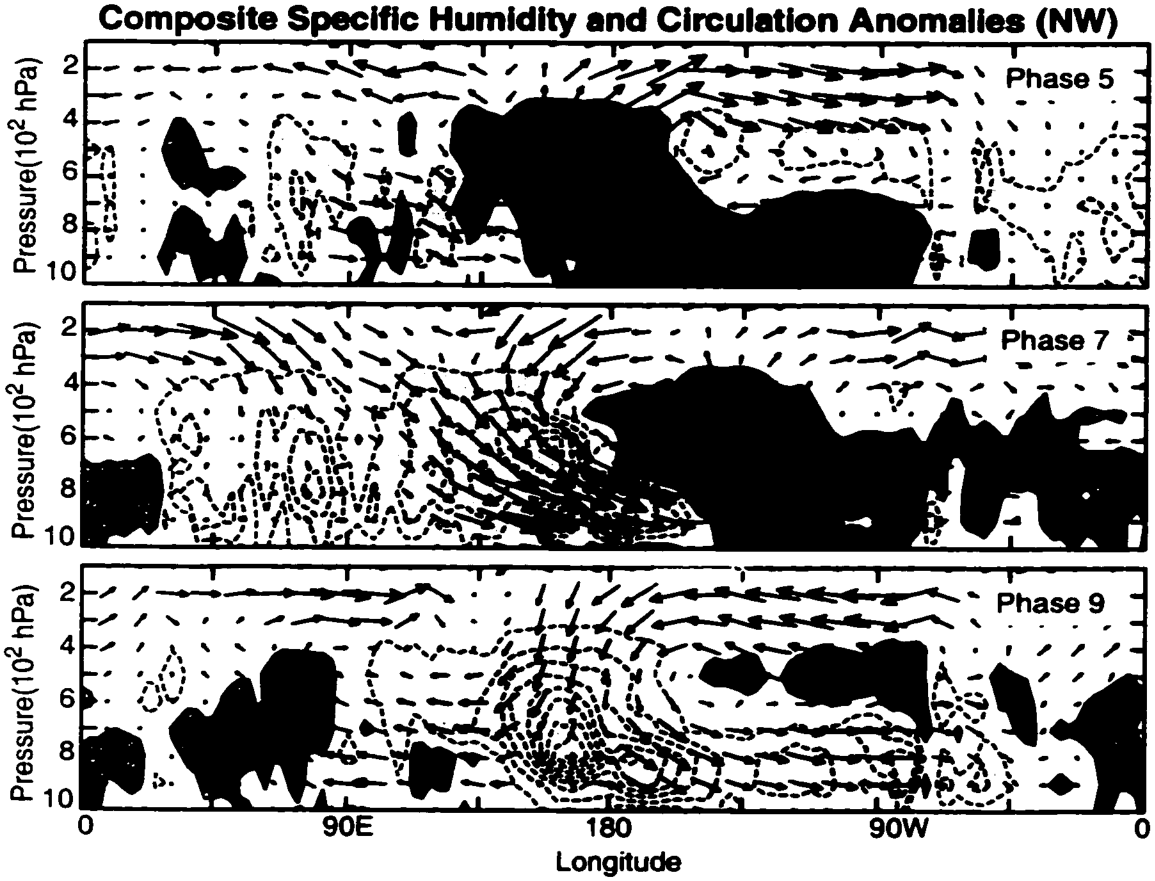

Figure 4.28. No-WISHE composite equatorial 20-80 day specific humidity and *u-w* circulation anomalies. MJO phases 5, 7, and 9 are displayed. Contours are plotted every 0.07 g kg^{-1}, starting at 0.035 g kg^{-1}. Negative contours are dashed and lightly shaded. The largest zonal velocity is 3.4 m s^{-1}. The largest vertical velocity is 0.004 m s^{-1}.

WISHE mechanism removed, the surface latent heat flux over the ocean should only depend on the surface air density and the specific humidity gradient across the ocean-air interface. Tropical latent heat flux anomalies in the No-WISHE simulation are generally 9 W m^{-2} or less during an MJO lifecycle, with the strongest anomalies occurring away from the equator. The regions of strongest equatorial wind anomalies feature very weak latent heat flux anomalies. The amplitudes of latent heat flux anomalies in the control simulation are, however, stronger and more complex. Positive latent heat flux anomalies of 33 W m^{-2} can be found near the Maritime Continent during phase 7. This region corresponds to westerly wind perturbations coinciding with westerly mean winds. Westerly wind anomalies cause negative latent heat flux anomalies farther east, however, when they coincide with mean easterly winds (Phase 9). The area of positive latent heat flux anomalies over

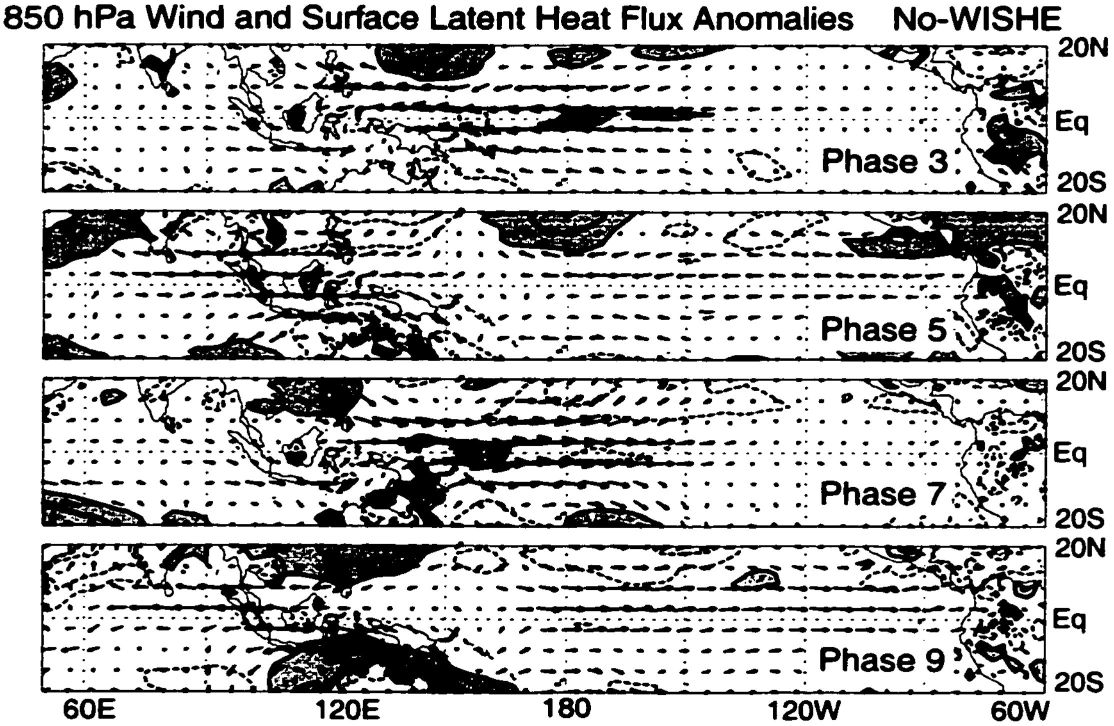

Figure 4.29. No-WISHE simulation 20-80 day 850 mb wind and surface latent heat flux anomalies for an MJO composite lifecycle. Phases 3,5,7, and 9 are displayed. Contour interval is 6 W m^{-2}, starting at 3 W m^{-2}. Negative values are dashed. Maximum vectors are 4.3 m s^{-1}.

the Maritime Continent tends to move westward from Phase 7 to Phase 9, suggesting that the WISHE mechanism may feed westward propagating modes in the control simulation. An area of negative flux anomalies similarly moves westward from phase 3 to phase 5.

Figure 4.3 showed evidence of some westward equatorial precipitation propagation across the Indian Ocean during an MJO lifecycle in the control simulation. This feature may be explained by the strong latent heat flux anomalies over the Maritime Continent and Indian Ocean, to the west of the strongest convective anomalies. The control simulation contains significantly more westward variance in the precipitation spectrum than the No-WISHE simulation (compare Figures 3.8 and 4.19). Latent heat flux anomaly fields are also generally noisier in the control simulation than in the No-WISHE simulation, possibly explaining the increase in high-frequency variance. The WISHE mechanism in the CCM3 with McRAS may help foster convective variability at timescales and wavenumbers outside of the MJO band, thus making eastward propagating MJO-like variability less dominant than it would be in a simulation with the WISHE mechanism removed.

4.5) Conclusions

The NCAR CCM3 with McRAS convection produces an MJO-like intraseasonal oscillation that is highly dependent on frictional convergence. Model MJO convective anomalies show a preference to occur within 850 mb easterly equatorial wind perturbations, where meridional surface convergence onto the equator is strong. Model convective anomalies during an MJO lifecycle are correlated with surface convergence at greater than 0.7 across the Indian and Pacific Oceans, and intraseasonal surface convergence anomalies are similarly strongly correlated with low-level specific humidity anomalies. Correlation analysis also indicates that low-level specific humidity is the dominant regulator of convection during a model MJO lifecycle. The dependence of model MJO convection on temperature is much weaker. Moistening of the lower troposphere within MJO easterly perturbations can be explained by increased lower tropospheric vertical advection associated with anomalous surface convergence (mainly meridional). Tropospheric moistening at lower levels leads that at upper levels during a model MJO lifecycle, especially in regions that contain a strong eastward propagating signal, such as over the central Pacific Ocean. The preference of convective anomalies to lie within low-level perturbation east-

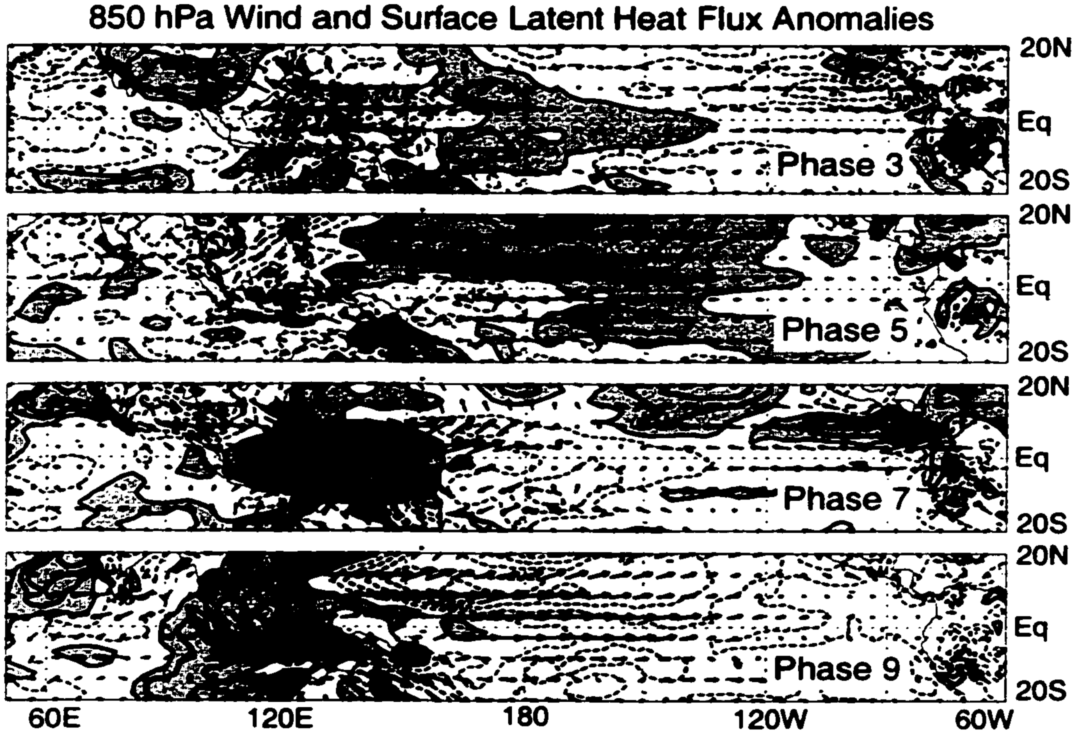

Figure 4.30. Control simulation 20-80 day 850 mb wind and surface latent heat flux anomalies for an MJO composite lifecycle. Phases 3,5,7, and 9 are displayed. Contour interval is 6 W m^{-2}, starting at 3 W m^{-2}. Negative values are dashed. Maximum vectors are 4.6 m s^{-1}.

erly winds leads to eddy available potential energy production throughout a MJO lifecycle, supporting equatorial wave growth.

The observed MJO does show significant correlations between intraseasonal surface convergence and convective anomalies, although those correlations are weaker than in the model (about one-half the strength). Observed surface convergence also tends to lead convection over the western Pacific. Maloney and Hartmann (1998, Chapter 2) found that MJO surface convergence anomalies were significantly correlated with lower tropospheric water vapor anomalies, although not as strongly as in the model. These results suggest that equatorial convection in the CCM3 with McRAS responds more strongly to surface convergence than does convection in nature. Hence, positive convective anomalies in the model tend to occur in association with regions of perturbation easterly winds, where anomalous surface convergence is strongest. Although the phasing of convection with perturbation winds is somewhat different than observed, these model results suggest that surface convergence during an MJO lifecycle is an important regulator of the lower-tropospheric moisture budget during an MJO lifecycle. Maloney and Hartmann (1998, Chapter 3) also found some evidence that convective anomalies grow within MJO perturbation easterly winds (see phase 5), so the phasing between winds and convection in the model may not be completely unrealistic. The modeling results indicate, at the very least, that frictional convergence is a plausible mechanism for producing sustained intraseasonal variability in nature. The results also highlight the importance of realistically simulating boundary layer processes, and their coupling to convection, in atmospheric GCMs.

The wind-induced surface heat exchange mechanism (WISHE) of Emanuel (1987) and Neelin and Yu (1994) is not important to MJO-like intraseasonal variability in the model. Removing the WISHE mechanism by fixing the surface wind speed to climatological values in the computation of the surface heat fluxes may, in fact, lead to a more robust MJO simulation. WISHE may contribute to the growth of modes at frequencies and wavenumbers outside of the MJO band, making the MJO signal less distinguishable from the background variance. The basic structure of the model MJO signal remains unchanged when the WISHE mechanism is removed.

5) Conclusions

This study has demonstrated the importance of frictional surface convergence to the Madden-Julian oscillation (MJO) of the tropical troposphere using both observations and an atmospheric general circulation model (GCM). The sensitivity of GCM intraseasonal variability to changing convective parameterizations was examined in the process. This section will summarize the conclusions from each of the chapters, and provide suggestions for future work. More detailed conclusions can be found at the end of each chapter.

Chapter 2 used NCEP wind reanalyses, MSU precipitation, and NVAP precipitable water to understand the effects of surface convergence during an MJO lifecycle. A composite MJO lifecycle was created using the first two empirical orthogonal functions of 850 mb equatorial zonal wind as an index. Lower tropospheric water vapor over the Indian and western Pacific Oceans was found to be significantly correlated with 1000 mb convergence during an MJO lifecycle. Correlations between water vapor and 850 mb convergence are weaker. Surface convergence tends to slightly lead water vapor anomalies over the western Pacific. Rapid drying occurs after the passage of an MJO convective event. It was concluded that frictional convergence may help to precondition the atmosphere for strong MJO convection by moistening the lower troposphere.

Chapter 3 documented attempts at developing a GCM with realistic intraseasonal variability. Different convection schemes were substituted into the NCAR CCM3 to test their effect on intraseasonal variability. The standard CCM3 convective scheme of Zhang and McFarlane (with the Hack scheme for shallow convection) produces intraseasonal variability that is much lower than observed in zonal winds and precipitation. The McRAS convection scheme, that includes a parameterization of unsaturated convective downdrafts and a relative humidity threshold for convective initiation, produces much improved intraseasonal variability. Intraseasonal zonal wind variance is near observed, and intraseasonal precipitation variance is greatly improved over the control simulation. The phasing between convection and wind anomalies during an MJO lifecycle with McRAS is somewhat different than observed, however, in that positive convection anomalies tend to occur in association with 850 mb perturbation easterly winds. Observed convective anomalies tend to lie closer to the nodal point in 850 mb zonal wind anomalies.

Two other convective schemes were also analyzed in Chapter 3: The Hack scheme and the Emanuel scheme. Zonal wind variability was generally realistic with these two schemes, but precipitation variance was much lower than in observations and in the McRAS scheme. The improvement in intraseasonal variability with the McRAS scheme does not result from the relative humidity threshold for initiation of convection. Variability is actually decreased for higher thresholds, contrary to the results of Wang and Schlesinger (1999). Removal of the unsaturated convective downdraft and rain evaporation parameterization greatly diminishes intraseasonal variability in zonal winds and precipitation. An excessively dry tropical troposphere was shown to be most likely responsible for the degradation of intraseasonal variability.

The CCM3 with McRAS, the model configuration that produces the most realistic intraseasonal variability, was then used in Chapter 4 to study the importance of frictional convergence to the MJO. Model intraseasonal convective anomalies during an MJO lifecycle are strongly correlated with surface convergence at zero lag. Observed MJO convective anomalies are also significantly correlated with surface convergence, although correlations are weaker, and convergence tends to lead convection. Model surface convergences during an MJO lifecycle are generally stronger than in observations. Model surface convergence peaks during periods of perturbation easterlies, explaining the tendency of model positive convective anomalies to lie within 850 mb easterly perturbations.

Low-level MJO specific humidity anomalies in the model are strongly correlated with surface convergence. Where the eastward propagating model MJO signal is strong, low-level specific humidity anomalies precede those at middle and upper levels. Surface convergence affects model convection by moistening the lower troposphere, suggesting that surface convergence during an MJO lifecycle may help to precondition the atmosphere for intense MJO convection. Observed lower tropospheric specific humidities are also significantly correlated with surface convergence anomalies. The agreement of the model and observational results indicates that frictional moisture convergence plays a crucial role in maintaining the Madden-Julian oscillation. Meridional convergence onto the equator contributes most of the anomalous convergence during an MJO lifecycle in both the model and observations.

The wind-induced surface heat exchange (WISHE) mechanism of Emanuel (1987) and Neelin and Yu (1994) is not responsible for producing the MJO-like mode in the CCM3 with McRAS. Removal of the WISHE mechanism, by fixing surface wind speeds to their climatological values in computation of surface latent heat fluxes, does not change the character of the MJO simulation. In fact, the MJO mode explains a greater fraction of the total variance when WISHE is removed, and the simulation is noticeably more robust. WISHE may contribute to the growth of modes outside of the MJO wavenumber-frequency band.

Future work is warranted to explain why model MJO positive convective anomalies occur in association with easterly wind perturbations. Hendon (2000) noticed a similar phase relationship in a GCM study that analyzed the effects of an ocean mixed layer model on the MJO. Convection in the CCM3 with McRAS clearly responds strongly to surface convergence, and the strongest surface convergence coincides with low-level easterly wind perturbations. Why model MJO surface convergence is stronger than in observations, and why model convection responds more strongly to surface convergence than in observations, are unanswered questions. The answer may lie in the atmospheric boundary layer scheme of the CCM3, and how McRAS convection interacts with the boundary layer.

Future work should also include coupling the CCM3 with McRAS convection to a slab ocean model to judge the effect of coupled ocean-atmosphere variations on intraseasonal variability. Waliser et al. (1999) found that coupling an atmospheric GCM to a simple slab ocean model improves model intraseasonal variability. Eastward phase propagation is slowed, and oscillation amplitude is increased. Surface convergence onto the equator is enhanced due to warm SSTs in regions of low-level easterly perturbations. Hendon (2000) found, however, that the coupling of a mixed layer ocean to a GCM did not alter model intraseasonal variability. Hendon attributed this to the tendency for positive convective anomalies in his model to coincide with perturbation easterly winds.

Increased shortwave radiation to the surface and low evaporation conspire to raise SST in regions of anomalous easterlies during an observed MJO lifecycle (Wang and Xie 1998). Shifting convection into surface easterlies reduces the solar flux to the surface there, possibly diminishing the prospects for increased SST. These ideas should be tested in the CCM3 with McRAS convection.

Bibliography

Arakawa, A., and W. H. Schubert, 1974: Interaction of a cumulus cloud ensemble with the large-scale environment, Part I. *J. Atmos. Sci.*, **31**, 674-701.

Bantzer, C. H., and J. M. Wallace, 1996: Intraseasonal variability in tropical mean temperature and precipitation and their relation to the tropical 40-50 day oscillation. *J. Atmos. Sci.*, **53**, 3032-3045.

Betts, A. K., 1976: The thermodynamic transformation of the tropical sub-cloud layer by precipitation and downdrafts. *J. Atmos. Sci.*, **33**, 1008-1020.

Bladé, I., and D. L. Hartmann, 1993: Tropical intraseasonal oscillations in a simple nonlinear model. *J. Atmos. Sci.*, **50**, 2922-2939.

Chang, C.-P., and H. Lim, 1988: Kelvin wave-CISK: A possible mechanism for the 30-50 day oscillations. *J. Atmos. Sci.*, **45**, 1709-1720.

Chao. W. C., and L. Deng, 1997: Phase lag between deep cumulus convection and low-level convergence in tropical synoptic-scale systems. *Mon. Wea. Rev.*, **125**, 549-559.

Chao. W. C., and L. Deng, 1998: Tropical intraseasonal oscillation, super cloud clusters, and cumulus convection schemes. Part II: 3D aquaplanet simulations. *J. Atmos. Sci.*, **55**, 690-709.

Chao, W. C., and S. Lin, 1994: Tropical intraseasonal oscillation, super cloud clusters, and cumulus convection schemes. *J. Atmos. Sci.*, **51**, 1282-1297.

Cheng, M.-D., 1989 Effects of downdrafts and mesoscale convective organizations on heat and moisture budget of tropical cloud clusters. Part II: Effects of convective-scale downdrafts. *J. Atmos. Sci.*, **46**, 1517-1564.

Crum, F. X., and T. J. Dunkerton, 1994: CISK and evaporation-wind feedback with conditional heating on an equatorial beta-plane. *J. Meteor. Soc. Japan*, **72**, 11-18.

Das, S., Y. C. Sud, and M. J. Suarez, 1998: Inclusion of a prognostic cloud scheme with the relaxed Arakawa-Schubert cumulus parameterization: Single-column model studies. *Quart. J. Roy. Meteor. Soc.*, **124**, 2671-2692.

Del Genio, A. D., M.-S. Yao, W. Kovari, and K. K.-W. Lo, 1996: A prognostic cloud water parameterization for global climate models. *J. Climate*, **9**, 270-304.

Dickey, J. O., M. Ghil, and S. L. Marcus, 1991: Extratropical aspects of the 40-50 day oscillation in length-of day and atmospheric angular momentum. *J. Geophy. Res.*, **96**, 22643-22658.

Emanuel, K. A., 1986: An air-sea interaction theory for tropical cyclones. Part I: Steady state maintenance. *J. Atmos. Sci.*, **43**, 585-604.

Emanuel, K. A., 1987: An air-sea interaction model of intraseasonal oscillations in the tropics. *J. Atmos. Sci.*, **44**, 2324-2340.

Emanuel, K. A., and M. Zivkovic-Rothman, 1999: Development and evaluation of a convection scheme for use in climate models. *J. Atmos. Sci.*, **56**, 1766-1782.

Flatau, M., P. J. Flatau, P. Phoebus, and P. P. Niiler, 1997: The feedback between equatorial convection and local radiative and evaporative processes: The implications for intraseasonal oscillations. *J. Atmos. Sci.*, **54**, 2373-2386.

Garstang, M., and A. K. Betts, 1974: A review of the tropical boundary layer and cumulus convection: Structure, parameterization, and modeling. *Bull. Amer. Meteor. Soc.*, **55**, 1195-1205.

Gill, A. E., 1980: Some simple solutions for heat-induced tropical circulation. *Quart. J. R. Met. Soc.*, **106**, 447-462.

Gruber, A., and A. F. Krueger, 1984: The status of the NOAA outgoing longwave radiation data set. *Bull. Am. Meteorol. Soc.*, **65**, 958-962.

Hack, J. J., 1994: Parameterization of moist convection in the National Center for Atmospheric Research community climate model (CCM2). *J. Geophys. Res.*, **99**, 5551-5568.

Hack, J. J., B. A. Boville, B. P. Briegleb, J. T. Kiehl, P. J. Rasch, and D. L. Williamson, 1993: Description of the NCAR community climate model (CCM2), NCAR Tech. Note NCAR/TN-382 + STR, 108 pp. [Available from National Center for Atmospheric Research, Boulder, CO, 80307.]

Hack, J. J., J. T. Kiehl, and J. W. Hurrell, 1998: The hydrologic and thermodynamic characteristics of the NCAR CCM3. *J. Climate*, **11**, 1179-1206.

Hartmann, D. L., and M. L. Michelsen, 1989: Intraseasonal periodicities in Indian rainfall. *J. Atmos. Sci.*, **46**, 2838-2862.

Hartmann, D. L., M. L. Michelsen, and S. A. Klein, 1992: Seasonal variations of intraseasonal oscillations: A 20-25 day oscillation in the western Pacific. *J. Atmos. Sci.*, **49**, 1277-1289.

Hayashi, Y.-Y., and S. Miyahara, 1987: Three-dimensional linear response model of the tropical intraseasonal oscillation. *J. Meteor. Soc. Japan.*, **65**, 843-852.

Hayashi, Y.-Y., and A. Sumi, 1986: The 30-40 day oscillations simulated in an "aqua planet" model. *J. Meteo. Soc. Jap.*, **64**, 451-467.

Hayes, S. P., L. J. Mangum, J. Picaut, A. Sumi, and K. Takeuchi, 1991: TOGA-TAO: A moored array for real-time measurements in the tropical Pacific Ocean. *Bull. Amer. Meteor. Soc.*, **72**, 339-347.

Hendon, H. H., 2000: Impact of air-sea coupling on the Madden-Julian oscillation in a general circulation model. *J. Atmos. Sci.*, in press.

Hendon, H. H., and J. Glick, 1997: Intraseasonal air-sea interaction in the tropical Indian and Pacific Oceans. *J. Climate*, **10**, 647-661.

Hendon, H. H., and B. Liebmann, 1990: The intraseasonal (30-50 day) oscillation of the Australian summer monsoon. *J. Atmos. Sci.*, **47**, 2909-2923.

Hendon, H. H., and M. L. Salby, 1994: The life cycle of the Madden-Julian oscillation. *J. Atmos. Sci.*, **51**, 2225-2237.

Holton, J. R., 1992: *An Introduction to Dynamic Meteorology. 3rd Ed.*, Academic Press, San Diego, 511 pp.

Houze, R. A., Jr., 1977: Structure and dynamics of a tropical squall-line system. *Mon. Wea. Rev.*, **105**, 1540-1567.

Hsu, H.-H., B. J. Hoskins, and F.-F. Jin, 1990: The 1985/86 intraseasonal oscillation and the role of the extratropics. *J. Atmos. Sci.*, **47**, 823-839.

Hu, Q. and D. A. Randall, 1994: Low-frequency oscillations in radiative-convective systems. *J. Atmos. Sci.*, **51**, 1089-1099.

Johnson, R. H., 1976: Role of convective-scale precipitation downdrafts in cumulus and synoptic-scale interactions. *J. Atmos. Sci.*, **33**, 1890-1910.

Jones, C., D. E. Waliser, and C. Gautier, 1998: The influence of the Madden-Julian oscillation on ocean surface heat fluxes and seas surface temperature. *J. Climate*, **11**, 1057-1072.

Jones, C., and B. C. Weare, 1996: The role of low-level moisture convergence and ocean latent heat fluxes in the Madden and Julian oscillation: An observational analysis using ISSCP and ECMWF analyses. *J. Climate*, **9**, 3086-3104.

Kalnay, E., M. Kanamitsu, R. Kistler, W. Collins, D. Deaven, L. Gandin, M. Iredell, S. Saha, G. White, J. Woollen, Y. Zhu, M. Chelliah, W. Ebisuzaki, W. Higgins, J. Janowiak, K. C. Mo, C. Ropelewski, J. Wang, A. Leetmaa, R. Reynolds, R. Jenne, D. Joseph, 1996: The NCEP/NCAR 40-year reanalysis project. *Bull. Am. Meteorol. Soc.*, **77**, 437-471.

Kao, C.-Y. J., and Y. Ogura, 1987: Response of cumulus clouds to large-scale forcing using the Arakawa-Schubert cumulus parameterization. *J. Atmos. Sci.*, **44**, 2437-2458.

Kessler, E., 1969: On the distribution and continuity of water substance in the atmospheric circulation. Meteor Monogr., No. 32, Amer Meteor. Soc., 1-84.

Kiehl, J. T., J. J. Hack, G. B. Bonan, B. A. Boville, D. L. Williamson, and P. J. Rasch, 1998: The
National Center for Atmospheric Research Community Climate Model: CCM3*.
J. Climate, **11**, 1131-1150.

Knutson, T. R., and K. M. Weickmann, 1987: 30-60 day atmospheric oscillations: Composite life cycles of convection and circulation anomalies. *Mon. Wea. Rev.*, **114**, 605-623.

Lau, K.-M., and T. J. Phillips, 1986: Coherent fluctuations of extratropical geopotential height and tropical convection in intraseasonal timescales. *J. Atmos. Sci.*, **43**, 1164-1181.

Lau K.-M., and L. Peng, 1987: Origin of low-frequency (intraseasonal) oscillations in the tropical atmosphere. Part I: Basic theory. *J. Atmos. Sci.*, **44**, 950-972.

Lau, K. M., L. Peng, C. H. Sui, and T. Nakazawa, 1989: Dynamics of super cloud clusters, westerly wind bursts, 30-60 day oscillations, and ENSO: A unified view. *J. Meteor. Soc. Japan*, **67**, 205-219.

Lau K.-M., and C.-H. Sui, 1997: Mechanisms of short-term sea surface temperature regulation: Observations during TOGA COARE. *J. Climate*, **10**, 465-472.

Leary, C. A., and R. A. Houze, Jr., 1979: Structure and evolution of convection in a tropical cloud cluster. *J. Atmos. Sci.*, **36**, 437-457.

Lindzen, R. S., and S. Nigam, 1987: On the role of sea surface temperature gradients in forcing low-level winds and convergence in the tropics. *J. Atmos. Sci.*, **44**, 2418-2436.

Lord, S. J., W. C. Chao, and A. Arakawa, 1982: Interaction of a cumulus cloud ensemble with the large-scale environment. Part IV: The discrete model. *J. Atmos. Sci.*, **39**, 104-113.

Madden, R. A., 1986: Seasonal variations of the 40-50 day oscillation in the tropics. *J. Atmos. Sci.*, **43**, 3138-3158.

Madden, R. A., and P. R. Julian, 1971: Detection of a 40-50 day oscillation in the zonal wind in the tropical Pacific. *J. Atmos. Sci.*, **28**, 702-708.

Madden, R. A., and P. R. Julian, 1972: Description of global scale circulation cells in the tropics with a 40-50 day period. *J. Atmos. Sci.*, **29**, 1109-1123.

Madden, R. A., and P. R. Julian, 1994: Observations of the 40-50-day tropical oscillation - A review. *Mon. Wea. Rev.*, **122**, 814-837.

Maloney, E. D., and D. L. Hartmann, 1998: Frictional moisture convergence in a composite life cycle of the Madden-Julian oscillation. *J. Climate*, **11**, 2387-2403.

Maloney, E. D., and D. L. Hartmann, 2000a: Modulation of eastern north Pacific hurricanes by the Madden-Julian oscillation. *J. Climate*, **13**, 1451-1460.

Maloney, E. D., and D. L. Hartmann, 2000b: Modulation of Gulf of Mexico and Caribbean Sea hurricanes by the Madden-Julian oscillation. *Science*, **287**, 2002-2004.

Maloney and Hartmann, 2000c: The sensitivity of intraseasonal variability in the NCAR CCM3 to changes in convective parameterization. *J. Climate*, submitted.

Manabe, S., and R. F. Strickler, 1964: Thermal equilibrium of the atmosphere with a convective adjustment. *J. Atmos. Sci.*, **21**, 361-385.

Matsuno, T., 1966: Quasi-Geostrophic Motions in the Equatorial Area. *J. Meteor. Soc. Japan*, **44**, 25-42.

Meehl, G. A., and others, 1996: Modulation of equatorial subseasonal convective episodes by tropical-extratropical interaction in the Indian and Pacific Ocean regions. *J. Geophys. Res.*, **101**, 15033-15049.

Molinari, J., and T. Corsetti, 1985: Incorporation of cloud-scale and mesoscale downdrafts into a cumulus parameterization: Results of one- and three-dimensional integrations. *Mon. Wea. Rev.*, **113**, 485-501.

Moorthi, S., and M. J. Suarez, 1992: Relaxed Arakawa-Schubert: A parameterization of moist convection for general circulation models. *Mon. Wea. Rev.*, **120**, 978-1002.

Neelin, J. D., and J. Yu, 1994: Modes of tropical variability under convective adjustment and the Madden-Julian oscillation. Part I: analytical theory. *J. Atmos. Sci.*, **51**, 1876-1894.

North, G. R., T. L. Bell, R. F. Cahalan, and F. J. Moeng, 1982: Sampling errors in the estimation of empirical orthogonal functions. *Mon. Wea. Rev.*, **110**, 699-706.

Park, C. K., D. M. Straus, and K. M. Lau, 1990: An evaluation of the structure of tropical intraseasonal oscillations in three general circulation models. *J. Meteor. Soc. Japan.*, **68**, 403-417.

Randall, D. A., 1989: Cloud parameterization for climate models: Status and prospects. *Atmos. Res.*, **23**, 341-361.

Randel, D. L., T. H. Vonder Haar, M. A. Ringerud, G. L. Stephens, T. J. Greenwald, and C. L. Combs, 1996: A new global water vapor dataset. *Bull. Am. Meteorol. Soc.*, **77**, 1233-1246.

Raymond, D. J., and D. J. Torres, 1998: Fundamental moist modes of the equatorial troposphere. *J. Atmos. Sci.*, **55**, 1771-1790.

Salby, M. L., R. R. Garcia, and H. H. Hendon, 1994: Planetary-scale circulations in the presence of climatological and wave-induced heating. *J. Atmos. Sci.*, **51**, 2344-2367.

Salby, M. L., and H. H. Hendon, 1994: Intraseasonal behavior of clouds, temperature, and motion in the tropics. *J. Atmos. Sci.*, **51**, 2220-2237.

Seager, R., and S. E. Zebiak, 1994: Convective interaction with dynamics in a linear primitive equation model. *J. Atmos. Sci.*, **51**, 1307-1331.

Seager, R., and S. E. Zebiak, 1995: Simulation of tropical climate with a linear primitive equation model. *J. Climate*, **8**, 2497-2520.

Shea, D. J., K. E. Trenberth, and R. W. Reynolds, 1992: A global monthly sea surface temperature climatology. *J. Climate*, **5**, 987-1001.

Slingo, J. M., and other authors, 1996: Intraseasonal oscillations in 15 atmospheric general circulation models: results from an AMIP diagnostic subproject. *Clim. Dyn.*, **12**, 325-357.

Spencer, R. W., 1993: Global ocean precipitation from the MSU during 1979-91 and comparisons to other climatologies. *J. Climate*, **6**, 1301-1326.

Sud, Y. C., and A. Molod, 1988: The roles of dry convection, cloud-radiation feedback processes, and the influence of recent improvements in the parameterization of convection in the GLA GCM. *Mon. Wea. Rev.*, **116**, 2366-2387.

Sud, Y. C., and G. K. Walker, 1993: A rain evaporation and downdraft parameterization to complement a cumulus updraft scheme and its evaluation using GATE data. *Mon. Wea. Rev.*, **121**, 3019-3039.

Sud, Y. C., and G. K. Walker, 1999a: Microphysics of clouds with the relaxed Arakawa-Schubert scheme (McRAS). Part I: Design and evaluation with GATE phase III data. *J. Atmos. Sci.*, **56**, 3196-3220.

Sud, Y. C., and G. K. Walker, 1999b: Microphysics of clouds with the relaxed Arakawa-Schubert scheme (McRAS). Part II: Implementation and performance in the GEOS II GCM. *J. Atmos. Sci.*, **56**, 3221-3240.

Tiedtke, M., 1993: Representation of clouds in large-scale models. *Mon. Wea. Rev.*, **121**, 3040-3061.

Trenberth, K. E., and C. J. Guillemot, 1995: Evaluation of the global atmospheric moisture budget as seen from analyses. *J. Climate*, **8**, 2255-2272.

Waliser, D. E., K. M. Lau, and J. H. Kim, 1999: The influence of coupled sea surface temperatures on the Madden-Julian oscillation: A model perturbation experiment. *J. Atmos. Sci.*, **56**, 333-358.

Wang, B., and T. Li., 1994: Convective interaction with boundary-layer dynamics in the development of a tropical intraseasonal system. *J. Atmos. Sci.*, **51**, 1386-1400.

Wang, B., and H. Rui, 1990: Dynamics of the coupled moist Kelvin-Rossby wave on an equatorial beta-plane. *J. Atmos. Sci.*, **47**, 397-413.

Wang, B., and X. Xie, 1998: Coupled modes of the warm pool climate system. Part I: The role of air-sea interaction in maintaining the Madden-Julian oscillation. *J. Climate*, **11**, 2116-2135.

Wang, W., and M. E. Schlesinger, 1999: The dependence on convective parameterization of the tropical intraseasonal oscillation simulated by the UIUC 11-layer atmospheric GCM. *J. Climate*, **12**, 1423-1457.

Webster, P. J., 1987: The elementary monsoon. *Monsoons*, J. S. Fein and P. L. Stephens Eds., John Wiley and Sons, NY, 3-32.

Weickmann, K. M., and S. J. S. Khalsa, 1990: The shift of convection from the Indian Ocean to the western Pacific Ocean during a 30-60 day oscillation. *Mon. Wea. Rev.*, **118**, 964-978.

Wheeler, M., and G. N. Kiladis, 1999: Convectively coupled equatorial waves: Analysis of clouds and temperature in the wavenumber-frequency domain. *J. Atmos. Sci.*, **56**, 374-399.

Xie, P., and P. A. Arkin, 1996: Analyses of global monthly precipitation using gauge observations, satellite estimates, and numerical model predictions. *J. Climate*, **9**, 840-858.

Xie, S. P., A. Kubokawa, and K. Kanawa, 1993: Evaporation-wind feedback and the organizing of tropical convection on the planetary scale. Part I: Quasi-linear instability. *J. Atmos. Sci.*, **50**, 3873-3883.

Yu, J.-Y., and J. D. Neelin, 1994: Modes of tropical variability under convective adjustment and the Madden-Julian oscillation. Part II: Numerical results. *J. Atmos. Sci.*, **51**, 1895-1914.

Zhang, G. J., and McFarlane, N. A., 1995: Sensitivity of climate simulations to the parameterization of cumulus convection in the Canadian Climate Centre General Circulation Model. *Atmosphere-Ocean*, **33**, 407-446.

Zipser, E. J., 1977: Mesoscale and convective-scale downdrafts as distinct components of squall line structure. *Mon. Wea. Rev.*, **105**, 1568-1589.

Appendix A: Western Pacific TAO vs. NCEP comparison

Tropical Atmosphere Ocean (TAO) buoy array data (Hayes et al. 1991) can be used to check the accuracy of the 1000 hPa NCEP/NCAR reanalysis product over the western Pacific. A comparison between the two datasets can at least indicate how well the reanalysis model assimilates surface wind observations. TAO buoy winds at 165°E (latitudes 5°N, 2°N, 0°, 2°S, and 5°S) were compared to 1000 mb reanalysis winds at 165°E (latitudes 5°N, 2.5°N, 0°, 2.5°S, and 5°S) during February of 1988 through December of 1995. Only days where both TAO and NCEP data were present are used in the comparison.

Monthly climatologies for January, April, July, and October are compared in Figure A1.1. Reanalysis and TAO surface wind climatologies are similar during January and April in both magnitude and direction. The two wind products do not agree as closely during July and October, especially at locations to the south of the equator, where wind magnitudes are stronger in the reanalysis product, and the wind direction has a more southerly component.

MJO studies are more dependent on the reliability of reanalysis wind variations than on the reliability of wind climatologies. Figure A1.2 compares reanalysis and TAO surface wind anomalies (annual cycle removed) at 165°E as a function of phase of the MJO. Phases were determined using the index of Maloney and Hartmann (1998). Phases 3,4,7, and 8 are displayed. The reanalysis product and TAO array anomaly winds generally agree in direction. Agreement in magnitude is also fairly reasonable, although the TAO array anomalies during phases 7 and 8 are generally stronger than the reanalysis product anomalies.

Since frictional moisture convergence may be an important mechanism for the MJO, the reanalysis wind field must be able to properly analyze the observed surface convergence field. Figure A1.3 compares TAO and NCEP meridional convergence anomalies at 165°E during an MJO lifecycle. Equatorial meridional convergence anomalies are 50-100% larger than zonal convergence anomalies during an MJO lifecycle (not shown). A

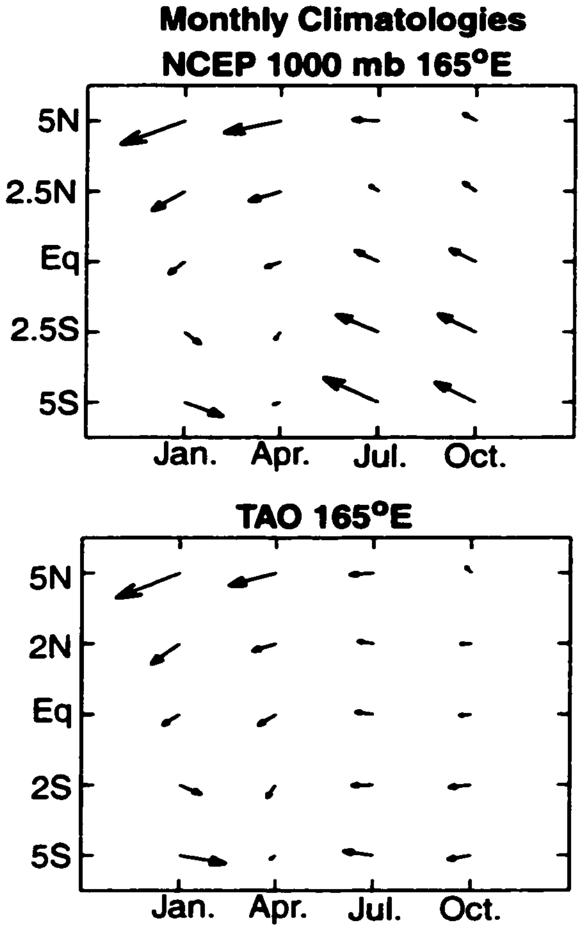

Figure A1.1. NCEP and TAO wind climatologies for January, April, July, and October. The largest vector shown is 5.8 m s^{-1}.

comparison of zonal convergence anomalies is assumed to produce similar results. TAO and NCEP meridional convergence anomalies are comparable during an MJO lifecycle. This result helps legitimize the use of western Pacific NCEP reanalyses in studying MJO-related frictional moisture convergence.

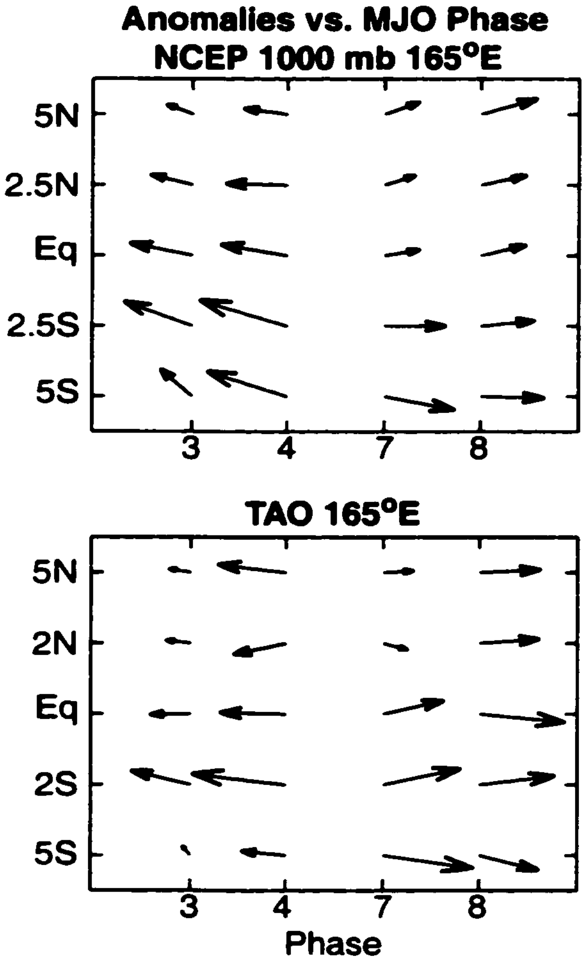

Figure A1.2. NCEP and TAO wind anomalies as a function of MJO phase. Phases 3, 4, 7, and 8 are shown. The largest vector shown is 1.5 m s^{-1}.

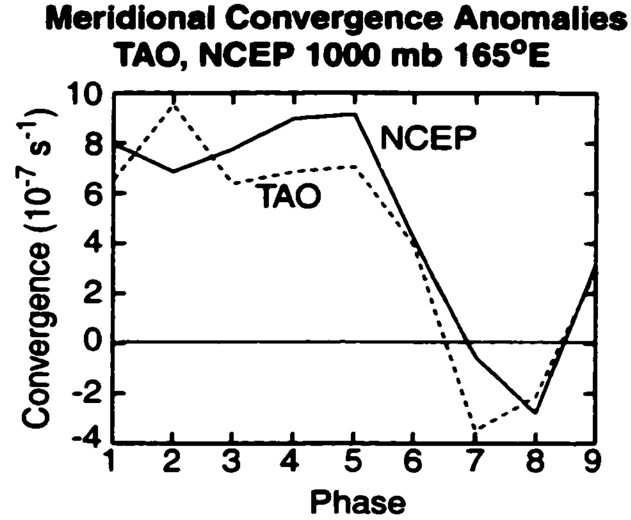

Figure A1.3. NCEP and TAO meridional convergence anomalies as a function of MJO phase. TAO averages are computed from the latitudes 2°N, Equator, and 2°S. NCEP averages are computed from the latitudes 2.5°N, Equator, and 2.5°S. Phases 3, 4, 7, and 8 are shown. The largest vector shown is 1.5 m s^{-1}.

Appendix B: The Cloud Work Function

The development here follows the work function derivation in Moorthi and Suarez (1992). Adjustment in McRAS occurs through an ensemble of entraining plumes. Each plume detrains at a different vertical level, and is specified by an entrainment parameter λ, where

$$\lambda(P_D) = \frac{(h_B - h^*(P_D))}{\left(\frac{c_p}{g}\right)\int_{P_D}^{P_B} \theta(P)[h^*(P_D) - h(P)]dP} \qquad (A2.1)$$

The subscript *B* denotes cloud base and the subscript *D* denotes the detrainment level for a given cloud type. Moist static energy is designated by $h(P)$, and $h^*(P)$ represents saturation moist static energy. $\theta(P)$ is the potential temperature, g specifies gravity, and c_p is the specific heat of dry air at constant pressure.

The normalized mass flux for an ensemble member increases linearly with height and is given by

$$\frac{\partial}{\partial z}\eta_\lambda(z) = \lambda \qquad (A2.2)$$

with the mass flux at cloud base taken as 1. Converting the mass flux relationship to pressure coordinates we find,

$$\frac{\partial}{\partial P}\eta_\lambda(P) = -\frac{c_p}{g}\theta\lambda \qquad (A2.3)$$

This equation can be integrated to give the normalized mass flux for a cloud type as a function of pressure,

$$\eta_\lambda(P) = 1 + \frac{c_p}{g}\lambda \int_{P}^{P_B} \theta dP \qquad (A2.4)$$

The cloud work function is then given by

$$A_\lambda = \int_{P_D}^{P_B} \frac{\eta_\lambda(P)}{1+\gamma(P)} \frac{[h^c_\lambda(P) - h^*(P)]}{P} dP \qquad (A2.5)$$

where

$$\gamma(P) = \frac{L}{c_p}\frac{d}{dT}q^*(P) \qquad (A2.6)$$

$h^c{}_\lambda$(P) is the cloud moist static energy for a cloud type λ, $q^*(P)$ is the saturation specific humidity of the environment, and L is the latent heat of condensation of water vapor. The moisture and temperature tendencies for a given cloud type are determined by the deviation of the cloud work function from the critical value of cloud work function (Lord et al. 1982).

Vita

Eric Daniel Maloney was born on November 3, 1972 in the great city of Chicago, where he developed a passion for the Earth's atmosphere (and pizza). He attended St. Laurence High School in the near-western suburb of Burbank, and then moved on to the University of Illinois at Urbana-Champaign in 1990, where he received his B. S. in Physics during May of 1994. That same summer he moved to Seattle to pursue graduate study in the atmospheric sciences at the University of Washington. After having an exciting graduate school career in Seattle, and receiving his Ph.D. in Atmospheric Sciences during August of 2000, Eric will move to Boulder, Colorado to work on a UCAR postdoc at NCAR. He will be accompanied by his beautiful wife, Heather.